Laser Spectroscopy of $^{208}Bi^{82+}$ and Commissioning of the HITRAP Cooling Trap

Laserspektroskopie an $^{208}Bi^{82+}$ und Inbetriebnahme der HITRAP Kühlfalle
Zur Erlangung des Grades eines Doktors der Naturwissenschaften (Dr. rer. nat.)
Genehmigte Dissertation von Max Henrik Horst aus Groß-Umstadt
Tag der Einreichung: 16.10.2023, Tag der Prüfung: 22.11.2023

1. Gutachten: Prof. Dr. Wilfried Nörtershäuser
2. Gutachten: Prof. Dr. Thomas Walther
Darmstadt, Technische Universität Darmstadt

TECHNISCHE UNIVERSITÄT DARMSTADT

Fachbereich Physik
Institut für Kernphysik
AG Nörtershäuser

LASER SpHERe

Laser Spectroscopy of $^{208}Bi^{82+}$ and Commissioning of the HITRAP Cooling Trap
Laserspektroskopie an $^{208}Bi^{82+}$ und Inbetriebnahme der HITRAP Kühlfalle

Accepted doctoral thesis by Max Henrik Horst

Date of submission: 16.10.2023
Date of thesis defense: 22.11.2023

Darmstadt, Technische Universität Darmstadt

Erklärungen laut Promotionsordnung

§ 8 Abs. 1 lit. c PromO

Ich versichere hiermit, dass die elektronische Version meiner Dissertation mit der schriftlichen Version übereinstimmt.

§ 8 Abs. 1 lit. d PromO

Ich versichere hiermit, dass zu einem vorherigen Zeitpunkt noch keine Promotion versucht wurde. In diesem Fall sind nähere Angaben über Zeitpunkt, Hochschule, Dissertationsthema und Ergebnis dieses Versuchs mitzuteilen.

§ 9 Abs. 1 PromO

Ich versichere hiermit, dass die vorliegende Dissertation selbstständig und nur unter Verwendung der angegebenen Quellen verfasst wurde.

§ 9 Abs. 2 PromO

Die Arbeit hat bisher noch nicht zu Prüfungszwecken gedient.

Darmstadt, 16.10.2023

M. Horst

Kurzfassung

Die Quantenelektrodynamik (QED) gilt heute als die am genauesten getestete Theorie der Physik. Die präzisesten Tests wurden dabei vor allem an vergleichsweise einfachen Systemen wie z.B. dem freien Elektron durchgeführt. Prüfungen in extrem starken elektrischen und magnetischen Feldern, in denen die QED nach heutigem Verständnis auch gültig sein sollte, haben noch nicht annähernd eine ähnliche Genauigkeit erreicht, was weitere Tests erforderlich macht.
Dafür eignen sich schwere und hochgeladene Ionen, weil die verbliebenen Elektronen in Kernnähe diesen extremen Feldern ausgesetzt sind. Da solche Ionen auf der Erde nicht natürlich vorkommen, ist es notwendig sie künstlich zu erzeugen. Dies erfordert hohe kinetische Energien und insbesondere für die schwersten Elemente große Beschleunigeranlagen, wie das GSI Helmholtzzentrum für Schwerionenforschung in Darmstadt.
Im Rahmen dieser Arbeit wurde die Laserspektroskopie an künstlich erzeugtem $^{208}Bi^{82+}$ bei relativistischen Energien am Speicherring ESR der GSI durchgeführt. Dies ist das erste Mal, dass auf diese Weise erzeugte Ionen in einem Speicherring erfolgreich laserspektroskopisch untersucht werden konnten. Die größte Herausforderung ist dabei die geringe Ionenanzahl, die zu niedrigen Signalzählraten in den Detektoren führt. Unter anderem durch die in dieser Arbeit durchgeführte Datenanalyse, konnte der gemessene Untergrund soweit reduziert werden, dass die Energiedifferenz der Hyperfeinaufspaltung extrahiert werden kann. Das erhaltene Ergebnis ist

$$^{208}\Delta E^{(1s)} = 5598.97(1)(8)\,\mathrm{meV}$$

und bildet einen wichtigen Meilenstein für den Test der QED in den stärksten im Labor zugänglichen Magnetfeldern.
Die Genauigkeit der Laserspektroskopie an Speicherringen wie dem ESR ist durch die Geschwindigkeitsverteilung der Ionen begrenzt. Mit Hilfe von Ionenfallen kann die Genauigkeit solcher Experimente um einige Größenordnungen verbessert werden. Allerdings ist es nicht möglich, die bei relativistischen Energien erzeugten Ionen direkt in einer Ionenfalle einzufangen.
Daher wurde im zweiten Teil dieser Arbeit zusätzlich die Kühlfalle der HITRAP-Anlage in Betrieb genommen. Die Aufgabe der HITRAP-Anlage ist es, die hochgeladenen Ionen abzubremsen, zu kühlen und zu den angeschlossenen Experimenten weiter zu transportieren. Die Kühlfalle bildet den letzten Teil der Abbremsung und ist für die sympathetische Kühlung der Ionen durch Elektronen zuständig. In dieser Arbeit konnte die Kühlfalle mit hochgeladenen Ionen und Elektronen aus lokalen Quellen in Betrieb genommen werden. Darüber hinaus konnten erstmals Ionen und Elektronen gleichzeitig in der Kühlfalle gespeichert werden. Dies führte schließlich zum ersten Nachweis von Kühleffekten von Elektronen auf hochgeladene Ionen in einer Penningfalle.

Abstract

Today, quantum electrodynamics (QED) is considered the most precisely tested theory in physics. The most precise tests have been performed mainly on comparatively simple systems such as the free electron. However, since QED should also be valid in the most extreme electric and magnetic fields, according to today's understanding, tests must be performed in this regime as well.
Heavy and highly charged ions are suitable for this purpose, because the remaining electrons near the nucleus are exposed to these extreme fields. Since such ions do not occur naturally on earth, they must be produced artificially. This requires high energies and, especially for the heaviest elements, large accelerator facilities, such as the GSI Helmholtzzentrum für Schwerionenforschung in Darmstadt, Germany.
In this work, laser spectroscopy of artificially produced $^{208}Bi^{82+}$ at relativistic energies was performed at the storage ring ESR of GSI. This is the first time that in-flight produced ions have been successfully studied by laser spectroscopy in a storage ring. The main challenge is the small amount of ions, which leads to low signal count rates in the detectors. In part due to the data analysis performed in this work, the measured background has been reduced to a point where the energy difference of the hyperfine splitting can be extracted. The obtained result is

$$^{208}\Delta E^{(1s)} = 5598.97(1)(8)\,\mathrm{meV}$$

and represents an important milestone for the test of QED in the strongest magnetic fields.
The accuracy of laser spectroscopy in storage rings like the ESR is limited by the velocity distribution of the ions. To improve the accuracy by several orders of magnitude, ion traps can be used. However, it is not possible to directly capture ions produced at relativistic energies in an ion trap.
Therefore, in the second part of this work, the Cooling Trap of the HITRAP facility was commissioned. The task of the HITRAP facility is to decelerate the highly charged ions, to cool them and to transport them further to the subsequent experiments. The Cooling Trap is the final step of the deceleration process and is responsible for the sympathetic cooling of the ions by electrons. In this work, the Cooling Trap was commissioned with highly charged ions and electrons from local sources. Moreover, for the first time, ions and electrons were simultaneously stored in the Cooling Trap. This finally led to the first demonstration of cooling effects of electrons on highly charged ions in a Penning trap.

Contents

List of Figures

1 Introduction

Quantum electrodynamics (QED) was the first relativistic quantum field theory that was developed and describes the interaction of electromagnetic fields with matter. This includes the interaction of charged particles through the exchange of photons and is the extension of classical electromagnetism. The QED is considered to be the most precisely tested theory in physics. For example, the measurement of the g-factor of the free electron reaches an extraordinary accuracy of less than one part per trillion [1] and is in agreement with theory at this level.
The theory should be valid not only for free particles or in light systems, but also for the heaviest elements. In such atoms or ions the electric and magnetic fields close to the nucleus reach extreme values. In the case of bismuth, the magnetic flux density at the nuclear surface is about 10^9 T [2]. This is of the order of the strongest magnetic fields in the universe expected at neutron stars, and close to the Schwinger limit of spontaneous pair production.
A test of QED in such extreme fields is important for the general understanding of field theory and may lead to physics beyond the Standard Model. High charge states and especially single-electron hydrogen-like (H-like) heavy systems are suitable for such tests, because electron-electron interactions are excluded, reducing the theoretical complexity and increasing the final precision. In this strong-field regime, the perturbative QED calculations in $Z\alpha$ are no longer valid, since $Z\alpha \approx 0.66$ in H-like U^{91+}, and non-perturbative approaches have to be used [3].
For H-like bismuth Bi^{82+}, the ground-state hyperfine splitting (HFS) can be measured by laser spectroscopy and used to test the theory. The HFS arises from the magnetic coupling of the nuclear and electronic spin, leading to a splitting in two energy levels for opposite relative orientation. For most elements, the transition energy is significantly lower than the energy of laser photons. In hydrogen, for example, the energy corresponds to a photon wavelength of 21 cm. In heavy Highly Charged Ions (HCI), however, the HFS is strongly enhanced since it scales roughly with $\approx Z^3$, making laser spectroscopic measurements feasible.
Since HCI do not occur naturally on earth, they have to be produced artificially to make them available for experiments. Especially for the heaviest elements, high relativistic energies are required, which are only available at a few large-scale accelerator facilities. One of them is the GSI Helmholtzzentrum für Schwerionenforschung in Darmstadt. In combination with the Experimental Storage Ring (ESR) [4], where the produced HCI can be stored over long periods of time and are accessible for experiments, GSI is currently the only facility where laser spectroscopy of HCI such as Bi^{82+} is possible.
Already in the 1990s, the HFS of the H-like ions $^{209}Bi^{82+}$ [5] and $^{207}Pb^{81+}$ [6] were measured at the ESR. However, these results could not be fully exploited as QED tests, since the experimental uncertainty cannot be matched by theory. This is caused by a large uncertainty in the calculation

of the magnetization distribution in the nucleus, also called the Bohr-Weisskopf effect. To circumvent this limitation, the specific difference

$$\Delta' E = \Delta E^{(2s)} - \xi \Delta E^{(1s)}$$

was introduced in [7]. By subtracting the ground-state hyperfine splitting of the H-like ($\Delta E^{(1s)}$) from the lithium-like (Li-like) charge state ($\Delta E^{(2s)}$) of the same isotope, the Bohr-Weisskopf effect can in theory be eliminated. Therefore, the factor ξ is introduced and determined theoretically to account for the different overlap of the $1s$ and $2s$ electron wave function with the nucleus.
The only measurement of the specific difference in a heavy HCI was performed with ^{209}Bi [8] and resulted in a 7σ-deviation from the theoretical value [9] at that time. This puzzle could be solved by correcting the wrongly tabulated literature value of the magnetic moment [10], which directly enters into the theoretical calculations. This correction brings theory and experiment back into agreement. However, as pointed out in [11], the current agreement is still based on complex calculations of the magnetic shielding constant. To confirm the cancellation of the Bohr-Weisskopf effect in the specific difference and to provide a rigorous QED test, a second system with a different magnetization distribution is needed.
Therefore, the radioactive isotope ^{208}Bi is selected. Besides the single proton in the $h_{9/2}$ shell like the stable isotope, ^{208}Bi has an additional hole in the $p_{1/2}$ neutron shell. This results in a different Bohr-Weißkopf effect and the coupling of the proton and neutron leads to a higher magnetic moment of the nucleus [11]. The isotope can be produced in flight at GSI by a nuclear reaction of ^{209}Bi with a stripper target. However, this results in a comparatively small number of ions.
The main part of this work is about the laser spectroscopy of relativistic ^{208}Bi^{82+} at the ESR. The beamtime took place in May 2022 and for the first time an artificially produced isotope is successfully targeted by laser spectroscopy in a storage ring. In addition to the optimized fluorescence detection, the detailed data analysis, which is the main contribution of this work, is key to this achievement. The extracted hyperfine splitting is the first part of the specific difference and reduces the search scan range in the upcoming beamtime at ESR with Li-like ^{208}Bi^{80+}.

The precision of laser spectroscopy in storage rings such as the ESR is limited by the uncertainty of the ion velocity. The high voltage (HV) of the electron cooler, which determines the absolute ion velocity, can only be measured to a level of a few ppm. In addition, the relative momentum distribution of the ions after electron cooling is limited by beam heating effects to about $\Delta p/p \approx 10\,\mathrm{ppm}$. This corresponds to a Doppler width in the GHz range, which is six orders of magnitude larger than the natural linewidth of the hyperfine transition.
To achieve ultimate precision for QED tests, the experiment has to be relocated to an ion trap. In ion traps, several cooling techniques can be employed to cool the ions to the ground state of motion. By using a narrow linewidth continuous wave laser, it is possible to resolve the natural linewidth of the transition in the trapped ions [12].
Capturing accelerator-produced ions such as Bi^{82+} in precision traps represents a huge challenge and has never been demonstrated. The ions have to be decelerated from a few hundred

$\mathrm{MeV/u}$ by at least five orders of magnitude. A worldwide unique project to achieve this is the Highly charged Ion Trap (HITRAP) facility [13, 14] at GSI. HITRAP is connected to the ESR and receives ions with an energy of $4\,\mathrm{MeV/u}$. After the first deceleration in the ESR, the linear decelerator system of HITRAP further reduces the ion energy to about $6\,\mathrm{keV/u}$. At this point, the ion beam has a large emittance and must be cooled for further transport to subsequent experiments. Therefore, the Cooling Trap, which facilitates the final deceleration step of HITRAP, is used to capture the ion bunch and cool it by electron cooling.
The commissioning of the HITRAP Cooling Trap is the second topic of this work. After several years without successful trap operation, it was decided to redesign the Penning trap in 2018. In this work, the new trap is commissioned with ions from a local source and electrons from a pulsed electron gun. After the successful storage of HCI and the optimization of electron production, both species are trapped simultaneously for the first time in the Cooling Trap. This results in the first observation of electron cooling effects on HCI in an ion trap, which is an important step towards precision experiments with heavy HCI at the HITRAP facility.

2 Theoretical Background

The experiments discussed in this work require ions at high energies as well as ions that are decelerated again. Therefore, concepts of ion acceleration and deceleration are introduced in Sec. 2.1. These concepts are also useful for understanding and evaluating systematic effects and uncertainties in storage ring experiments. After deceleration, ions can be confined in traps for beam preparation and precision experiments. The basic principles of ion trapping in a Penning trap are explained in Sec. 2.2.
An important technique in both, storage rings and ion traps, is electron cooling to enable precision experiments. The similarities and differences between the two setups are discussed in Sec. 2.3. A major part of this work is about the laser spectroscopy of the hyperfine structure of Bi^{82+} for a test of QED. Therefore, the atomic structure including the theoretical calculations of the energy levels is introduced in Sec. 2.4. In addition, the concepts of laser spectroscopy in a storage ring are covered in Sec. 2.5.

2.1 Accelerator Physics

Before discussing linear and circular accelerators, some general concepts are introduced, in particular the beam quality. The basis for the description of a particle with charge q under the influence of electric fields $\vec{E}$ and magnetic fields $\vec{B}$ is the Lorentz force

$$\vec{F}_{\mathrm{L}} = q(\vec{E} + \vec{v} \times \vec{B}) \tag{2.1}$$

[15]. Electric fields aligned in direction of ion motion are commonly used to change particle energy. In contrast, magnets are often used for beam deflection and focusing. This is particularly suitable for relativistic ion beams, which can be derived from Eq. 2.1. To obtain the same force $qE = qvB$ as a $1\,\mathrm{T}$ perpendicular magnetic field on a relativistic particle $v \approx c$, an electric field of $E \approx 300\,\mathrm{MV/m}$ is needed, which is technically not feasible. On the other hand, electrostatic components are well suited for the transport of low energy beams.
For the following considerations, a coordinate system is defined in the frame of the moving ion cloud (see Fig. 2.1). The origin is determined by the reference particle, which is located in the geometrical center of the ion ensemble and moves along the z-axis with the beam energy. The remaining ions are distributed in the transverse xy-plane and have a longitudinal spread corresponding to different energies. Since ions in accelerators are often moving close to the speed of light c, a relativistic description is necessary. Therefore, the velocity β in terms of the

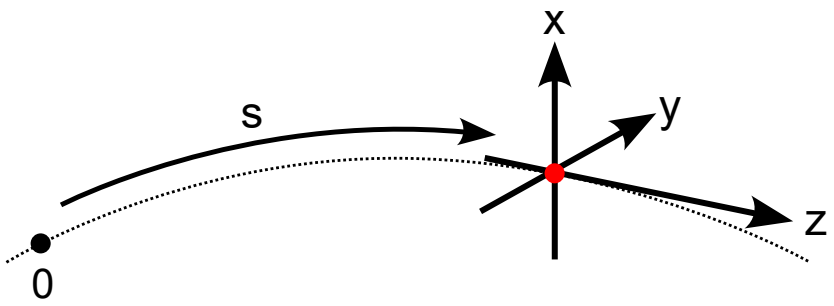

Figure 2.1: Coordinate system of a moving ion cloud. The ions move in z-direction from the starting point 0 along an arbitrary trajectory. The reference ion (red) is at the origin of the coordinate system. In ring accelerators, the distance covered on the central path is usually referred as s.

speed of light and the Lorentz factor γ are introduced

$$\begin{aligned} \beta &= \frac{v}{c}, \\ \gamma &= \frac{1}{\sqrt{1-\beta^2}}. \end{aligned} \tag{2.2}$$

The beam energy or kinetic energy E_{kin} can be derived from the total relativistic energy E_{tot} and the rest mass energy mc^2 [16]

$$E_{\text{kin}} = E_{\text{tot}} - mc^2 = (\gamma - 1)mc^2. \tag{2.3}$$

The description of the beam energy in terms of energy per nucleon is common in accelerator physics. This is obtained by inserting the atomic mass unit u for the mass m which yields

$$E_{\text{kin}} = (\gamma - 1) \cdot 931.5\,\text{MeV/u}^{1}. \tag{2.4}$$

In addition to energy, beam quality is crucial for accelerator operations and for experiments, since it allows for better control of the ions. Starting from the coordinate system introduced in Fig. 2.1, an ion propagating along a trajectory can be described as a point in the six-dimensional phase space

$$\vec{a} = (x, x', y, y', z, \Delta p/p). \tag{2.5}$$

Here x is the position and x' is the slope in x-direction with respect to the reference ion. The same is true for the second transverse direction y. In longitudinal direction, z describes the position and $\Delta p/p$ the relative momentum [15]. The particle momentum $p = \gamma m v$ is connected by

$$E_{\text{tot}} = \sqrt{(pc)^2 + m^2c^4} \tag{2.6}$$

to the total energy. Since $\Delta p = p - p_0$ is the momentum difference to the reference particle with momentum p_0, the collection of relative momentum of each individual ion describes the

[1] In the literature, the unit is sometimes represented as MeV/nucleon.

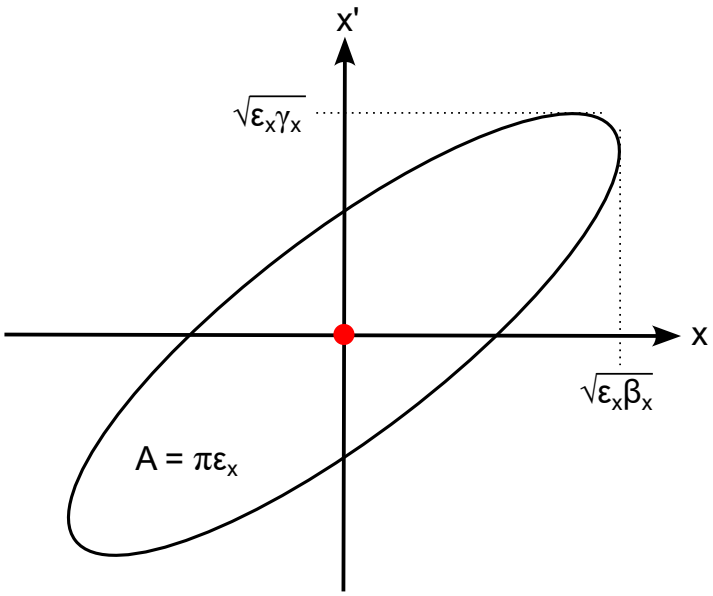

Figure 2.2: Phase ellipse of the (x, x')-phase space. Each ion of an ensemble can be represented by a particular point within the ellipse with respect to the reference particle (red). The area of the ellipse is called emittance and is a measure of the beam quality. The maximum position and slope are given by the ellipse parameters.

energy distribution of the ion beam.
In transverse direction, the coordinates (x, x') and (y, y') describe the displacement and divergence in the respective direction. In linear beam dynamics, both directions are not coupled and can be treated independently. It should be noted, that the description based on the slope $\sin x' \approx x'$ (for y-direction respectively) is only valid if the beam energy remains constant. To study the dynamics in an accelerating field, the full transverse momentum $p_\mathrm{x} = p_0 \sin x'$ of the particle has to be taken into account.
A convenient way to represent an ion beam in transverse direction, such as x, is to map each individual ion into the (x, x')-phase space. All particles can be enclosed by the so-called phase ellipse (see Fig. 2.2)

$$\epsilon_\mathrm{x} = \gamma_\mathrm{x} x^2 + 2\alpha_\mathrm{x} x x' + \beta_\mathrm{x} x'^2 \tag{2.7}$$

with ellipse parameters $\alpha_\mathrm{x}, \beta_\mathrm{x}, \gamma_\mathrm{x}$ and ϵ_x [15]. The area occupied by the phase ellipse $A = \pi\epsilon_\mathrm{x}$ is the (geometrical) emittance. The emittance is a measure of the beam quality. The smaller the maximum deviations from the reference particle in terms of angle and position, the smaller the emittance and the better the beam quality. Using the momentum instead of the slope gives the normalized emittance

$$\epsilon_\mathrm{n,x} = \beta\gamma\epsilon_\mathrm{x}, \tag{2.8}$$

which also takes into account the change in momentum during acceleration or deceleration. In some cases, emittance is also referred to as beam temperature. A "hot" beam has a large emittance, which can be reduced by applying a beam cooling technique to obtain a "cooled"

beam with smaller emittance.
An advantage of introducing a phase ellipse, is the simplified description of ion beam dynamics. By selecting particles on the envelope of the ellipse and calculating their evolution in time, it is possible to describe the dynamics of the entire ion ensemble, since by definition every single particle is enclosed by the ellipse. The evolution of the ellipse can be calculated in terms of a matrix formalism, which is derived in detail in [15]. This description is similar to the ABCD matrix analysis used for light propagation in optics.
An important statement regarding the evolution of the phase ellipse is given by Liouville's theorem. The area of the ellipse - or the normalized emittance - cannot be changed by conservative forces [16]. Such forces are, for example, exerted by magnetic fields for beam deflection and focusing. If a beam is focused in a transverse direction, the phase ellipse can be rotated so that the position distribution in a focal point becomes small. However, since the area of the ellipse is not changed by the magnetic field, the ion beam will have a large angular distribution at the focal point and will expand thereafter. Therefore, ion beams have to be refocused in both transverse directions after a certain distance to prevent losses.
Without active countermeasures, the beam emittance of a particle beam will increase over time. This is caused by dissipating and non-conservative forces, as mainly induced by scattering processes. These can be divided into two groups. The first one is scattering with residual gas ions. To reduce this effect, accelerator components are operated at low pressures. This is especially important for storage rings, where ions propagate easily over $10^9\,\mathrm{m}$. Therefore, the residual gas pressure in storage rings is on the order of $10^{-11}\,\mathrm{mbar}$. The second scattering effect is intrabeam scattering, where Coulomb scattering occurs between beam particles [17]. This is particularly relevant for large particle densities in high intensity beams.
These effects are also called heating effects. One way to counteract them is to cool the beam, which reduces the beam emittance. The technique of electron cooling is introduced in Sec. 2.3.

2.1.1 Linear Accelerator

One option to achieve high ion energies in a straight line is to use radio frequency (RF) cavity accelerators. The basic principle is the generation of an accelerating field by high-power RF fields [15]. The cavity structure is designed in a way, that a standing wave can build up between the conducting walls. The ions have to be synchronized with the oscillation period of the field in order to interact only with the accelerating part of the longitudinal electric field. The resulting ion beam is divided into small packets called bunches. Most designs have cylindrical conducting drift tubes, which are used like Faraday cages to shield the ions in regions, where the RF field has a decelerating effect. To compensate for the increase in energy and the faster propagation of the ions, the drift tubes become longer towards the end of the accelerating structure.
A specific realization of such a LINear ACcelerator (LINAC) structure is the Alvarez LINAC [16] as illustrated in Fig. 2.3a. The cavity consists of several drift tubes fixed in the center by metal rods. Between the tubes, a standing RF field creates an accelerating electric field for the ions. During acceleration, the gaps act as lenses that defocus in the radial direction [16]. Therefore, it is necessary to use focusing elements like quadrupole magnets inside of the structure to keep the ion beam within the apertures of the drift tubes. An Alvarez structure typically accepts

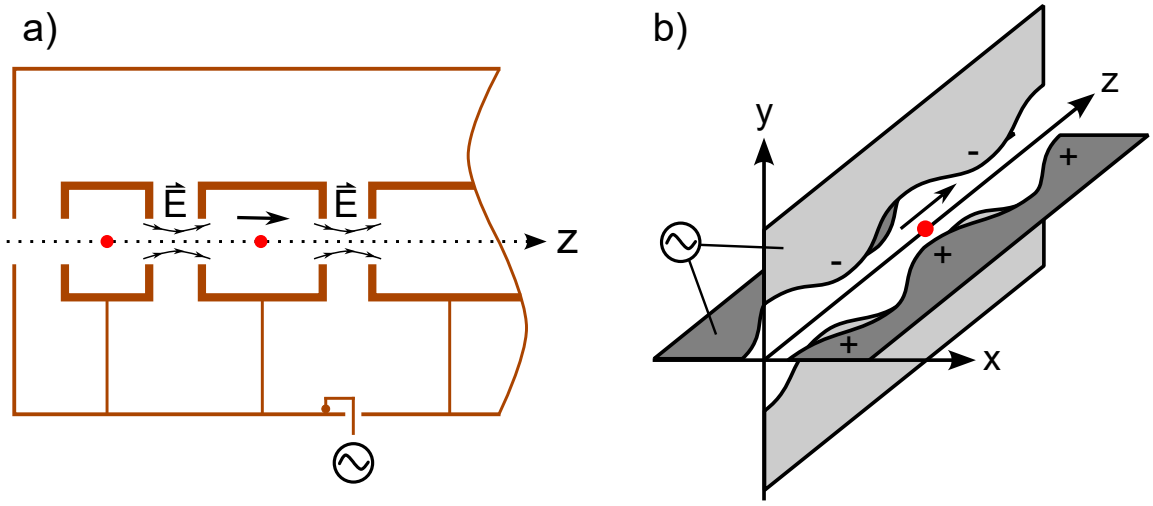

Figure 2.3: a) Schematic illustration of an Alvarez LINear ACcelerator (LINAC) structure for ion acceleration. The ions are accelerated by a standing RF field in the gaps between the shielding drift tubes. b) Schematic of an Radio Frequency Quadrupole (RFQ) accelerating structure. The RF field is generated by sinusoidal electrodes. An RFQ accelerates and focuses the ion beam at the same time.

beam energies around $1\,\mathrm{MeV/u}$ and accelerates the beam up to several tens or even hundreds of $\mathrm{MeV/u}$.
Another accelerating structure based on RF fields is the Radio Frequency Quadrupole (RFQ) [18]. Instead of drift tubes with accelerating gaps, two horizontal and two vertical electrode rods generate a radio-frequency-quadrupole field. The rods have a sinusoidal structure with the wavelength increasing towards the end. The horizontal and vertical maxima are shifted by π, resulting in a variation of the transverse field gradient. As a result, ions with a suitable phase dependence are not only accelerated, but also focused in both transverse directions. An RFQ can ideally be used to accelerate ions from the low $\mathrm{keV/u}$ to the low $\mathrm{MeV/u}$ range [19]. The accessible energy range, compact design and focusing characteristics make the RFQ a preferred primary accelerator stage.

An important principle for stable accelerator operation is phase focusing. It prevents an uncontrollable divergence of the ion bunch in longitudinal direction caused by different energy classes. Ions with charge q undergo an energy change ΔE_{RF} (see Fig. 2.4a) in the accelerating gap depending on the phase difference ϕ to the RF field [16]

$$\Delta E_{\mathrm{RF}} = qU_0 \sin\phi. \tag{2.9}$$

The RF field has a maximum potential U_0. If the reference ion has a phase difference of $\phi_r = 0$ (see Fig. 2.4b), there is no net energy transfer from the RF field. Ions with the same momentum as the reference particle, but arriving later ($\phi > 0$), are accelerated and will arrive earlier, i.e. with a reduced phase shift, but with increased energy ΔE in the next gap. After some time, the

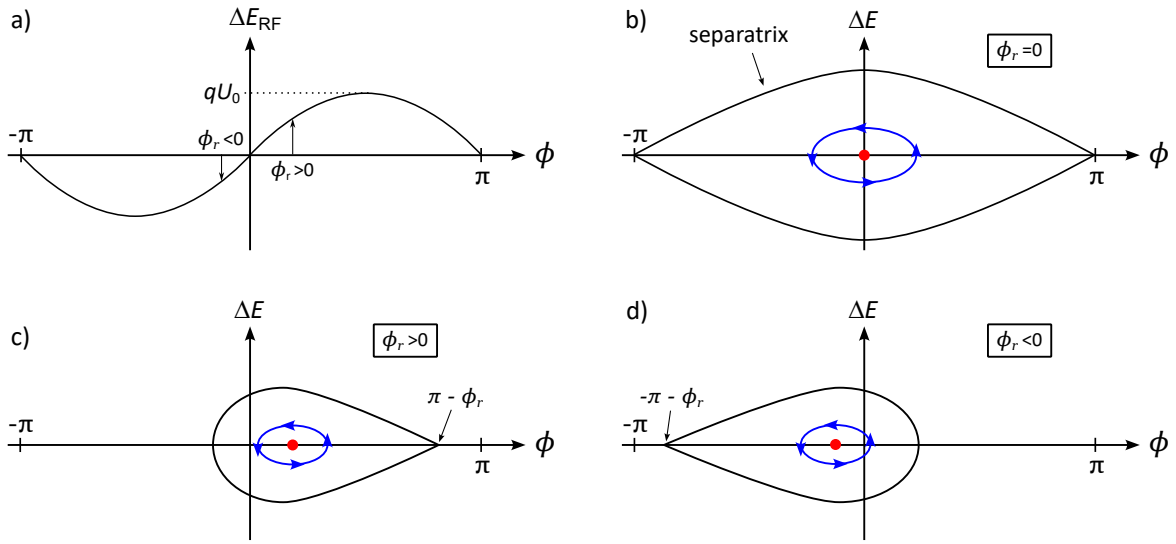

Figure 2.4: In a) the energy gain ΔE_{RF} with respect to the phase relative to the RF field is shown. Depending on the phase ϕ_r of the reference particle (red), the ion ensemble is stationary with no energy change (b), accelerated with a net energy gain (c), or decelerated with a net energy loss (d) [16]. The y-axis is the energy difference to the reference particle, while the x-axis represents the phase relative to the RF field. As long as the particles remain in the region enclosed by the separatrix, stable oscillations around the reference particle occur as indicated by the blue ellipses.

phase difference has disappeared ($\phi = \phi_r$), but now the ions have a higher momentum and will therefore arrive earlier, leading to a negative phase ($\phi < 0$) next. In the $\Delta E - \phi$ diagram, representing the longitudinal phase space, the ions move counterclockwise[2] on an elliptically shaped curve as shown in blue in Fig. 2.4b. The same principle applies to any ion with an arbitrary displacement in phase-momentum space relative to the reference ion. The result is an oscillation around the reference ion and the ion bunch will not diverge longitudinally.
The phase-stable region of this oscillation is enclosed by the so-called separatrix. Particles outside of the separatrix follow unstable trajectories and will get lost [15]. In a synchrotron or storage ring, the stable region is commonly called bucket and the oscillation is called synchrotron oscillation.
To accelerate an ion bunch, the reference particle has to have a positive phase difference $\phi_r > 0$ (see Fig. 2.4c) to the RF field. This shifts the ion ensemble into a region where each interaction with the RF field yields a net energy gain. Again, ions with a phase or momentum difference to the reference particle perform elliptically shaped oscillations. The separatrix in this case has a fish-like shape and depends on the phase of the reference ion [16].
The same principle applies to the deceleration of an ion beam. Therefore, the reference particle

[2]Depending on the machine-specific transition energy γ_{tr} and the momentum of the particles, the oscillation direction can also be inverted. In this case, the falling edge of the RF field is used.

has to have a negative phase $\phi_r < 0$ (see Fig. 2.4d) with respect to the RF field. The deceleration is in principle a time reversed acceleration. This means that the particles are only exposed to a decelerating RF field and the drift-tube length or the sinusoidal electrode structures of an RFQ must evolve from long to short.
An important consideration is the evolution of the transverse emittance. Since Liouville's theorem applies only to the normalized emittance, the geometric emittance changes during the momentum change. Using Eq. 2.8 with subscript $+$ for higher energy and $-$ for lower energy, it follows

$$\epsilon_{\text{n,-}} \stackrel{!}{=} \epsilon_{\text{n,+}} \Rightarrow \epsilon_+ = \epsilon_- \frac{\beta_- \gamma_-}{\beta_+ \gamma_+}. \tag{2.10}$$

Acceleration from low to high energies results in a decrease in the measured geometric emittance. This is useful for further ion manipulation. In the case of deceleration, the emittance grows, resulting in a transverse "blow-up" of the ion beam. The strongly divergent beam is a major challenge for deceleration facilities.

2.1.2 Synchrotron and Storage Ring

Synchrotrons and storage rings are accelerators in which ions are captured and stored in a closed orbit. The ions are revolving with high frequencies and implemented accelerating structures can be used many times to reach higher energies than in single-pass linear machines. A special type of ring accelerator is the synchrotron. It consists of several dipole magnets that bend the ion beam on its circular path. In addition, quadrupole and higher order magnets are used to focus the beam in transverse direction. A characteristic parameter of a circular machine is the magnetic rigidity $B\rho$. This parameter results from the fact, that the relativistic centripetal force required to keep the ion on its circular orbit is provided by the Lorentz force (see Eq. 2.1) exerted inside a transverse magnetic dipole field

$$\gamma m \frac{v^2}{\rho} \stackrel{!}{=} qvB \Rightarrow B\rho = \frac{\gamma m v}{q} = \frac{p}{q}. \tag{2.11}$$

The magnetic rigidity of a ring accelerator is given in Tm and specifies the maximum possible energy of a stored particle with respect to the radius and the available magnetic field strength of the machine [16]. This is determined by the maximum magnetic field B of the dipoles and the curvature radius ρ of the trajectory in the dipole.
Particles injected into a synchrotron are usually pre-accelerated, but have a low momentum compared to the maximum magnetic rigidity of the synchrotron. To increase their energy, RF cavities analogous to those in linear accelerators are used. The challenge is the synchronized adjustment of the resonance frequency and the ramping of the magnetic field with the increasing velocity and revolution frequency of the ion beam. The required synchronous ramping process with the particle energy is responsible for the name of the synchrotron.
During acceleration, the so called synchronicity condition [15]

$$f_{\text{RF}} = h f_{\text{rev}} \tag{2.12}$$

with RF frequency f_{RF} and ion revolution frequency f_{rev} has to be fulfilled. The parameter h is called harmonic number and determines the possible number of bunches revolving in the ring. As explained before, phase focusing is an important mechanism to keep the bunches in the stable phase space called *bucket*.

A storage ring can be thought of as a stationary synchrotron. This means that high-energy ions are injected and revolve in the ring at a constant energy. The main purpose of storage rings is to perform experiments with the stored relativistic particles. The ion-optical lattice is thus designed to allow for the implementation of experimental sections. Furthermore, windows for laser experiments or ports for detectors are foreseen. A big advantage of experiments with stored ions is the increased beam current due to the periodic circulation of the ions.
Storage rings can be operated in bunched mode like a synchrotron or in coasting-beam mode. In coasting mode, the RF cavity is switched off and the ions can distribute across the entire storage ring. This happens on a short time scale due to the momentum distribution of the ions and due to the Coulomb interactions with each other (intra-beam scattering). A coasting beam exhibits lower space charge and heating effects, which may be advantageous for some applications.
The betatron oscillation is a characteristic transverse motion of ions in a synchrotron or storage ring and is defined by the ion-optical elements of the ring. It arises from the analytical solution of the particle dynamics based on Newton's principles and the Lorentz force (Eq. 2.1), which leads to Hill's differential equation

$$y'' + K(s)y = 0 \tag{2.13}$$

with periodic coefficient $K(s + C) = K(s)$ [16]. It has the form of a harmonic oscillator but with a position-dependent restoring force. A general solution of this equation is given by

$$y(s) = a\sqrt{\beta(s)}\cos[\phi(s) + \phi_0]. \tag{2.14}$$

This is a periodic oscillation with variable amplitude $a\sqrt{\beta(s)}$. The parameter a and ϕ_0 define the amplitude and the initial phase of the single particle at longitudinal position s in the ring. The function $\beta(s)$ is the *betatron function*, which characterizes the transverse motion. For a matched ion beam with emittance $\epsilon_{x,y}$ in x or y direction, the position-dependent beam size can be easily calculated by

$$d_{x,y}(s) = \sqrt{\epsilon_{x,y}\beta_{x,y}(s)} \tag{2.15}$$

[16] (see also Fig. 2.2). The betatron oscillation is not synchronous with the revolution frequency of the ions, but has a lower repetition rate called *betatron tune*. Since there is an increasing phase offset after each revolution of the betatron oscillation, the maximum displacement of $d_{x,y}(s)$ drifts along the orbit and smaller apertures than this will inevitably lead to beam loss.
A further horizontal deviation from the central orbit occurs, if the stored particles have an energy difference to the reference particle. This is described by the dispersion function [16], which depends on the properties of the dipole magnets. A higher ion momentum means, that

the distance traveled in the deflecting dipole magnets becomes longer, for lower momentum it becomes shorter. This effectively shifts the beam trajectory outward or inward. Dispersion occurs naturally in an ion bunch, because of the influence of the synchrotron oscillations on the ion energy.

2.2 Penning Traps

Ion traps are devices that confine charged particles in a limited volume of space for an extended period of time. A special type of ion trap is the Penning trap, in which ions are confined axially by an electrostatic potential and radially by a magnetic field. The Penning trap is named after Frans Penning, who in 1936 studied the behavior of electrons in magnetic fields at low pressures [20] and thus inspired further progress. In 1989, Hans Georg Dehmelt was awarded with the Nobel Prize in Physics for his contributions to the development and use of the Penning trap [21].
Penning traps are nowadays employed in many different areas of research. They are used to store and cool particles, to select ions of specific masses and charges for experiments and non-destructive detection methods allow the analysis during storage. Typical applications are in high-precision experiments such as mass measurements [22], laser spectroscopy of matter [23] and antimatter [24] or g-factor measurements [1, 25]. On the other hand, Penning traps can be used to accumulate and cool ions to prepare them for subsequent experiments. This is done, for example, at ISOLTRAP [26] at the CERN-ISOLDE facility or at the HITRAP facility [13] at GSI, which is part of this work.
A brief theoretical description of particle motion in an ideal Penning trap is presented in Sec. 2.2.1. The discussion is extended in Sec. 2.2.2 in terms of elongated cylindrical Penning trap designs with open endcaps to establish a connection with the HITRAP Cooling Trap.

2.2.1 Trapped Particle Motion

A charged particle in a Penning trap is confined by an electric and a magnetic field. In its hyperbolic form, the Penning trap consists in total of three curved electrodes, two endcaps and a ring between which an electrostatic field $\vec{E}$ is applied (see Fig. 2.5a). The field is given by an electrostatic potential Φ, which in this case has a quadrupolar shape, so that the trapped particles perform harmonic oscillations

$$\vec{E} = -\vec{\nabla}\Phi \quad ; \quad \Phi = \frac{U_0}{4d^2}(Ax^2 + By^2 + Cz^2) \tag{2.16}$$

[27]. Parameters A, B and C are arbitrary factors, $d = \sqrt{\frac{1}{2}\left(z_0^2 + \frac{1}{2}r_0^2\right)}$ is a normalization factor called *trap parameter*[3] and U_0 is the applied voltage between endcap and ring. To satisfy the Laplace equation $\triangle\Phi = 0$, the coefficients must fulfill $A + B + C = 0$. Choosing $A = B = -1$

[3] for a trap with an axial length of z_0 and a radius of r_0

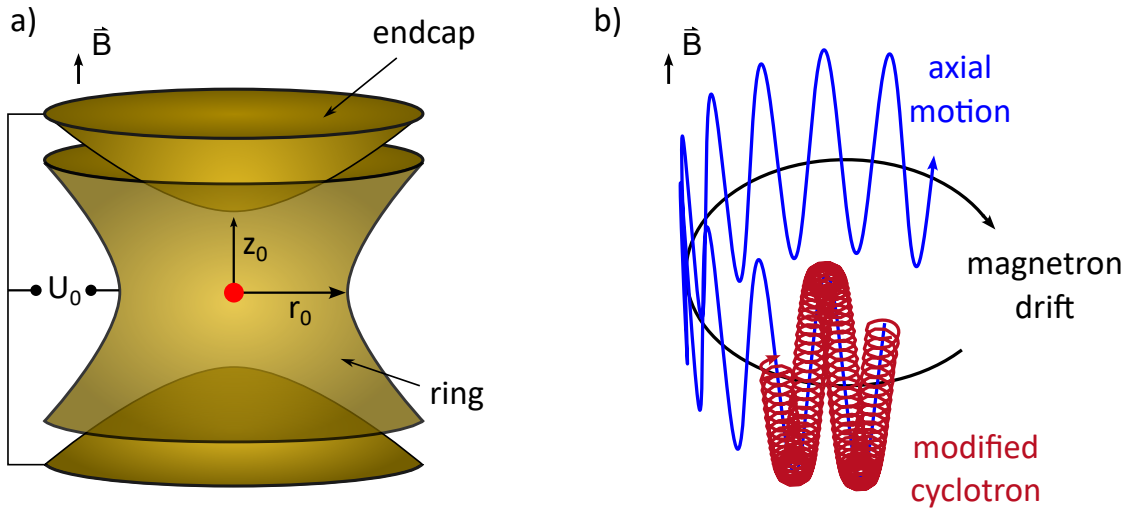

Figure 2.5: a) Hyperbolic Penning trap design, which creates a quadrupolar electrostatic potential. The magnetic field is aligned with the z-axis of the trap. b) Schematic of the particle movement in the trap, which is a superposition of three independent motions.

and $C = 2$ leads to the cylindrically symmetric form

$$\Phi = \frac{U_0}{4d^2}(-x^2 - y^2 + 2z^2) = \frac{U_0}{4d^2}(2z^2 - r^2) \tag{2.17}$$

with radial component r. The different signs of r and z in Eq. 2.17 indicate that the potential has a saddle point at the origin, which is confining along the z-axis but repulsive in radial direction r. In general, it is not possible to generate an electrostatic potential minimum in free space, as stated by Earnshaw's theorem [27]. Therefore, in a Penning trap, a magnetic field $\vec{B} = (0, 0, B_0)$ is superimposed with the electric field to also achieve radial particle confinement. Analogous to Eq. 2.1, stored particles with charge q, mass m and velocity $\vec{v}$ are suspect to the Lorentz force

$$\vec{F}_\mathrm{L} = q(-\vec{\nabla}\Phi + \vec{v} \times \vec{B}). \tag{2.18}$$

With Newton's second law of motion $\vec{F} = m\vec{a}$ and the electric potential defined in Eq. 2.17, a set of differential equations follows

$$\begin{aligned} \frac{d^2x}{dt^2} - \omega_\mathrm{c}\frac{dy}{dt} - \frac{1}{2}\omega_\mathrm{z}^2 x = 0\ , \\ \frac{d^2y}{dt^2} + \omega_\mathrm{c}\frac{dx}{dt} - \frac{1}{2}\omega_\mathrm{z}^2 y = 0\ , \\ \frac{d^2z}{dt^2} + \frac{1}{2}\omega_\mathrm{z}^2 z = 0. \end{aligned} \tag{2.19}$$

The different constants are combined to the cyclotron frequency ω_c and the axial frequency ω_z

$$\omega_c = \frac{qB_0}{m} \quad \text{and} \quad \omega_z = \sqrt{\frac{qU_0}{md^2}}. \tag{2.20}$$

Since the magnetic field exerts no force in z-direction, the motion along the z-coordinate is a simple harmonic oscillation with frequency ω_z and decoupled from the radial motion. For the motion in the x, y-plane the solution is found to be a superimposed oscillation with two frequencies

$$\begin{aligned} \omega_+ &= \frac{\omega_c}{2} + \sqrt{\left(\frac{\omega_c}{2}\right)^2 - \frac{\omega_z^2}{2}} \\ \omega_- &= \frac{\omega_c}{2} - \sqrt{\left(\frac{\omega_c}{2}\right)^2 - \frac{\omega_z^2}{2}} \end{aligned} \tag{2.21}$$

[27]. The oscillation with frequency ω_+ is called modified cyclotron motion and the oscillation with frequency ω_- is called magnetron drift. A stored particle performs in combination a superposition of all three motions, which is illustrated in Fig. 2.5b. In order to have stable trajectories, the expression under the root in Eq. 2.21 must be positive. This leads to the stability criterion

$$\frac{m}{q} < \frac{d^2 B_0^2}{2U_0}, \tag{2.22}$$

which relates the maximum storable mass-to-charge ratio to the trap parameter and the applied electric and magnetic fields.
For He-like argon in a Penning trap such as the HITRAP Cooling Trap with $B_0 = 4\,\mathrm{T}$, $d = 5\,\mathrm{mm}$ and $U_0 = 1\,\mathrm{kV}$ the frequencies are calculated to be

$$\omega_- \approx 2\pi \cdot 8\,\mathrm{kHz} \ , \ \omega_z \approx 2\pi \cdot 625\,\mathrm{kHz} \ , \ \omega_+ \approx 2\pi \cdot 25\,\mathrm{MHz}. \tag{2.23}$$

Usually, the sorting order of the frequencies is, as in this case, $\omega_- \ll \omega_z \ll \omega_+ < \omega_c$.

2.2.2 Cylindrical Open-Endcap Design

The ideal hyperbolically shaped Penning trap introduced in the last part is advantageous to obtain a perfect harmonic potential for precision experiments. However, the design has some drawbacks for real experiments. Both endcaps are closed and the trap center is not accessible along the z-axis, which makes ion injection difficult. Therefore, it is not suitable for capturing an elongated ion bunch due to the compact design. Furthermore, the curved electrodes are challenging to manufacture and irregularities can disturb the harmonic potential.
A frequently used design to solve these problems is the cylindrical open-endcap design, as depicted in Fig. 2.6. In its minimal form it consists of three cylindrically shaped electrodes, the inner ring and two outer endcaps. The addition of two compensation electrodes, makes it possible to correct for the anharmonicity introduced by the electrode shapes within a small spatial region in the trap center. The electrodes are placed on top of each other and are

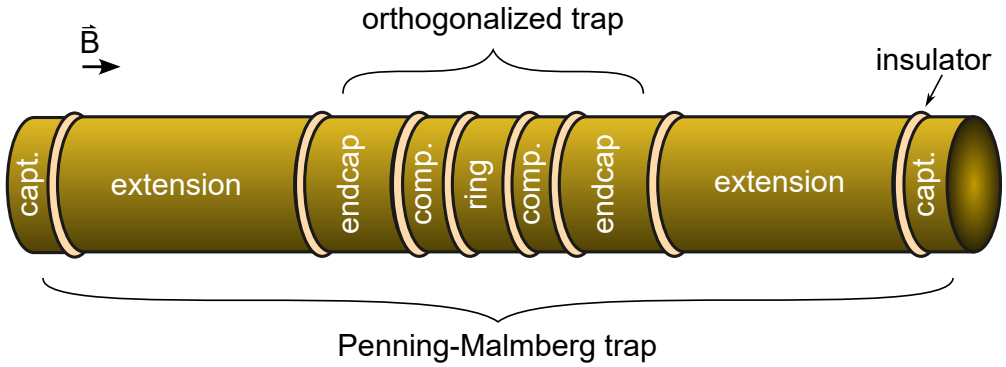

Figure 2.6: Illustration of an open-endcap Penning trap with axial access. The minimal design consists of a ring and two endcap electrodes. With the addition of compensation electrodes and proper electrode dimensioning, the potential in the ring can be corrected to be harmonic, which is called an orthogonalized trap. A Penning-Malmberg style trap has two capture electrodes and a long central section. This part may consist of one electrode or may be divided into several electrodes.

separated by insulators, resulting in a trap stack.
The electric potential in the trap center can be expanded in Legendre polynomials $P_k(\cos\theta)$, in order to describe it and compare it with the hyperbolic form

$$\Phi = \frac{1}{2}U_0 \sum_{k=0}^{\infty} C_k \left(\frac{r}{d}\right)^k P_k(\cos\theta) \quad , k \in 2\mathbb{Z} \tag{2.24}$$

[28]. Only expansion coefficients C_k with even k are non-zero, due to the cylindrical symmetry. For a perfect hyperbolic Penning trap, the coefficient $C_2 = 1$ and all higher order terms are vanishing. For the cylindrical form, the higher-order expansion coefficients are in general not vanishing, resulting in anharmonic oscillations.
However, since the coefficients C_k depend on the trap geometry, the trap radius r_0 and the trap length z_0 can be chosen such that C_4 vanishes, which is referred to as *orthogonalized* Penning trap [28]. Additionally, the length of the compensation electrode z_c can be selected, such that C_6 also vanishes. Since higher order anharmonicities decrease in magnitude by a factor of at least $(r/d)^8$, the result is in good approximation harmonic.
In practice, the theoretical values that result in a harmonic trapping potential are not obtained in the laboratory. As in the case of the hyperbolic trap, the machining has tolerances and also the alignment of the electrodes is not perfect. However, the resulting deviations are usually not large and can be compensated by fine-tuning the correction electrode voltage. Therefore, the cylindrical design is also suitable for precision experiments [28].
Moving away from precision experiments with single ions to experiments with ion clouds, the trap must be able to store a large number of ions. If many charged particles are stored in a Penning trap, collective phenomena become important, which can be treated in the context of non-neutral plasmas. A cloud of charges changes the trapping potential and the oscillation

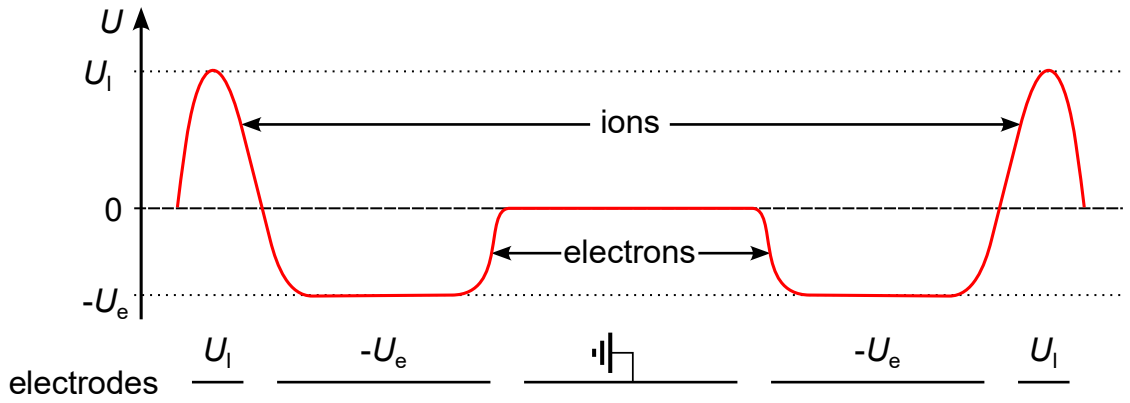

Figure 2.7: Illustration of a nested trap potential. The length of the electrodes and the applied voltages are indicated on the bottom of the figure. Ions and electrons are stored simultaneously and overlap spatially in the trap center. The repulsive potential $-U_e$ for electrons is attractive for the ions.

frequencies [29]. For the axial frequency ω_z a downward shift occurs, depending on the plasma frequency ω_p

$$\omega_z' = \omega_z \sqrt{1 - \frac{\omega_p^2}{3\omega_z^2}} \ , \ \omega_p^2 = \frac{q^2 n}{\epsilon_0 m} \tag{2.25}$$

with particle density n and permittivity in free space ϵ_0. Additionally, the total amount of charges that can be stored is limited by repulsive space-charge effects. The condition that ω_z' remains a real number, leads to a theoretical axial space-charge limit of

$$n \leq \frac{3\epsilon_0 U_0}{q d^2}. \tag{2.26}$$

At higher densities, a given particle will experience a space-charge potential that is higher than the endcap potential and axial confinement is lost. This can be counteracted with higher endcap potentials or by increasing the confinement volume.
In a Penning-Malmberg trap design, the trap volume is increased by extending the space between the endcap electrodes, which are in this case also called capture electrodes. This can be done with an elongated ring electrode or with multiple electrodes as shown in Fig. 2.6. The geometrical-extended trap design allows a higher capture efficiency for spatially elongated particle ensembles. The trade-off for the length is the loss of the well-defined harmonic electric potential. This results in energy transfer between the motional degrees of freedom and energy-dependent oscillation frequencies, leading to a broadening of the frequency distribution [30]. In an extreme case, the endcaps are so far apart that the particles are no longer in a harmonic potential. Instead, they are in a "bathtub"-like potential, in which they are reflected at the endpoints and are not affected by an electrical trap potential in between. The frequencies of the motions can be calculated as a rough estimation with Eq. 2.20 and Eq. 2.21, but the real frequencies depend strongly on the individual setup.

Multiple-electrode Penning traps can be used to create several electrostatic minima. The length of the electrodes and the applied voltage determine the shape of the potential wells. The potential can be formed to store particles of opposite charge at the same time [31]. In Fig. 2.7 a nested potential is illustrated for the simultaneous storage of ions and electrons, which can be utilized for electron cooling (see Sec. 2.3.2). The ions are stored between the outer capture electrodes, which are at a positive potential U_{I}, while the electrons are stored in the center of the trap, with a negative potential $-U_{\mathrm{e}}$ applied to the endcap electrodes. In this configuration, ions and electrons can be simultaneously confined and spatially overlapped in the center of the trap.

2.3 Electron Cooling

When preparing ions for high precision experiments, cooling techniques are important. Cooling reduces the momentum spread of an ion ensemble. Therefore, the number of ions in certain velocity classes is increased by depleting others. This benefits energy-dependent experiments, such as laser spectroscopy, since the signal-to-noise ratio can be significantly increased, while reducing the width of resonance-like structures.
In a storage ring, cooling means reducing the longitudinal and/or transversal emittance of the ion beam. This dampens the internal motions (e.g. synchrotron oscillations) of the ions while leaving the center-of-mass energy largely unaffected. The main techniques of beam cooling in a storage ring are stochastic cooling [32] and electron cooling [33]. In some special cases, laser cooling is also feasible [34, 35].
These methods are analogously applicable in ion traps. In this case, the center-of-mass motion is often also addressed in order to obtain a cold and compact particle ensemble at rest in the laboratory frame. Depending on the setup, the ions reach cryogenic temperatures or can even be cooled down to the quantum mechanical ground state of motion [36]. Therefore, different cooling methods are combined in order to achieve the desired result.
With respect to this work, electron cooling is of particular importance since it is applied for cooling of highly charged ions in storage rings as well as in Penning traps [37] and provides ion cooling on short time scales. Electron cooling is a sympathetic cooling process in which ions and electrons are spatially combined. They can be idealized as two gases with a specific temperature. These gases are brought into contact so that they can interact via Coulomb collisions. In the rest frame of the cold electrons, the hot ions move with high relative velocities compared to the stationary electrons. The energy transfer slows down the fast ions and accelerates the slow ions as they pass through the electron cloud. If the energy transferred to the electrons is either dissipated or the electrons are continuously replaced by cold electrons, the ion cloud will eventually reach the electron temperature.
In the following, the properties and characteristics of electron cooling in storage rings and Penning traps are described in more detail.

2.3.1 Electron Cooling at Storage Rings

Electron cooling in storage rings was originally proposed in 1966 by G. Budker [33] for the accumulation of antiproton beams. To bring electrons in contact with the revolving ion beam, a well directed electron beam is introduced in a straight section of the storage ring. The electrons are typically emitted by a thermal gun and electrostatically accelerated by an electron gun potential U_{EG}. Thereby, the longitudinal momentum spread is compressed and a nearly monoenergetic beam is obtained. To increase the cooling efficiency, the potential is chosen such that the electron velocity corresponds to the mean velocity of the ions. The electrons are guided and superimposed with the ions by magnetic fields until they are deflected towards the collector. Since the electron beam is continuously refreshed, the temperature of the reservoir stays constant.
A detailed introduction into electron cooling can be found in [38]. For a qualitative understanding, the dependence of the cooling time for a thermalized and moderately pre-cooled beam

$$\tau_{\mathrm{ec}} \propto \frac{A}{q^2} \cdot \frac{1}{n_{\mathrm{e}}} \frac{l_{\mathrm{ring}}}{l_{\mathrm{cool}}} \cdot (\delta v)^3 \tag{2.27}$$

as provided in [39] is discussed. The cooling time is proportional to the ion mass, here represented by the mass number A, and proportional to $1/q^2$, which is favorable for HCI with high charge states. A high electron density n_{e} and a long interaction region l_{cool} compared to the ring circumference l_{ring} reduces the cooling time. An important factor is the cubic dependence on the ion velocity deviation $\delta v = v_{\mathrm{ion}} - \bar{v}_{\mathrm{e}}$ with respect to the mean electron velocity. For a hot ion ensemble the cooling power is small since δv is large for a considerable fraction of the ions, whereas cooling is strongest, if the ion temperature is close to the electron temperature. Therefore, the use of stochastic cooling as a pre-cooling method can be beneficial to reduce the cooling time. Typical electron cooling times are on the order of seconds.
So far, the electron and ion beam are considered to be perfectly overlapping. The non-centered position of the ion beam within the electron beam is a possible imperfection. The electron velocity is not homogeneous across the electron beam diameter due to the beam's space-charge potential $U_{\mathrm{SC}}(r)$. Thus, the ions experience a position-dependent electron velocity. The effective acceleration potential U_{eff} of the electrons depending on the radial position r is

$$U_{\mathrm{eff}}(r) = U_{\mathrm{EG}} - U_{\mathrm{SC}}(r). \tag{2.28}$$

To estimate this effect, the electron beam can be considered in good approximation as a homogeneously charged cylinder. For the arising space-charge potential within the electron beam ($r < R_{\mathrm{e}}$) one obtains

$$U_{\mathrm{SC}}(r) = \frac{1}{4\pi\epsilon_0} \left[\frac{r^2}{R_{\mathrm{e}}^2} - 1 - 2 \ln \frac{R_{\mathrm{D}}}{R_{\mathrm{e}}} \right] \frac{I_{\mathrm{e}}}{\beta_{\mathrm{e}} c} \tag{2.29}$$

[40]. R_{D} is the drift-tube radius, I_{e} the electron current and β_{e} the electron velocity in units of the speed of light. The space-charge can result in potential differences on the order of $100\,\mathrm{V}$ between the edge and the center of the electron beam. Such systematic effects must be taken into account in precision experiments.

2.3.2 Electron Cooling in Penning Traps

Ions, which shall be captured in a Penning trap, are usually produced in a hot environment and transported with energies varying from eV to a few keV. After capture, the energy is split between the axial and the two radial oscillations (see Sec. 2.2.1). To prepare the ions for precision experiments, the energy in all degrees of freedom has to be reduced. A fast method to achieve this is sympathetic cooling with a buffer gas such as helium [36]. Therefore, helium gas at room temperature or lower temperatures can be introduced into the trap and the stored ions collide with the gas atoms and transfer their energy. The thermalization time can be adjusted by the pressure in the trap. This works well for singly charged ions, but not for HCI or antiprotons, because the high pressure environment leads to rapid charge exchange or annihilation.
To overcome this limitation, the buffer gas can be replaced by an electron cloud. This has been demonstrated with antiprotons in [41]. An advantage of electron cooling is the fast energy reduction over several orders of magnitude, making it a perfect initial cooling step for high-energy particles.
In contrast to an electron cooler in a storage ring, the electrons are trapped at rest and are not constantly refreshed. This is not necessary, because they dissipate energy by emission of synchrotron radiation in the strong magnetic field of the Penning trap.
In general, synchrotron radiation occurs if a charged particle is accelerated. In a Penning trap, the highest frequency oscillation is the cyclotron motion. This oscillation exerts a continuous acceleration on the particles around the magnetic field lines. The radiation causes an exponential decay of the initial electron energy E_0

$$E(t) = E_0 e^{-t/\tau_\mathrm{e}}. \tag{2.30}$$

The magnitude of the effect is determined by the cooling constant

$$\tau_\mathrm{e} = 3\pi\epsilon_0 \frac{mc^3}{q^2\omega_c^2} = 3\pi\epsilon_0 \frac{m^3c^3}{q^4B^2} \tag{2.31}$$

and depends on mass m, charge q, dielectric constant ϵ_0 and magnetic field B [42]. In a typical magnetic field of $6\,\mathrm{T}$ this leads to a cooling constant of $\tau_\mathrm{e} = 0.07\,\mathrm{s}$ for electrons and they dissipate $99\,\%$ of their initial energy in $0.3\,\mathrm{s}$. This effect is also present for other oscillations or particles, but the slower frequency or the strong mass dependence makes it negligible. For example, for a proton under the same conditions it would take over 50 days to lose $1\,\%$ of its energy.
If electrons are captured in a Penning trap, they lose their initial energy at a high rate and quickly reach cryogenic temperatures. A hot cloud of ions with temperature T_ion introduced into the trap will be cooled as soon as they start to interact with the electrons. The thermalization time τ_th to reach the temperature equilibrium of both species can be derived from plasma studies and is proportional to

$$\tau_\mathrm{th} \propto \frac{m_\mathrm{ion}}{q^2} \cdot \frac{1}{n_\mathrm{e}} \cdot \left(\frac{k_\mathrm{b}T_\mathrm{ion}}{m_\mathrm{ion}} + \frac{k_\mathrm{b}T_\mathrm{e}}{m_\mathrm{e}} \right)^{3/2} \tag{2.32}$$

with ion mass m_{ion} and Boltzmann constant k_{b} [37]. This relation is only valid for a thermal distribution of the involved particle ensembles. While this is true for the cold electrons, injected ions can have arbitrary velocity distributions depending on their production process. However, after some collisions with the thermal electron cloud, the distribution should evolve towards a Maxwell-Boltzmann distribution and the condition is satisfied.
The thermalization time has a strong similarity to Eq. 2.27 with respect to the dependence on the mass-to-charge ratio and the electron density. The last term can be interpreted as a cubed velocity dependence. Assuming the electrons have a constant temperature, the ion cooling time decreases as the ion temperature decreases. This leads to a faster than exponential reduction of the ion energy.
In reality, the electrons will not keep their low temperature, but will be heated by the interaction with the ions, because they are not constantly refreshed and can only dissipate energy with cooling time τ_{e}. This leads to the following pair of rate equations

$$\begin{aligned} \frac{d}{dt}T_{\text{ion}} &= -\frac{1}{\tau_{\text{th}}}(T_{\text{ion}} - T_{\text{e}}) \\ \frac{d}{dt}T_{\text{e}} &= \frac{N_{\text{ion}}}{N_{\text{e}}}\frac{1}{\tau_{\text{th}}}(T_{\text{ion}} - T_{\text{e}}) - \frac{1}{\tau_{\text{e}}}(T_{\text{e}} - T_{\text{trap}}) \end{aligned} \tag{2.33}$$

with the total number of ions N_{ion} and electrons N_{e}. These rate equations are solved numerically in [37] for antiprotons. Depending on the number and density of electrons, cooling times of a few seconds from $1\,\text{keV}$ to the sub-eV level are achievable. Due to the self-cooling mechanism of the electrons, they have the same longitudinal and transverse energy and are able to cool all ion motions.

When moving away from negatively charged antiprotons to ions with high positive charge, the question is whether the electrons are captured by the HCI. The dominant process here is radiative recombination (RR)

$$X^{q+} + e^- \rightarrow X^{(q-1)+} + \gamma \tag{2.34}$$

where the binding energy is released in form of a photon. Systematic simulations for electron cooling of a cloud of bare uranium ions in a Penning trap are performed in [43]. The survival probability of the bare charge state shows, that recombination effects appear already at the beginning of the cooling process. However, the cross section at the start is small and the majority of ions do not change their charge state. If the ion energy starts to decrease and the relative velocity becomes smaller, a sudden increase of ion-electron recombination is predicted and the initial charge state is lost within a short period of time.
The simulations show, that electron cooling is an efficient way to cool a hot cloud of HCI in a few seconds, but that ions and electrons must be separated at some point to avoid the loss of the high charge state.

2.4 Atomic Structure

Starting with Rutherford's scattering experiment [44], the theoretical description of the structure of atoms developed continuously and became more accurate in the early twentieth century. Rutherford discovered, that the atom consisted of a positively charged centre surrounded by a number of electrons equal to the atomic number. Until then, there was no suitable method to describe the electron distribution. This changed with the atomic model introduced by Niels Bohr [45], who sought to explain experimental observations of the hydrogen atom. The Bohr model postulates, that electrons can only exist on discrete orbits. By equating the Coulomb force with the centripetal force, the binding energy E_n of an electron on the n-th orbit in the Bohr model is thus obtained to be

$$E_n = -\frac{m_\mathrm{e} e^4 Z^2}{8\epsilon_0^2 h^2 n^2} = -\frac{1}{2} m_\mathrm{e} c^2 (\alpha Z)^2 \cdot \frac{1}{n^2} = -E_\mathrm{Ryd} \cdot \frac{Z^2}{n^2} \tag{2.35}$$

with electron mass m_e, elementary charge e, nuclear charge number Z, Planck constant h and vacuum permittivity ϵ_0. The parameter $\alpha = e^2/(4\pi\epsilon_0\hbar c) \approx \frac{1}{137}$ is the fine-structure constant and $E_\mathrm{Ryd} = m_\mathrm{e} e^4/(8\epsilon_0^2 h^2)$ is the Rydberg constant.
For the first time electrons were assigned with a quantum number n and a specific binding energy. Thus, discrete energies for transitions between different bound states of the electron could be understood, which explained the line pattern of atomic spectra.
Further insights into the structure of the hydrogen atom came with the advent of quantum mechanics. Heisenberg and Schrödinger developed the matrix and the wave equation formalism of quantum mechanics, respectively, which were shown to be equivalent [46]. The Schrödinger equation for a non-relativistic electron in a spherically symmetric Coulomb potential $V_\mathrm{C}(r)$ is

$$\left(\frac{-\hbar^2}{2m_\mathrm{e}}\nabla^2 + V_\mathrm{C}(r)\right)\psi = E\psi. \tag{2.36}$$

The solution of the Schrödinger equation (derived e.g. in [47]) by a separation into radial and angular parts reveals the same energy levels as Eq. 2.35. The fact that there must be discrete energy states follows naturally from the required boundary conditions. In the case of hydrogen, the wave function ψ must vanish for large r ($\psi(r \to \infty) \to 0$). Furthermore, the additional quantum numbers l and m result from solving the angular part for respective boundary conditions [48]. The quantum number l indicates the size of the angular momentum and m_l its orientation with respect to the quantization axis. For the integer numbers l and m the following conditions apply:

$$l < n \quad \text{and} \quad -l \leq m_l \leq +l\ . \tag{2.37}$$

The set of quantum numbers (n, l, m) fully characterizes the atomic state as long as the electron spin (see below) is not considered. According to Eq. 2.35, the binding energy depends only on n and different combinations of l and m are indistinguishable, they are degenerate. The lowest possible energy level is the so-called $1s$ state with $n = 1$ and $l = m = 0$. Calculating the radial

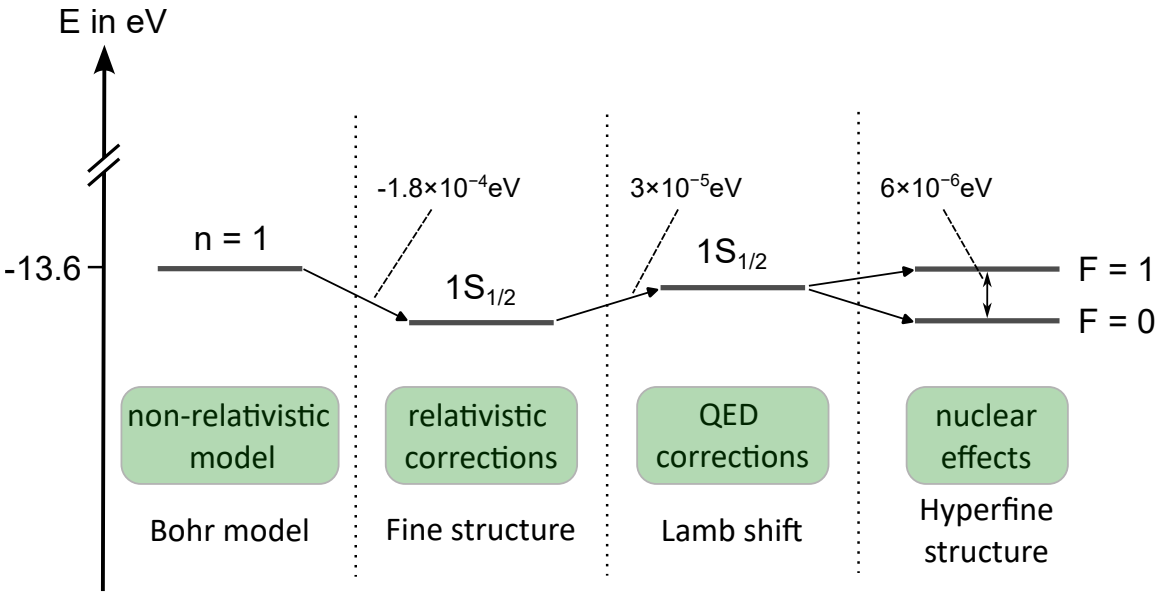

Figure 2.8: Influence of different corrections to the electron ground state energy in hydrogen. The illustration is only schematic and not to scale. The effective corrections are getting smaller from left to right.

probability distribution ($4\pi r^2|\psi(r)|^2$) of the $1s$ electron from the wave function [48], yields a maximum likelihood at

$$r_\mathrm{m} = \frac{\epsilon_0 h^2}{\pi m_e e^2} = a_0 \approx 50\,\mathrm{pm}. \tag{2.38}$$

a_0 is the Bohr radius and is already derived from the Bohr model. However, an important difference to that model is the probabilistic nature of the wave function. The electron is not localized on a fixed orbit, but has a non-zero probability density of being closer or further away from the nucleus than a_0, including being inside the nucleus.
So far, relativistic effects are missing in the description of the hydrogen system. To describe them, perturbations of the non-relativistic Schrödinger equation (2.36) can be implemented. In total, three different relativistic effects can be distinguished, which are later summarized as *fine structure* effects (see Fig. 2.8). The first is due to the relativistic kinetic energy of the electron, which leads to an increase in its mass. This effect is largest for $n = 1$, since the electron velocity is highest near the nucleus [48]. The next effect is called *Darwin term* and involves a correction of the potential energy term. Since the electron position is not perfectly localized, but smeared out according to the uncertainty principle, the Coulomb potential has to be calculated for a small volume and not only for a point in space.
For the last effect the concept of electron spin must be introduced. This intrinsic property of the electron was observed experimentally in the famous Stern-Gerlach experiment [49]. In addition to the orbital angular momentum, the electron must have another angular momentum

called spin. The spin $\vec{s}$ of an electron is associated with a magnetic moment of

$$\vec{\mu}_s = -g_\mathrm{s}\frac{e}{2m_\mathrm{e}}\vec{s} = -g_s\frac{\mu_B}{\hbar}\vec{s}, \tag{2.39}$$

with the *Landé-factor* $g_s \approx 2$ and the Bohr magneton μ_B [48]. This looks similar to the magnetic moment of the electron orbital angular momentum

$$\vec{\mu}_l = -\frac{e}{2m_\mathrm{e}}\vec{l}, \tag{2.40}$$

resulting from the movement of the electron around the nucleus. This motion of charges generates a magnetic field $\vec{B}_l$ at the site of the electron. The electron spin can be oriented either up ($s_z = +\frac{1}{2}$) or down ($s_z = -\frac{1}{2}$) with respect to the magnetic field resulting in a potential energy of

$$\Delta E_{l,s} = -\vec{\mu}_s \cdot \vec{B}_l. \tag{2.41}$$

This spin-orbit interaction leads to a coupling of the spin and orbital angular momentum to a total angular momentum $\vec{j} = \vec{l} + \vec{s}$. Using the total angular momentum quantum number $j = |l \pm s|$, the formula for the relativistic corrected hydrogen levels takes the compact form

$$E_{n,j} = E_n\left[1 + \frac{Z^2\alpha^2}{n}\left(\frac{1}{j+1/2} - \frac{3}{4n}\right)\right] \tag{2.42}$$

[48] with the non-relativistic energy E_n from Eq. 2.35. The spin-orbit coupling can only occur for $l > 0$ and is not present for s-electrons ($l = 0$). A typical notation for the atomic level is nl_j, where $l = 0, 1, 2$ is represented by *S, P, D* respectively. The lowest hydrogen level is $1S_{1/2}$.
The fine structure effects lead to a decrease of the binding energy and have in case of the ground state of hydrogen ($E_1 \approx -13.6\,\mathrm{eV}$) a magnitude of $\Delta E_\mathrm{fs} \approx 1.8 \times 10^{-4}\,\mathrm{eV}$ (see Fig. 2.8). The factor $Z^2\alpha^2$ is small for hydrogen and can easily be treated perturbatively, which is not applicable anymore for H-like HCI with $Z \approx 82$. At this point it should also be mentioned that Eq. 2.42 is only valid for one-electron systems, for which an analytical solution exists. For all other non-hydrogen-like systems, numerical methods or approximations must be used.
Another way to derive the relativistic energy levels of atoms and ions is based on the Dirac equation

$$(\vec{\alpha}\cdot\vec{p} + V_\mathrm{nuc}(x) + \beta m_\mathrm{e})\Phi_n(x) = E_n\Phi_n(x) \tag{2.43}$$

with Dirac matrix $\vec{\alpha}$ and the nuclear binding potential $V_\mathrm{nuc}(x)$ [2]. The Dirac equation is used to describe spin-$1/2$ particles and inherently takes into account both quantum mechanical and relativistic effects. The solution of Eq. 2.43 for the energy levels in compact form is

$$E_{n,j} = m_\mathrm{e}c^2\left[\left(1 + \frac{(Z\alpha)^2}{[n-(j+1/2)+\zeta]^2}\right)^{-1/2} - 1\right] \tag{2.44}$$

with $\zeta = \sqrt{(j+1/2)^2 - (Z\alpha)^2}$ [2]. The first two terms of a Taylor expansion in powers of $(Z\alpha)^2$ of these energy levels yields as result Eq. 2.42. Terms of order $\mathcal{O}(Z\alpha)^6$ and higher

provide additional small corrections. Thus, fine structure effects are directly incorporated into the Dirac theory and do not need to be treated perturbatively.
According to Eq. 2.42, states with different j and identical quantum number n are not degenerate, but states with the same j but different l are. However, the experiment of Lamb and Retherford [50] has observed a difference between the $2S_{1/2}$ and the $2P_{1/2}$ state, which is now called *Lamb-shift*. This difference cannot be explained by the Schrödinger or Dirac equation and led to the development of quantum electrodynamics (QED).
QED is a quantum field theory that describes the electromagnetic interactions. In this framework, electrons interact with their environment by exchanging photons. An electron can also emit and reabsorb the same photon, which leads to the effect of *self energy*. To account for this process, it is included by the renormalization of the electron mass. Furthermore, the electron can interact with virtual electron-positron pairs that appear and disappear within the limits of the uncertainty principle. For the short time of their existence they can affect propagating photons. This *vacuum polarization* effect can be included by the renormalization of the electron charge [2].
Both effects must be taken into account as QED corrections for the exact description of the electron binding energy. The correction depends on the spatial distribution of the electron and is strongest near the nucleus. Furthermore, it leads to the experimentally observed shift of the electron binding energy for different quantum numbers l. The $2S_{1/2}$ - $2P_{1/2}$ *Lamb-shift* is with $\Delta E_L \approx 3 \times 10^{-5}\,\mathrm{eV}$ smaller then the fine structure effects for the $1S_{1/2}$-electron [48]. QED effects are treated in some more detail in Sec. 2.4.2.

2.4.1 Hyperfine Structure

The atomic nucleus can carry an angular momentum additional to its charge Ze. It is an analog to the spin of the electron, originates from the coupling of orbital and spin angular momentum of all protons and neutrons and is called nuclear spin $\vec{I}$. Nuclei in their ground state have a spin, if the number of protons or neutrons is odd, resulting in unpaired nucleons. In analogy to the electron spin, the nuclear spin is related to the nuclear magnetic moment

$$\vec{\mu}_I = g_I \frac{e}{2m_\mathrm{p}} \vec{I}. \tag{2.45}$$

Compared to Eq. 2.39, the nuclear moment of a proton is smaller by the ratio of electron and proton mass $\frac{m_\mathrm{e}}{m_\mathrm{p}} \approx \frac{1}{1836}$. The parameter g_I is the dimensionless nuclear *g-factor*, which correlates the spin to the magnetic moment of the specific particle and is $g_{I,\mathrm{p}} = 5.59$ for the proton and $g_{I,\mathrm{n}} = -3.83$ for the neutron [51]. The nuclear magnetic moment and the electronic magnetic moment lead to a coupling of the nuclear and the total angular momentum of the electron shell to the total angular momentum $\vec{F} = \vec{j} + \vec{I}$ of the atom. For $j = 1/2$ or $I = 1/2$, there are two possible orientations leading to a hyperfine splitting as shown in Fig. 2.8. For a H-like ion this splitting can be calculated as

$$\Delta E_\mathrm{HFS} = \alpha g_I \frac{m_\mathrm{e}}{m_\mathrm{p}} \frac{F(F+1) - I(I+1) - j(j+1)}{2j(j+1)(2l+1)} m_\mathrm{e}c^2 \frac{(Z\alpha)^3}{n^3} A(Z\alpha) \tag{2.46}$$

[2]. $A(Z\alpha)$ accounts for relativistic corrections and is

$$A(Z\alpha) = n^3(2l+1)\frac{\kappa[2\kappa(\lambda+n_r)-N]}{N^4\lambda[4\lambda^2-1]} \tag{2.47}$$

with $\kappa = (-1)^{j+l+1/2}\cdot(j+1/2)$, $\lambda = \sqrt{\kappa^2-(\alpha Z)^2}$, $n_r = n-|\kappa|$ and $N = \sqrt{n_r^2+2n_r\lambda+\kappa^2}$ [2]. In Eq. 2.46 the proportionality to $(Z\alpha)^3 n^{-3}$ is important. The splitting is largest for K-shell ($n=1$) electrons and scales strongly with the nuclear charge Z.
For the ground state in hydrogen with $j=1/2$ and $I=1/2$, the hyperfine levels are $F=0$ and $F=1$. The energy splitting between these levels is $\Delta E_{\text{HFS,H}} \approx 6\times10^{-6}\,\text{eV}$, which corresponds to the famous $21\,\text{cm}$-line of the M1 transition between the two hyperfine levels. In contrast, the single-electron system $^{209}\text{Bi}^{82+}$ the energy splitting between $F=4$ and $F=5$ is $\Delta E_{\text{HFS,Bi}} \approx 5.1\,\text{eV}$ [5]. This splitting is six orders of magnitude larger and corresponds to a photon wavelength of $243\,\text{nm}$.
Besides the energy splitting, the lifetime τ of the upper hyperfine level of the ground-state can be calculated as

$$\tau^{-1}_{\text{HFS,H}} = \frac{\alpha}{3\hbar}\frac{\Delta E^3_{\text{HFS}}}{(m_\text{e}c^2)^2}\frac{I}{2I+1}\left[g_e - g_I\frac{m_\text{e}}{m_\text{p}}\right]^2 \tag{2.48}$$

[2]. The lifetime is proportional to the bound-electron g-factor g_e, which can be used for an experimental test of theoretical calculations [52]. Furthermore, the lifetime scales strongly with the nuclear charge

$$\tau_{\text{HFS,H}} \propto \Delta E^{-3}_{\text{HFS}} \propto Z^{-9}. \tag{2.49}$$

This results in a huge increase of the corresponding transition strengths for HCI. For the example above, the lifetime of the $F=1$ level in hydrogen is $\tau_{\text{HFS,H}} > 10^7\,\text{a}$, while that for the $F=5$ level in H-like $^{209}\text{Bi}^{82+}$ is $\tau_{\text{HFS,Bi}} \approx 400\,\mu\text{s}$. The combination of the increasing energy splitting and the decreasing lifetime in heavy HCI, enables a measurement of the hyperfine splitting in $^{209}\text{Bi}^{82+}$ by laser spectroscopy.

2.4.2 Corrections to the Hyperfine Splitting

In Eq. 2.46 the nucleus is treated point-like with respect to the magnetic moment as well as the charge distribution. In addition, QED effects have not yet been included. These three effects can be taken into account as follows

$$\Delta E_{\text{HFS,c}} = \Delta E_{\text{HFS}}\left((1-\delta)(1-\epsilon)+\frac{\chi_\text{rad}}{A(Z\alpha)}\right). \tag{2.50}$$

Parameter δ is the nuclear charge-distribution correction (Breit-Schwolow), ϵ is the nuclear magnetization-distribution correction (Bohr-Weißkopf) and χ_rad represents the QED correction [53]. The finite-size corrections are significant for heavy H-like ions already at a relative precision of about 10^{-4}, since the remaining electron has a considerable overlap with the nucleus. The individual corrections are explained below.

Table 2.1: Different model calculations of the Bohr-Weisskopf correction ϵ for $^{209}Bi^{82+}$. Most values are not assigned with uncertainties.

Reference	ϵ for $^{209}Bi^{82+}$
Boucard and Indelicato [55]	0.0215
Shabaev et. al [54]	0.0118
Gustavsson et al. [56]	0.0131
Labzowsky et al. [57]	0.0131
Tomaselli et al. [58]	$0.0210(16)$
Sen'kov and Dmitriev [59]	$0.0095(+7, -38)$

Nuclear Charge Distribution

The spatial distribution of the electric charge in the nucleus influences the electron wave function and thus the hyperfine splitting. To account for the difference from a point-like nucleus, a specific nuclear model for the charge distribution must be used. For example, the charge distribution for $^{209}Bi^{82+}$ is evaluated for a homogeneously charged sphere ($\delta = 0.110$ [53]) or a two-parameter Fermi model ($\delta = 0.1111$ [54]). It turns out that the resulting corrections are very similar for different approaches (compare Fig. 26 in [2]). The theoretical uncertainty of this contribution is therefore small compared to the uncertainty of the nuclear magnetization distribution and is not yet a limiting factor.

Nuclear Magnetization Distribution

Analogous to the extended charge distribution, the magnetic moment of the nucleus is distributed across some volume and the arising magnetic potential is not a perfect point-dipole field. The effect was first studied by Bohr and Weisskopf [60] and is therefore often called *Bohr-Weisskopf* effect. For the description they used the picture of a smeared-out dipole distribution and considered the spin and angular components of the magnetic moment separately. Within their calculations, they introduced a density function of the magnetization distribution and integrated its effect over the volume of the nucleus to derive the interaction energy between the extended nucleus and the electron. Since the distribution was not known, the result has to be considered as a model-dependent estimation.
Currently, it is still not possible to derive the magnetization distribution from first principles. Therefore, various models are used to describe it. The simplest models treat the magnetization distribution spread over the Fermi distribution of the nucleus like the charge distribution [55]. The majority of models are based on the single-particle approach, where the extended magnetization originates only from the additional odd nucleon. This nucleon can be described, for example, with the Schrödinger equation by employing a Woods-Saxon potential [54, 56]. This approach is especially justified for ^{209}Bi or ^{208}Bi, since these nuclei are close to the stable

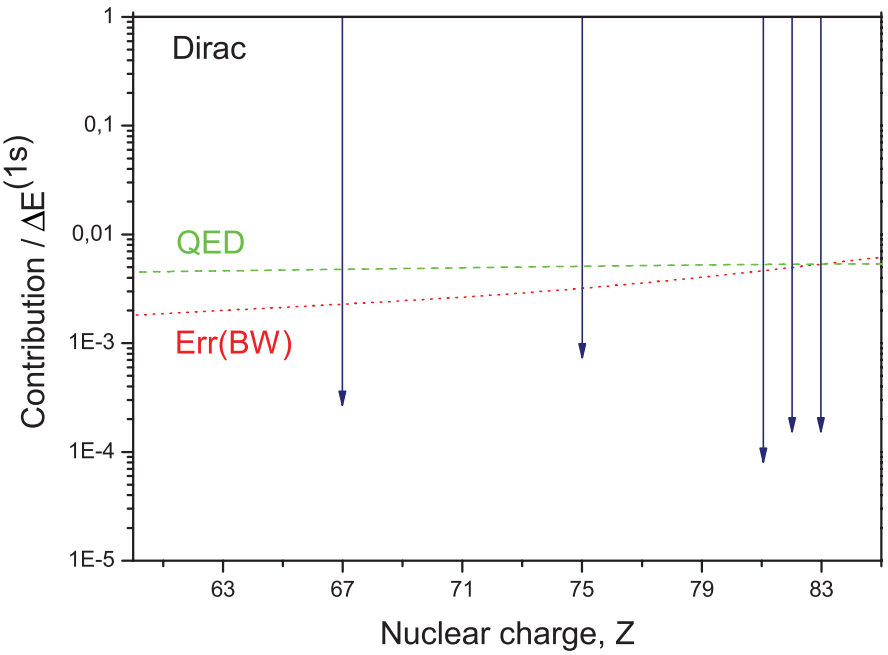

Figure 2.9: Relative contribution to the ground-state hyperfine splitting in H-like ions of the quantum-electrodynamics (QED) correction and the uncertainty of the Bohr-Weisskopf (BW) effect with respect to the Dirac value. The arrows represent the experimental results of Ho^{66+} [61], Re^{74+} [62], Tl^{80+} [63], Pb^{81+} [6] and Bi^{82+} [5] from left to right. The uncertainty of the BW effect is significantly higher than the experimental results and QED tests are only possible to a limited extent. (From Volotka et al. [64]. Reproduced with permission of Wiley.)

doubly magic lead nucleus ^{208}Pb, which is a simpler system. For ^{209}Bi, a valence proton has to be considered and for ^{208}Bi an additional unpaired neutron can be treated as a hole in the magic ^{208}Pb core.
Another single-particle approach treats the proton as a Dirac particle moving in the field of the nucleus given by the strong interaction, which is interacting with the electron [57].
More complex calculations are also taking many-body effects with the inner nucleons into account. Tomaselli and co-workers [58] used the Dynamic Correlation Model (DCM), where a single valence or hole particle couples non-perturbatively to the reference closed-shell nucleus. Further, Sen'kov and Dmitriev [59] developed an approach based on the theory of finite Fermi systems.
The results of various model calculations of the Bohr-Weisskopf correction for $^{209}Bi^{82+}$ are listed in Tab. 2.1. The corrections show a large deviation up to a factor of two. Most values have no uncertainty associated with them, and if they do, only numerical uncertainties and no assumption of the model accuracy is given. To get a realistic uncertainty, the spread of the different models can be considered, leading to large uncertainties.
Overall, the nuclear magnetization-distribution correction represents the largest uncertainty in

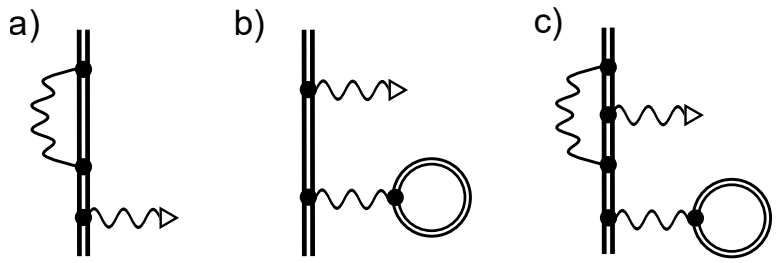

Figure 2.10: One-loop Feynman diagrams for a) *self-energy* and b) *vacuum-polarization* correction to the hyperfine splitting. There are a total of six Feynman diagrams in order α (see remaining e.g. in [65]). c) shows a Feynman diagram for a two-loop correction to the hyperfine splitting.

the hyperfine splitting calculation. In Fig. 2.9 the uncertainty of the Bohr-Weisskopf effect (red dotted line) is compared to the QED contribution. For bismuth the uncertainty is as large as the QED contribution (green dashed line) and no conclusive QED test is possible, although the experimental precision is high as indicated by the arrows.

QED Correction

The hyperfine splitting is also affected by QED effects. These consist of the already introduced effects of *self energy* and *vacuum polarization*, which in the case of H-like ions add up to the QED correction

$$\chi_{\text{rad}} = \chi_{\text{SE}} + \chi_{\text{VP}}. \tag{2.51}$$

For few-electron systems such as Li-like ions, additional QED effects have to be considered due to interelectronic interactions and screening effects of the electrons [65]. Feynman diagrams for a one-loop QED correction of the hyperfine splitting are shown in Fig. 2.10 a) and b). The straight double line indicates the bound electron, i.e. the solution of the Dirac equation, and the wavy line with triangle[4] represents the magnetic interaction. The photon propagator is denoted with the wavy line. Diagram a) shows a *self-energy* correction with the emission and reabsorption of the same photon, while b) shows the correction for a coupling to a virtual electron-positron pair, visualized by the closed loop (*vacuum polarization*).
QED calculations are based on perturbation theory in the fine structure constant α. The Feynman diagrams a) and b) of Fig. 2.10 show first-order contributions in α, called one-loop corrections. For a detailed description of one-loop QED calculations, which show a good agreement between several groups, see [2].
Besides the perturbative expansion in α, QED calculations often include an additional expansion in αZ. While this is feasible for atoms with low Z and called non-relativistic QED (NR-QED) [66], it is not applicable anymore for HCI such as H-like bismuth ($\alpha Z \approx 0.61$). In this case, αZ has to be treated in all orders by implementing the full Dirac solution in the QED calculations [3], which is represented by the double lines in the Feynman diagram in Fig. 2.10.

[4] In some literature also depicted as a dashed line with triangle.

Table 2.2: Theoretical calculation of the ground-state hyperfine splitting $\Delta E^{(1s)}$ and the specific difference ${}^{208}\Delta' E$ in H-like ^{208}Bi. For $\Delta E^{(1s)}$ the first uncertainty is due to the Bohr-Weisskopf effect and for ${}^{208}\Delta' E$ due to uncalculated terms and remaining nuclear effects. The second one is in both cases the uncertainty of the magnetic moment. The table is adopted from [11].

	$\Delta E^{(1s)}$ (meV)		${}^{208}\Delta' E$ (meV)
Dirac value	6427	Dirac value	-35.008
One-electron QED	-33	One-electron QED	-0.040
Nuclear size	$-712(4)$	$\propto 1/Z$	-33.017
Bohr-Weisskopf	$-88(30)$	$\propto 1/Z^2$	0.285
		$\propto 1/Z^3$	$-0.003(3)$
		Screened QED	0.213(2)
Total	5594(30)(12)	Total	$-67.491(5)(148)$

On the other hand, highly charged ions have the advantage, that complex interelectronic interactions are not present or can be treated perturbatively by expansion in $1/Z$. For Li-like bismuth this effect is evaluated to first and second order [9].
For a further increase in precision, calculations in order α^2 (two-loop effects) have to be considered. Here the contributions can be sorted into second-order *vacuum polarization*, mixed *self energy-vacuum polarization* (one combination is shown in Fig. 2.10c) and two-photon *self energy* [3]. In total 50 different Feynman diagrams have to be derived and calculated (see Fig. 21 in [2]). For calculations of two-loop effects see [67].

2.4.3 Specific Difference for QED Tests

The strong model dependence of the Bohr-Weisskopf effect (see Sec. 2.4.2) introduces a large uncertainty into the hyperfine splitting calculation, which strongly masks QED effects (see Fig. 2.9).
In case of H-like ^{208}Bi, the uncertainty of the recent calculation [11] is as large as the total QED contribution, which can be seen in Tab. 2.2. The first uncertainty is mainly due to the Bohr-Weisskopf effect and the second is due to the magnetic moment. The uncertainty of the QED calculation is negligable compared to the other effects. Therefore, the identification of QED effects and the verification of the theory by comparison with high precision experimental results is not feasible.
To circumvent this limitation Shabaev and co-workers proposed in [7] to consider the specific difference of the ground-state hyperfine splitting of H- and Li-like charge states of the same isotope

$$\Delta' E = \Delta E^{(2s)} - \xi \Delta E^{(1s)}. \tag{2.52}$$

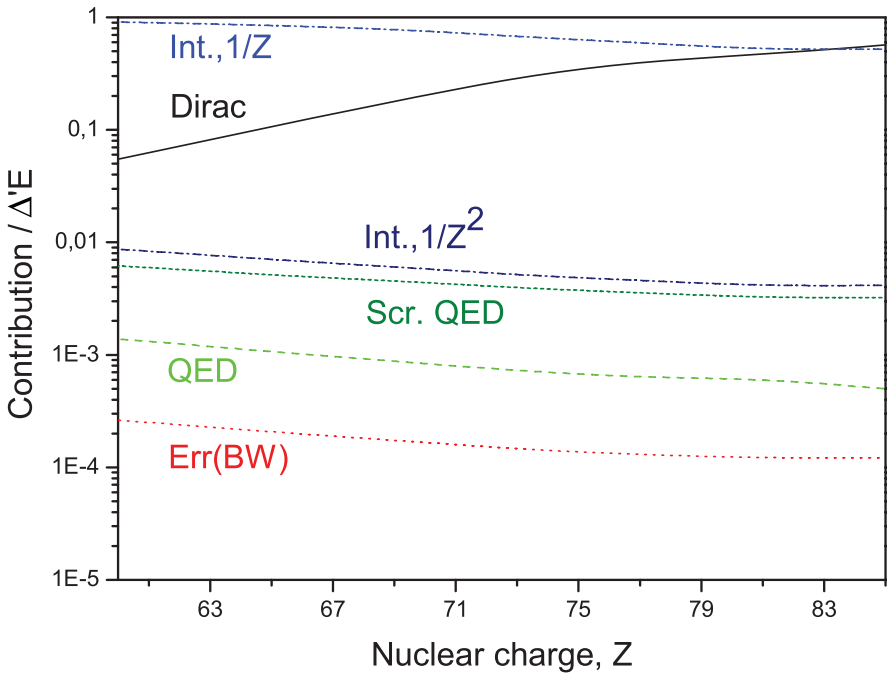

Figure 2.11: Relative contributions to the specific difference of the ground-state hyperfine splitting in hydrogen- and lithium-like ions. The uncertainty caused by the Bohr-Weisskopf effect is significantly lower than the QED contribution, which enables experimental tests. (From Volotka et al. [64]. Reproduced by permission of Wiley.)

The parameter ξ can be chosen such that the magnetization distribution of the joint nucleus cancels. This is possible, because the Bohr-Weisskopf effect depends on the electronic structure only through the radial components of the Dirac wave function of the electron. The ratio of these components can be calculated with high accuracy for H- and Li-like ions. Therefore, ξ can be derived almost independent of the nuclear structure. For bismuth, a value of $\xi = 0.168\,86$ largely cancels the Bohr-Weisskopf effect [64].
The results of the calculation of the specific difference of ^{208}Bi [11] can be found in Tab. 2.2. The first uncertainty is the theoretical uncertainty including uncalculated interelectronic interactions of order $1/Z^3$ and screening contributions of the Li-like ion. Uncertainties due to nuclear effects are not listed, since they almost completely cancel. This shows that the specific difference leads to a significant reduction of the uncertainty caused by the Bohr-Weißkopf effect, which can also be seen in Fig. 2.11.
The larger and now limiting contribution is the second uncertainty due to the nuclear magnetic moment. This emphasizes the importance of accurate knowledge of the magnetic moment for QED tests. Ideally, improved measurements are performed directly on H-like ions instead of Nuclear Magnetic Resonance (NMR) experiments with atoms to avoid complex shielding calculations [11].
First QED tests are already possible for ^{209}Bi. The theoretical [10] and experimental [8] specific

difference for ^{209}Bi is

$$\begin{aligned} {}^{209}\Delta' E_{\text{theo}} &= -61.043(5)(30)\,\text{meV} \quad \text{and} \\ {}^{209}\Delta' E_{\text{exp}} &= -61.012(5)(21)\,\text{meV}. \end{aligned} \tag{2.53}$$

The results agree within the 1σ-range, which demonstrates a successful QED test. The dominant theoretical uncertainty is again due to the magnetic moment. However, this amounts to only $14\,\%$ of the total QED contribution in the specific difference [10].

2.5 Laser Spectroscopy

Laser spectroscopy is a powerful tool to investigate atomic and nuclear properties by precisely measuring energy levels in atoms or ions. It can be applied with respect to HCI in many different environments, e.g. in various ion traps [12, 68, 69], in dedicated collinear setups [70] or in storage rings [5] to mention only those which are of relevance for this work. The targeted ion species are equally diverse, ranging from stable isotopes, which are investigated with highest precision [71], to very exotic isotopes with short lifetimes [72]. The basic principle of laser spectroscopy, as performed in this work, is the excitation of an atomic transition with a laser providing a precisely known frequency. The laser is overlapped with the atoms or ions and suitable detectors are installed to detect resonantly scattered fluorescence photons. One way to obtain the required resonance condition is to scan the laser frequency in small steps across the atomic transition.
In this work, laser spectroscopy of the hyperfine structure in H-like ^{208}Bi and ^{209}Bi is performed in a storage ring. The expected linewidth and special aspects of laser spectroscopy in storage rings are discussed.

2.5.1 Linewidth

The precision of a laser spectroscopic method is limited by the linewidth of the resonance. The fundamental lower limit for the linewidth of a transition is called natural linewidth. It results from Heisenberg's energy-time uncertainty relation

$$\Delta E \cdot \Delta t = \hbar \Delta\omega \cdot \tau \overset{!}{\geq} \hbar, \tag{2.54}$$

due to the limited lifetime τ of the excited state. To derive the transition lineshape the excited atom or ion can be described as damped harmonic oscillator. Solving the equation of motion [48] leads to the intensity profile

$$I(\omega) = \frac{I_0}{\pi} \frac{\gamma/2}{(\omega - \omega_0)^2 + (\gamma/2)^2} \tag{2.55}$$

of a transition between two energy levels $E_i - E_f = \hbar\omega_0$. This lineshape is called Lorentzian and is centered around ω_0. The width of the Lorentzian distribution $\Delta\omega_{\text{nl}} = \gamma$ gives the full

width at half maximum (FWHM) and is related to the lifetime by $\gamma = 1/\tau$.
In experiments it is usually not possible to resolve the natural linewidth. This is due to several broadening mechanisms, which are discussed in detail e.g. in [73]. In many cases, the Doppler broadening is the most prominent mechanism. It is caused by the thermal motion of a particle ensemble resulting in different velocity classes. If a laser is now directed at this ensemble from direction x, there will be particles moving towards or away from the laser. Due to the Doppler effect, the resonance frequency is thereby effectively shifted to lower or higher values. If the particles are in a non-relativistic thermal equilibrium at temperature T, their velocity in one dimension can be described by a Maxwell-Boltzmann velocity distribution [74]

$$f(v_x) = \sqrt{\frac{m}{2\pi k_\mathrm{b} T}} \cdot \exp\left(-\frac{m v_x^2}{2 k_\mathrm{b} T}\right). \tag{2.56}$$

This is a symmetric Gaussian distribution, depending on particle mass m and Boltzmann constant k_b. Since the transition intensity is proportional to the amount of particles in a certain velocity class, few steps [48] yield

$$I(\omega) = I_0 \exp\left(-\frac{mc^2(\omega-\omega_0)^2}{2 k_\mathrm{b} T \omega_0^2}\right). \tag{2.57}$$

The transition intensity has a Gaussian distribution around the central frequency ω_0. A frequently used measure for the width of a Gaussian distribution is the standard deviation in terms of frequency $f_0 = \omega_0/2\pi$

$$\sigma_\mathrm{D} = \frac{f_0}{c}\sqrt{\frac{k_\mathrm{b} T}{m}}. \tag{2.58}$$

In general, the measured lineshape is a combination of all contributing broadening mechanisms. This results in a convolution of Gaussian and Lorentzian lineshapes, which is known as Voigt profile. However, if one mechanism dominates, the profile can be completely represented by a single component. This is the case for laser spectroscopy of relativistic ions in a storage ring. For example, the hyperfine splitting in $^{209}\mathrm{Bi}^{82+}$ with an excited-state lifetime of $400\,\mu\mathrm{s}$ leads to a natural linewidth (nl) of

$$\Delta\omega_{\text{nl, Bi}} = 2.5\,\mathrm{kHz}. \tag{2.59}$$

In contrast, the Doppler broadening can be estimated by connecting the Doppler width (2.58) with the longitudinal momentum spread [75]

$$\frac{\Delta p}{p} = \frac{\sigma_\mathrm{D}}{\beta f}. \tag{2.60}$$

For a cooled ion beam in a storage ring (sr) with a typical momentum spread of $\Delta p/p = 3\times10^{-5}$ at $\beta = 0.72$ and a laser frequency of $f = 498\,\mathrm{THz}$, the Doppler width is

$$\sigma_{\text{sr, Bi}} = 10.1\,\mathrm{GHz}. \tag{2.61}$$

Since $\sigma_{\text{sr, Bi}} \gg \Delta\omega_{\text{nl, Bi}}$, the use of a pure Gaussian distribution is justified. Moving from a storage ring towards an ion trap, where the ions have thermalized at $T = 1\,\mathrm{K}$, gives

$$\sigma_{\text{trap, Bi}} = 26\,\mathrm{MHz}. \tag{2.62}$$

This results in a reduction of the linewidth by about three orders of magnitude, which also represents a massive increase in precision. However, the natural linewidth is still not reached in this scenario, but further cooling techniques or special measurement techniques such as saturation spectroscopy [48] can be applied.

2.5.2 Laser Spectroscopy at Storage Rings

A storage ring with relativistic ions is a challenging environment for laser spectroscopy experiments with certain drawbacks, but also with unique advantages. The main disadvantage compared to other environments is the achievable precision. The relativistic ion velocity is determined by the electron cooler, but the measurement of the applied high voltage is limited to a relative precision of 10^{-5} (more information in Sec. 3.2.1). In addition, the ion ensemble has a rather high temperature as mentioned in the previous section. To counteract such effects, the collinear laser spectroscopy method [76] can be used in some experiments to partially eliminate uncertainties due to the ion velocity. However, the precision of trapped cold ions can never be achieved.
One advantage of a storage ring experiment at an accelerator facility is the availability of exotic ions with high charge states. Although the achievable ion production efficiencies are limited, the stored circulating ions can interact many times with a laser, which increases the ion current significantly. For 10^6 ions revolving at $2\,\mathrm{MHz}$ in the storage ring an ion current of $2 \times 10^{12}\,\mathrm{ions/s}$ is obtained, which corresponds to $26\,\mu\mathrm{A}$ for H-like bismuth.
Furthermore, the Doppler effect, due to the relativistic ion velocity, can be exploited to shift the laser wavelength λ_{lab} in the ion rest frame (λ_0). The Doppler effect depends on the angle θ between the laser and the ion beam and is given by

$$\lambda_0 = \frac{\lambda_{\mathrm{lab}}}{\gamma(1 - \beta\cos\theta)}. \tag{2.63}$$

By choosing the orientation of the laser to be co-propagating ($\theta = 0°$) or counter-propagating ($\theta = 180°$) with respect to the ion beam, the shift direction can be chosen. This can be used, for example, to target an ultraviolet transition at $243\,\mathrm{nm}$ and an infrared transition at $1554\,\mathrm{nm}$ with the same ion velocity and a laboratory wavelength around $600\,\mathrm{nm}$ [8]. Moreover, it is possible to excite transitions in the ultraviolet or infrared region that otherwise cannot be directly excited with conventional laser systems.

3 Experimental Setups

3.1 Production of Highly Charged Ions

There are two main options to produce highly charged ions (HCI) in the laboratory. The first possibility is a table top ion source such as an *Electron Cyclotron Resonance Ion Source* (ECRIS) [77] or an *Electron Beam Ion Source/Trap* (EBIS/T) [78]. Such ion sources are rather easy to operate and can be used for a variety of experiments, e.g. in-trap spectroscopy [61], as source for high precision mass measurements [79] or g-factor determination [80]. The limitations are arising when moving to heavy highly charged ions ($Z > 80$). In this regime, technically challenging electron energies above $100\,\mathrm{keV}$ are required to remove all electrons from an ion. The production process of bare and few electron systems is not efficient in such machines, resulting in only a few ions in the desired charge state. In addition, only stable or long-lived isotopes can be used.
To overcome these limitations, accelerator facilities such as the GSI Helmholtzzentrum für Schwerionenforschung in Darmstadt can be used. Here, ions are accelerated almost to the speed of light and then focused onto dedicated targets. In the subsequent reaction, the highest charge state of any element up to uranium can be produced in significant quantities. Additionally, the production of rare and short-lived isotopes opens up the possibility of unique experimental studies.
For the commissioning of the HITRAP Cooling Trap an EBIT is used, while for the future operation of the trap and for laser spectroscopy on bismuth the GSI accelerator complex is utilized. Both are described in more detail below.

3.1.1 Electron Beam Ion Trap (EBIT)

The ion production in an EBIT is based on electron impact ionization. Electrons are generated at a negative potential cathode and are accelerated towards the trap region, which is biased on positive potential. The electrons are guided and compressed along the trap axis by a strong magnetic field until they are electrostatically repelled onto a collector. Typical settings for the SPARC-EBIT [81], which is used to commission the HITRAP Cooling Trap, are electron energies of a few keV and an electron current of about $20\,\mathrm{mA}$.
Within the trap region, which consists of two endcaps and a central electrode, the electrons interact with atoms and molecules in the ultra-high vacuum environment. In the process, bound electrons can be removed by impact ionisation. The created ions are confined radially by the negative space charge potential of the electron beam and longitudinally by an electric potential of the trap endcaps. The production of high charge states is counteracted by the

effects of charge exchange and recombination. Thereby, trapped ions capture electrons from the electron beam or from lower charged particles.
Depending on the storage time, different charge state distributions are present. In general, a longer storage time leads to a higher charge state. This is called *charge breeding* and can be used to optimize the production of a particular ion charge state. After the storage time, the ions can be ejected by rapidly switching the voltage of an endcap electrode. To separate individual charge states from the ejected bunch, an additional component or method has to be used. This can be, for example, a Wien filter, separator magnet or the separation by charge- and mass-dependent flight times.
To ionize the element of interest, it has to be introduced into the vacuum of the EBIT. This is easy for gaseous elements or molecules. A high-pressure gas reservoir is connected to the ultra-high vacuum via a needle valve and the supply is constantly regulated. An extension to other elements facilitates the MIVOC method, where the vapor of liquids is injected into the EBIT [82]. Injection and charge breeding of externally produced ions is also possible, but more demanding.

3.1.2 GSI Accelerator Complex

The GSI accelerator complex (shown in Fig. 3.1), including the Heavy Ion Synchrotron (Schwer-Ionen Synchrotron SIS18) and the Experimental Storage Ring (ESR), is in operation since the early 1990's. The facility provides a variety of ion beams in all charge states up to U^{92+} [4]. This section provides details on the ion production and the individual accelerator steps. The production of the rare bismuth isotope ^{208}Bi is used as an example, since it is the target isotope for the laser spectroscopy presented later.
The starting point of the accelerator chain is an ion source. There are different types of ion sources that can be used at GSI, installed at three different terminals. For bismuth either the Penning Ionization Gauge (PIG) ion source [83] or a Metal Vapor Vacuum Arc (MeVAC) source is commonly used. The latter provides higher ion currents but could not be used in this work. Therefore the PIG source is used, in which electrons are generated and accelerated by high voltages to form a plasma. In the plasma, a support gas such as argon is ionized by electron impact and accelerated towards the cathode, which consists of naturally abundant ^{209}Bi. Bismuth is sputtered from the cathode and also ionized by the electron plasma. The ions can be extracted from the source at a high positive potential and accelerated towards ground potential [84].
Only Bi^{4+} ions are selected in a magnetic separator and injected into the UNIversal Linear ACcelerator (UNILAC) [85] at $2.2\,\mathrm{keV/u}$. The UNILAC consists of an RFQ, an interdigital H-type LINAC (IH-DTL), a gas stripper for higher charge state production followed by Alvarez-type cavities. Along this $120\,\mathrm{m}$ long chain, the bismuth ions are accelerated stepwise by high-frequency electric fields of $36\,\mathrm{MHz}$ and $108\,\mathrm{MHz}$. The final UNILAC beam energy is $11.4\,\mathrm{MeV/u}$, corresponding to a velocity of $16\,\%$ of the speed of light.
For a more efficient acceleration, the charge state of the ions is increased twice before injection into the SIS18. The first time in the gas stripper target behind the IH-DTL and once again in a solid stripper target in the transfer channel (TK) after the UNILAC. Here the intermediate

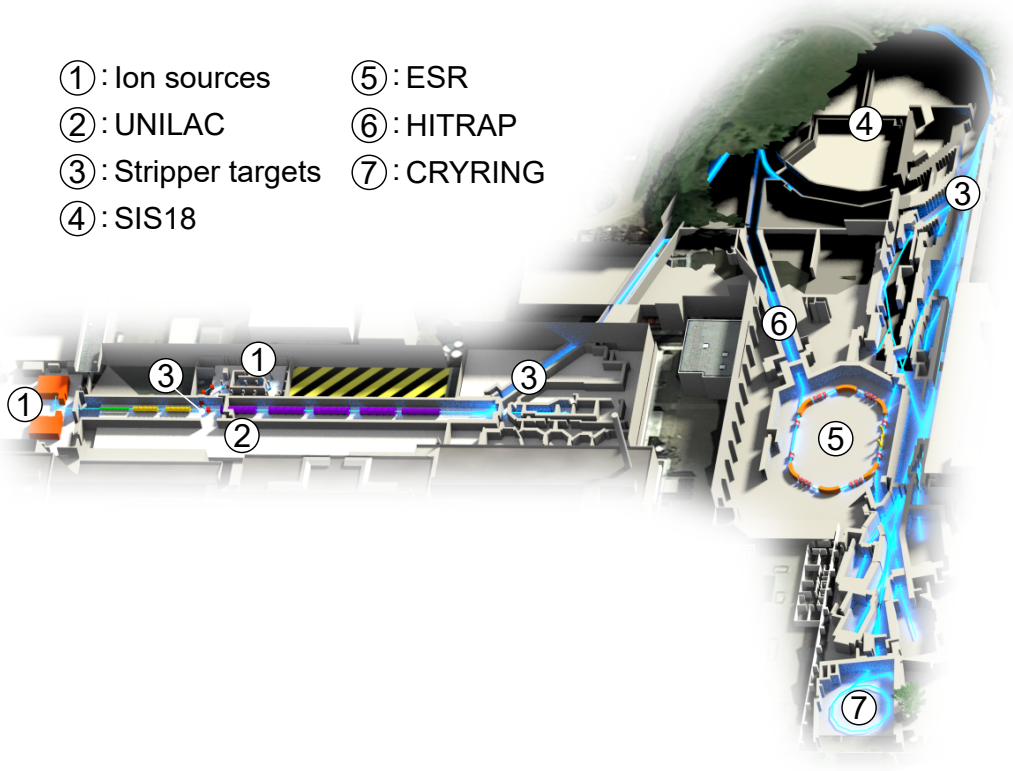

Figure 3.1: Overview of the GSI accelerator complex (modified from [86]). Ions are produced in different ion sources and first accelerated in the UNIversal Linear ACcelerator (UNILAC). Further acceleration to high relativistic energies takes place in the Heavy Ion Synchrotron (SIS18). From there, ions can be distributed to different experimental areas or storage rings. The blue lines indicate possible ion trajectories.

charge state of Bi^{68+} is reached. Inside the targets, the bound projectile electrons are stripped off by impact ionization with electrons in the target. This can be understood as an inverse process compared to an EBIT, where the ions are at rest and the target electrons are at high velocity.
After acceleration in the UNILAC, the ions are injected into the synchrotron SIS18. This ring accelerator has a circumference of $216\,\mathrm{m}$ and a magnetic rigidity of $18\,\mathrm{Tm}$. Within SIS18, ions are accelerated by RF cavities up to final energies in the $\mathrm{GeV/u}$ range. To increase the number of stored ions, several consecutive UNILAC bunches can be injected and accumulated in SIS18 [87]. During acceleration, the dipole magnets are ramped up synchronously with the increasing energy of the particles in order to maintain a stable orbit.
For the laser spectroscopy experiment on ^{208}Bi about 10^8 primary $^{209}Bi^{68+}$-ions are accumulated and accelerated to $550\,\mathrm{MeV/u}$. All ions can be ejected from the ring in one revolution by fast pulsing of kicker magnets. The ions are then focused onto the final stripper target, where the

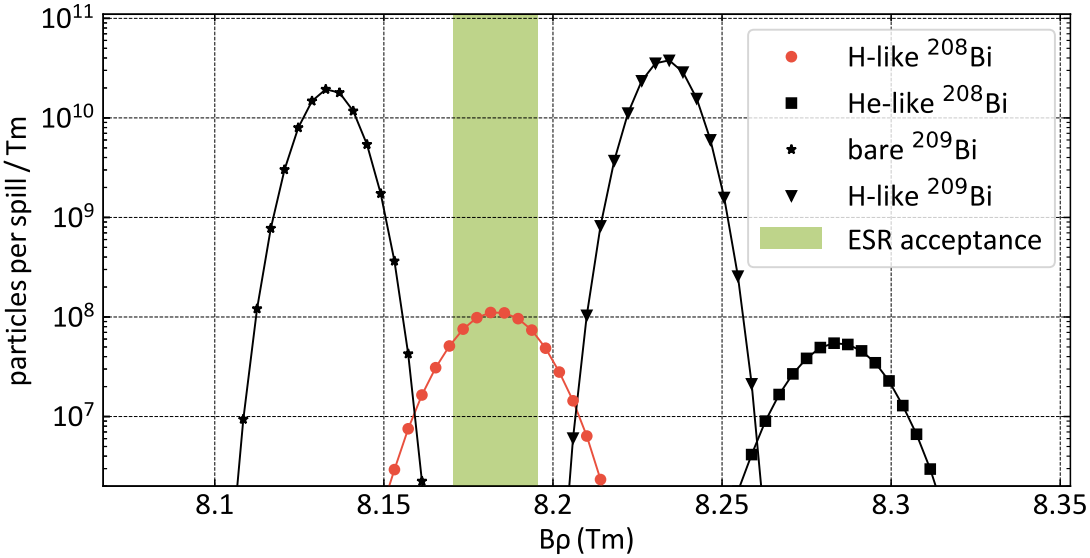

Figure 3.2: *LISE++* simulation by Y. Litvinov for produced bismuth isotopes and charge states per spill in the stripper target between SIS18 and ESR assuming 10^8 ions ejected from SIS18. The injection acceptance of the ESR (green area) can be adjusted to store a maximum amount of $^{208}Bi^{82+}$.

isotope and charge state for the experiment is produced.
At this point the stripper material and thickness is important for the efficiency of the process [88]. In a thick target the charge state distribution is given by an equilibrium of ionization and electron capture processes. For relativistic ions the final charge state depends only on the proton numbers of projectile and stripper and the exit energy, but not on the initial charge state. At sufficient energies, as reached after SIS18, this results in a dominant production of bare or H-like ions. However, a thick target also means more ion loss and worse beam quality. Therefore, a compromise between charge state distribution and ion loss has to be found. Especially, if an experiment requires H-, He- or Li-like ions, a thinner stripper foil can be advantageous [39].
The situation changes if, in addition to stripping, a nuclear reaction is required, to produce a rare isotope. In order to optimize the process of projectile fragmentation, a thicker foil is needed.
For the $^{208}Bi^{82+}$ experiment, a thick beryllium foil with $1850\,\mathrm{mg/cm^2}$ was chosen by the operators, in order to optimize the production. After the stripper foil the secondary beam, consisting of different charge states and isotopes, has an energy of $411\,\mathrm{MeV/u}$ and is transported towards the ESR. In Fig. 3.2 a *LISE++* simulation by Y. Litvinov of the bismuth isotopes and charge states produced per spill is shown.
By adjusting the magnetic rigidity of the ESR, different ion species produced in the stripper target can be selected for storage. The green area in Fig. 3.2 indicates the ESR injection acceptance of about $0.025\,\mathrm{Tm}$ and an estimation of the maximum amount of $^{208}Bi^{82+}$ ions

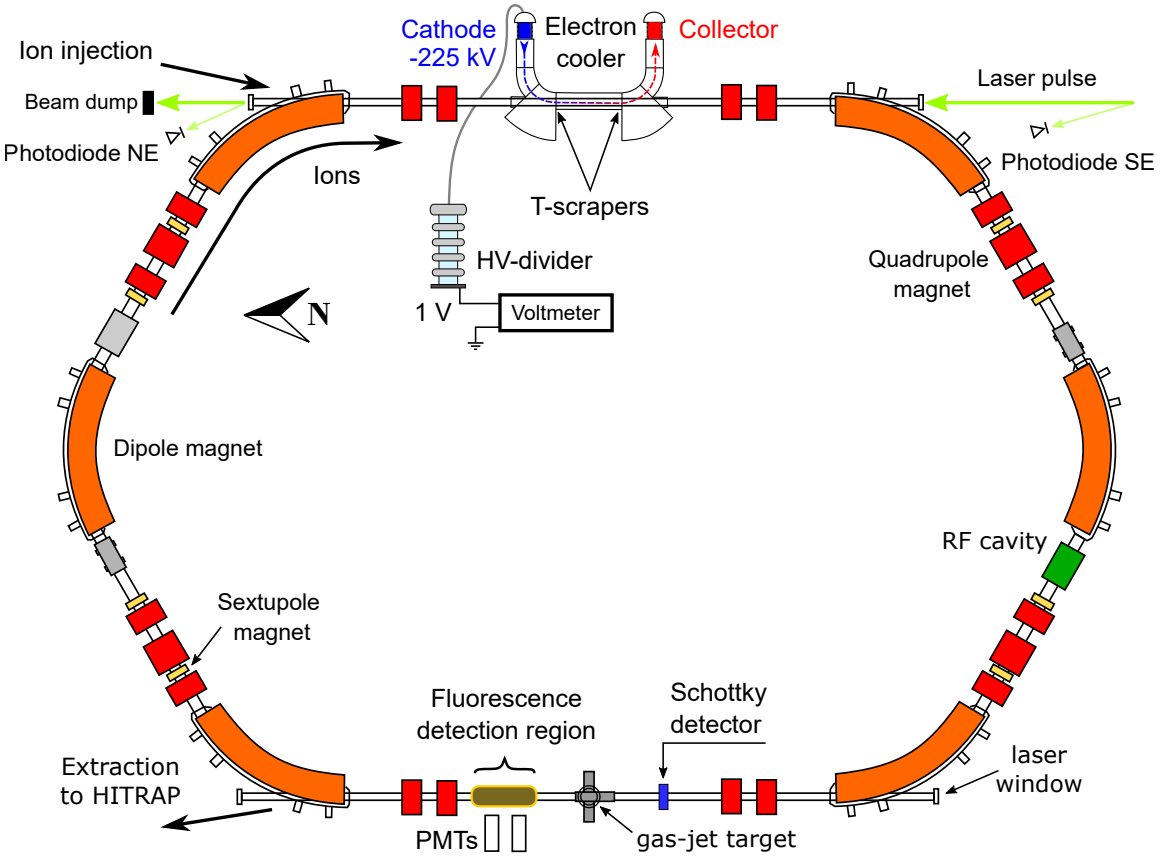

Figure 3.3: Schematic view of the Experimental Storage Ring (ESR). The ESR has a circumference of $108.4\,\mathrm{m}$ and ions are deflected by six dipole magnets (orange). Laser windows allow laser spectroscopy of stored ions in the straight sections of the ESR. The schematic is modified from [89].

results in 2×10^6. This is more than two orders of magnitude less than for the bare or H-like charge states of stable ^{209}Bi, whose production does not involve a nuclear reaction. In addition to the bismuth isotopes, also other elements are produced in the process and are stored in the ESR as contaminant ions if they coincide with the acceptance window.

3.2 Storage Ring ESR

The Experimental Storage Ring (ESR) at GSI is a $108.4\,\mathrm{m}$ long storage ring for highly charged ions with a magnetic rigidity of $10\,\mathrm{Tm}$. In the ESR, for example, fully ionized uranium U^{92+} can be stored in an energy range from $3\,\mathrm{MeV/u}$ to $550\,\mathrm{MeV/u}$ [39]. A schematic view of the ESR is shown in Fig. 3.3 and some properties are listed in Tab. 3.1.
The ions are injected in the northeast section of the ESR and are guided by a total of six dipole

Table 3.1: Properties of the Experimental Storage Ring (ESR) [39].

Circumference	$108.4\,\mathrm{m}$
Magnetic rigidity	$10\,\mathrm{Tm}$
Beam energy U^{92+}	3 - $550\,\mathrm{MeV/u}$
Beam cooling	stochastic, electron
Operation mode	bunched, coasting
Vacuum	$< 10^{-10}\,\mathrm{mbar}$

magnets. Each of them deflects the ion beam by 60°. The magnet arrangement allows for two $18\,\mathrm{m}$ long straight sections that can be used for experiments and electron cooling. The ion-optical lattice also includes quadrupole magnets in duplet and triplet arrangements and sextupole magnets for higher order corrections [4]. The ESR can perform a variety of tasks such as beam accumulation for in-ring experiments or deceleration and extraction to the low-energy facilities Cryring@ESR [90] and HITRAP [14].
The ESR can be operated in coasting- or bunched-beam mode. Without further measures, the ions will revolve in a continuous beam. An integrated RF cavity can be used to bunch the ions at the injection energy or to accelerate or decelerate the beam analogous to a synchrotron.
The advantage of the bunched-beam mode is the compression of the ions into a shorter time window. This can be beneficial for background suppression or for the temporal overlap with a laser pulse. On the other hand, a bunching force can affect the ion velocity. If the bunching frequency has a mismatch to the electron cooler voltage, this leads to an uncontrolled change of ion velocity, which can introduce systematic shifts as will be discussed in Sec. 5.6.5.
Due to its ion-optical structure, the ESR is well suited for laser spectroscopy experiments, which have been performed for a long time [5]. Four windows are installed in the ESR vacuum system as access points for the laser beam, located at the beginning and end of the two straight sections (see Fig. 3.3). The laser-ion overlap can be realized over the entire length of the section and is adjusted with scraper pairs. Depending on the targeted transition, the laser-ion overlap can be realized in collinear or anti-collinear geometry to take advantage of the relativistic Doppler effect (Eq. 2.63).
A region for single-photon detection is installed in one of the straight sections close to the target. It consists of a mirror system and photon detectors for different wavelength regimes (see Sec. 3.2.4). If the laser experiment probes a transition that is fast with respect to the ion revolution time, the laser is introduced into the section with the detection region in order to efficiently detect fluorescence photons [35]. For longer lifetimes of the excited states the other section is more suitable, because of the absence of laser background during detection.
Important elements of the ESR that determine the sensitivity and accuracy of laser spectroscopy will be discussed in more detail in the following sections.

3.2.1 Electron Cooler

The electron cooler of the ESR is a crucial part for the storage ring operation and also for high precision measurements, since it improves the beam quality, reduces the ion velocity distribution and determines the average beam velocity. The HCI injected into the ESR have a rather poor emittance due to the previous preparation steps and the production of the high charge state in the stripper foil. Over time, the emittance of stored ions will continue to grow because of residual gas or intrabeam scattering. This eventually leads to ion loss and significantly limits the beam lifetime.
To counteract this mechanism and to improve the beam quality, electron cooling (see Sec. 2.3.1) is applied in most cases directly after injection. Therefore, an electron beam is superimposed with the revolving ion beam over a distance of about $2.5\,\mathrm{m}$ in a straight section of the ESR (see Fig. 3.3). The electron beam is generated by a heated tungsten cathode that is coated with barium to increase the electron-emission efficiency. The cathode is at a high negative potential, which accelerates the electrons toward the ion beam line. Magnetic fields of a solenoid guide the electrons to achieve an overlap with the ion beam. After the interaction section the electrons are again separated from the ion beam by the field of a second solenoid and directed to the collector on the high voltage platform to minimize power dissipation. Some important properties of the electron cooler are listed in Tab. 3.2.
The most important aspect for cooling is the fact that the electrons are always replaced by "fresh and cold" electrons, while those electrons carrying the excess energy of the ion beam are dumped. The electron beam current can reach up to $1\,\mathrm{A}$ and the maximum electron energy is $230\,\mathrm{keV}$ [39]. According to Eq. 2.27, a higher current would result in a shorter cooling time. This is in conflict with the ion losses that occur, mainly due to recombination effects with the free electrons [91]. During the laser spectroscopy experiment described in this work the current was set between $50\,\mathrm{mA}$ and $200\,\mathrm{mA}$ as a compromise between long beam lifetime and efficient cooling.
The ion velocity ($v_{\mathrm{ion}} = \beta_{\mathrm{ion}} c$) after thermalization can be deduced from the acceleration potential U_{EG} of the electrons by

$$\beta_{\mathrm{ion}} = \beta_{\mathrm{e}} = \sqrt{1 - \left(1 + \frac{eU_{\mathrm{EG}}}{m_{\mathrm{e}}c^2}\right)^{-2}}. \tag{3.1}$$

For the laser spectroscopic measurements on ^{208}Bi an accelerating potential of $U_{\mathrm{EG}} = 225\,440\,\mathrm{V}$ is used, which corresponds to an ion velocity of $0.72\,\mathrm{c}$.
A direct and accurate measurement of such high voltages is currently not possible. Instead, the high voltage is scaled down to an accessible range by a long chain of resistors in a high-voltage divider [92]. At the ESR a *HVS 250*[1] high voltage divider is used. The divider ratio of this device is $248\,517$ resulting in a divided voltage of about $0.9\,\mathrm{V}$ [93]. This voltage can be easily measured with a high precision voltmeter. Such setups can achieve a precision of $10\,\mathrm{ppm}$. This is the most accurate method for measuring the ion velocity at the ESR. However, as will be discussed in Sec. 5.6.3, this level of accuracy is still the origin of the largest uncertainty for

[1] Ohmlabs, Serial No.: 17060

Table 3.2: Properties of the ESR electron cooler [39].

Electron energy	1.6 - 230 keV
Electron current	0.001 - 1.0 A
Electron beam radius	25.4 mm
Length of cooling section	2.5 m
Magnetic field strength	0.01 - 0.11 T
Cathode temperature	$\approx$ 1000 K
Space charge correction	$-0.16\,\mathrm{V/mA}$

laser spectroscopy. In addition, space-charge and contact potentials on the electron beam are shifting the ion velocity, which are also covered in Sec. 5.6.3.

For a horizontal and vertical position measurement of the ion beam, a T-scraper is integrated into the electron cooler layout in front and after the electron-ion overlap section. The T-shaped metal plate can be remotely driven into the ion trajectory during an experiment. It is also a tool for laser alignment, if laser spectroscopy is performed on the electron cooler side.

3.2.2 Beam Diagnostic

Beam diagnostic elements are an essential tool for storage rings. There are a variety of detectors that measure beam properties such as current, position, profile, etc. Without suitable detectors a storage ring operation would not be possible. For this work, the current transformer and the Schottky detector are of particular interest.

Current Transformer

The ion beam current I_{beam} is an important parameter for a storage ring. It is directly related to the number of stored particles N_{ion} with charge state q

$$I_{\mathrm{beam}} = \frac{qeN_{\mathrm{ion}}}{T_{\mathrm{rt}}} = qeN_{\mathrm{ion}} \cdot f_{\mathrm{rt}}. \tag{3.2}$$

The current is defined by the number of charges per unit of time. In a storage ring the ions revolve with a high frequency f_{rt} and pass the same plane again after the round-trip time T_{rt}, effectively increasing the ion current. This is not only advantageous for experiments but also for the non-destructive detection with a current transformer.
The measuring principle of a current transformer is the detection of currents induced by the ion beam. A highly permeable ring with a coil wound around it, is mounted directly on the

vacuum beam pipe. The ions induce a current in the coil, which can be measured as a voltage drop across a resistor and is proportional to the number of revolving ions. This method can be applied not only to a bunched beam, but also to a coasting beam where the ion beam induces a constant background with a more complex setup. Detailed information for both versions can be found in [94].
The current transformer used in the ESR includes a measurement setup for bunched- and coasting-beam mode and is sensitive to ion currents from hundreds of mA down to single µA [95]. Despite the magnetic shielding, the measurement is sensitive to external magnetic fields from nearby storage ring magnets and has to be calibrated for different storage ring settings (see Sec. 5.6.4).

Schottky Detector

The principle of Schottky detection is the non-destructive measurement of ion-induced currents. For a bunched beam, the individual ion bunches can be detected directly and the signal is proportional to the total amount of charges. For a coasting beam, the current is continuous and the measurement relies on the beam noise (Schottky noise). This noise is caused by statistical fluctuations in the beam current, due to the discrete number of charged ions revolving in the ring. After signal acquisition and amplification, a Fourier analysis is performed to extract the frequency spectrum including the higher harmonics of the mean revolution frequency [96].
The pick up can be realized with conductive plates close to the ion beam or with a microwave cavity placed around the beam pipe, where resonant modes can be excited by the Schottky noise. The higher sensitivity of the latter method allows the measurement at much higher harmonic numbers and thus increases the absolute frequency resolution. This detection scheme is utilized in this work, using a microwave cavity with a resonance frequency of about $245\,\mathrm{MHz}$ [97].
Since the revolution frequency of the ions is directly related to their mass-to-charge ratio, the Schottky detector can be adopted for mass and decay spectroscopy of in-flight produced exotic ions. The sensitivity of the method is sufficiently high to perform such experiments even on single ions [98, 99]. It is also used in this work, to identify the fragments stored in the ring and to select the target isotope ^{208}Bi.
In Fig. 3.4 a typical Schottky spectrum of the preparation of a bunched $^{208}\mathrm{Bi}^{82+}$ beam is shown. A total of four harmonics (121 to 124) of the ion revolution frequency of about $2\,\mathrm{MHz}$ are visible. Each harmonic is close to the resonance frequency of the microwave cavity and has redundant information, but differs in amplification. The color coding depicts the amount of ions circulating at the corresponding frequency. Dark blue represents no ions, while red displays the highest amount of ions.
The injection of ions into the ESR marks the beginning of the time axis (1). There, the ions cover a comparatively large frequency band, translating to a broad longitudinal momentum distribution. To reduce this, electron cooling is applied immediately after injection and the cooling effect narrows the frequency distribution. After about $100\,\mathrm{s}$, different single lines can be distinguished. Each line represents one isotope with a certain charge state. At time (2) the ion orbit is changed to optimize the beam position in the detection region. Since the path

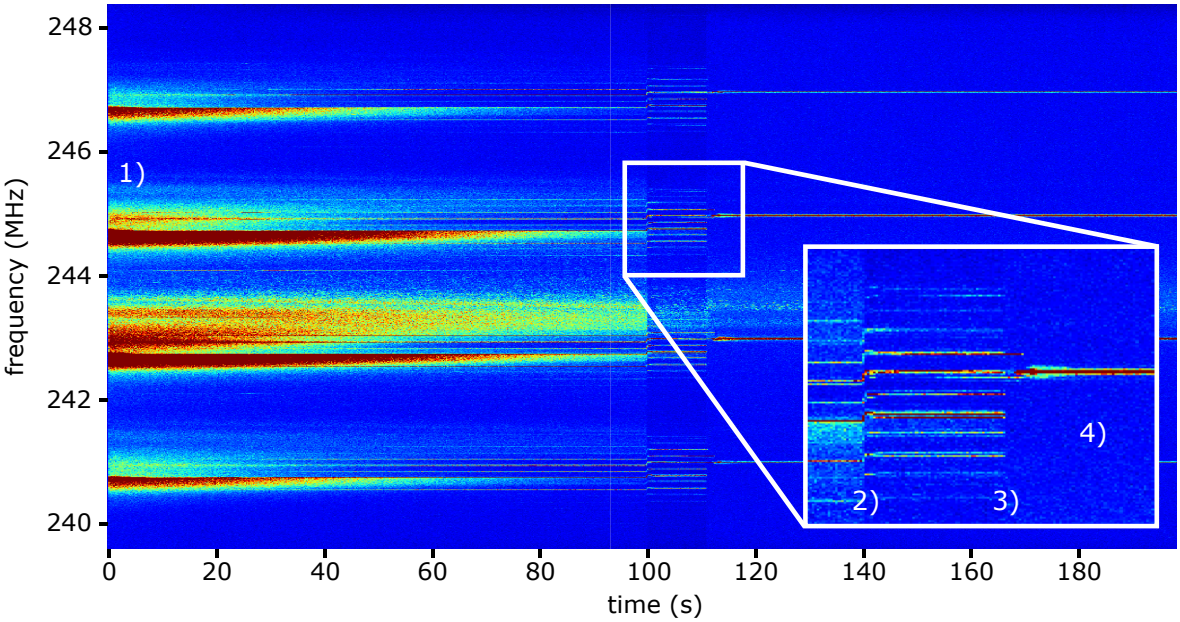

Figure 3.4: Schottky spectrum of the preparation of a bunched $^{208}Bi^{82+}$ beam for laser spectroscopy. Point 1) marks the ion injection, 2) the orbit change, 3) the scraping of contaminant ions and 4) the start of the measurement phase. After injection, the ion beam is directly cooled and the frequency distribution of the ions is narrowed. See text for more information. Data extracted and provided by S. Sanjari [100].

length along the ring is changed, while the ion velocity remains constant, the ion frequency changes as well.
At this stage, the unambiguous assignment of isotopes by their frequency-to-mass relationship allows the selection of the isotope and charge state of interest. In addition, the different ion species are spatially separated from each other. This allows the removal of contaminant ions by moving scraper plates into the ESR. Blocking of all but one isotope is visible at point (3). After two minutes of beam preparation, the laser spectroscopic experiment can begin. For the duration of the experiment, which is typically about $30\,\mathrm{min}$, the electron cooler is on and the storage ring settings are kept constant. The Schottky spectrum shows a single line in this period, which slowly decreases in intensity (4). This is related to the beam lifetime in the ESR.

3.2.3 Laser System

For laser spectroscopy at the ESR, there is a dedicated laser laboratory next to the storage ring. Different laser systems can be installed there and the light can be guided through special openings into the ESR cave. There, the laser can be transported further via enclosed beamlines to one of the four laser windows.
Laser spectroscopy of H-like bismuth is performed using a combination of a pulsed Nd:YAG

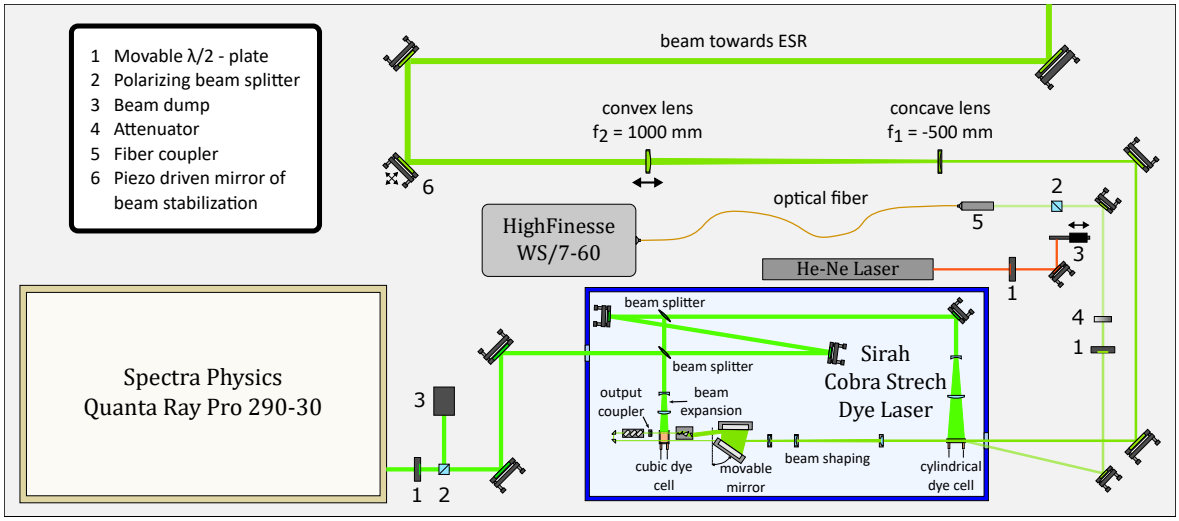

Figure 3.5: Schematic of the laser setup used for ^{208}Bi. The pulsed laser light for spectroscopy is generated by a dye laser that is pumped by a Nd:YAG laser. The light with a wavelength of $549\,\mathrm{nm}$ ($602\,\mathrm{nm}$ for ^{209}Bi) is collimated on the laser table by an adjustable telescope to reach a beam size of $1\,\mathrm{cm}$ at the overlap region in the ESR $50\,\mathrm{m}$ away. The laser wavelength is continuously measured by a WS/7-60 wavelength meter.

laser and a dye laser. The Nd:YAG laser serves as pump laser and supplies ns-pulses with the required high laser power. The dye laser acts as a spectroscopy laser and allows the wavelength scanning in different wavelength ranges. Both laser systems and parts of the beam transport are shown schematically in Fig. 3.5.

The pump laser is a Spectra Physics Quanta-Ray Pro-290-30. Short laser pulses below $10\,\mathrm{ns}$ are generated by Q-switching of a Pockels cell, which abruptly increases the quality of the resonator. The resonator contains two Nd:YAG rods, which are individually pumped by flash lamps and serve as the active medium. The flash lamps are triggered at a rate of $30\,\mathrm{Hz}$, saturating the active medium by depositing energy. As long as the Q-Switch is not activated, high losses within the resonator will prevent amplification by stimulated emission and the light output by spontaneous emission is low. When the Q-switch is active, the light intensity in the resonator rapidly increases by stimulated emission and the energy in the active medium is converted into coherent photons. The result is a short pulse of $1064\,\mathrm{nm}$ wavelength, which is further amplified by two similar Nd:YAG rods to energies up to $1.6\,\mathrm{J}$. The final stage of the pump laser consists of a potassium-dideuterium-phosphate (KDP) crystal. Here the wavelength of the light is transformed by second harmonic generation to $532\,\mathrm{nm}$ with an efficiency of about $50\,\%$.

The pump laser is always operated at maximum power to maintain uniform conditions and to ensure stable operation. Before the pump light is guided into the dye laser, the power is regulated by a combination of a $\lambda/2$-plate and a polarizing beam splitter cube.

The spectroscopy laser is a Sirah Cobra Stretch dye laser. A $60\,\mathrm{mm}$ long grating in Littman-

Table 3.3: Properties of the used dyes.

	$^{208}Bi^{82+}$	$^{209}Bi^{82+}$
wavelength	$549\,\mathrm{nm}$	$602\,\mathrm{nm}$
dye	Fluorescein 27 + NaOH	Rhodamine 610 + 640
concn. resonator	$0.4\,\mathrm{g/l}$ + $0.2\,\mathrm{g/l}$	$0.17\,\mathrm{g/l}$ + $0.04\,\mathrm{g/l}$
concn. main amplifier	$0.05\,\mathrm{g/l}$ + $0.025\,\mathrm{g/l}$	$0.021\,\mathrm{g/l}$ + $0.005\,\mathrm{g/l}$
solvent	$80\,\%$ Ethanol + $20\,\%$ H_2O	Ethanol

configuration with $2400\,\mathrm{lines/mm}$ serves as the wavelength-selective element. When the pump light enters the dye laser, it is split into three parts of different power. The first and weakest part below $1\,\%$ is directed into the rectangular dye cell of the resonator to generate the spectroscopy laser light. The dye is excited by the laser light and can emit light of a broad wavelength range due to the manifold energy level structure. To select a specific wavelength, the motorized mirror at the end of the resonator can be remotely tilted in small increments. Together with the grating, a resonance condition is established and only photons of the selected wavelength can generate stimulated emission. The linewidth of the generated pulse depends on the line spacing and the number of lines illuminated on the grating. During the beamtime a FWHM linewidth of $9.7\,\mathrm{pm}$ or $10\,\mathrm{GHz}$ was used.
The generated light leaves the resonator and passes through polarization and beam adjustment optics into the first amplifier stage. The amplifier is located in the same dye cell as the active medium of the resonator, but vertically displaced (as indicated by the parallel offset in Fig. 3.5). The second part of the pump pulse (about $10\,\%$) is used to excite the dye at this spot and the amplification takes place in a single pass. After a telescope to correct the elliptical beam profile and collimate the pulse, the light travels through the main amplifier. This amplifier has a cylindrical shape and is pumped by the main part of the pump laser (about $90\,\%$). Due to the high peak powers, a lower dye concentration must be used in the second circulator to avoid damage to the dye cell.
With the choice of the ion velocity ($\beta \approx 0.72$) the wavelength in the laboratory frame for $^{209}Bi^{82+}$ is about $602\,\mathrm{nm}$ and $549\,\mathrm{nm}$ for $^{208}Bi^{82+}$, respectively. It is not possible to cover this range efficiently with a single dye. Therefore, two dyes are prepared in advance in two circulator systems, which are easily interchangeable during the experiment. Information on the dyes, the solvents and concentration are given in Tab. 3.3.
During the beamtime, the dye laser is typically pumped with $500\,\mathrm{mJ}$, producing an output power of $70\,\mathrm{mJ}$. A small fraction of the light is collected from a reflection produced by the main amplifier and is coupled via a multi-mode fiber into a WS/7-60[2] wavelength meter for continuous wavelength monitoring. If necessary, a calibrated helium-neon laser can be coupled into the wavelength meter for calibration.
After a final beam shaping telescope on the laser table, the laser pulse is guided about $50\,\mathrm{m}$

[2]HighFinesse, Serial No.: 481

to the ESR. The beam path in air is given by eight highly reflective 2" mirrors and is mostly covered by black plastic pipes. On the southeast side of the ESR (see Fig. 3.3) the laser is coupled into the vacuum system through a kodial glass viewport.
The laser beam size in the overlap region is about $1\,\mathrm{cm}$, sufficiently large for a good spatial overlap with the mm-sized ion beam. The laser position is stabilized throughout the experiment by a laser beam stabilization system from *MRC-Systems*. For this purpose, one mirror on the laser table and one mirror in front of the ESR are equipped with a piezo drive. In addition, a fraction of the laser pulse is monitored on a position sensitive detector (PSD) in the vicinity of each piezo driven mirror. A fast controller is used to stabilize the position on the PSDs and thus the laser position in the ESR.

3.2.4 Fluorescence Detection

In the straight western part of the ESR (see Fig. 3.3) a special detection region for emitted fluorescence light is installed for laser spectroscopy experiments. Three different types of detectors are installed here. These are optimized either for infrared [101], visible and UV [102] or XUV [103] photons. The former two are based on Photo-Multiplier Tubes (PMT) while the latter one is based on a Micro-Channel Plate (MCP)[3]. For the bismuth experiment, the detection is located on the opposite side of the laser-ion overlap region, resulting in a measurement free of laser-induced background. The spatial separation of excitation and detection is possible, because the lifetime of the upper hyperfine state [52] is two orders of magnitude longer than the ion revolution time.
Relativistic effects influence the light emission of ions traveling near the speed of light and have to be taken into account in the detection scheme. While the fluorescence light is emitted isotropically in the rest frame of the ions, it appears boosted in the forward direction in the laboratory frame. This effect leads to a change in the detected intensity ratio. The angle of detection θ_{lab} for a stationary observer and the intensity ratio can be calculated as

$$\theta_{\mathrm{lab}} = \arccos\left(\frac{\cos\theta_{\mathrm{ion}} + \beta}{1 + \beta\cos\theta_{\mathrm{ion}}}\right) \tag{3.3}$$

$$\frac{I_{\mathrm{lab}}}{I_{\mathrm{ion}}} = \frac{1-\beta^2}{(1-\beta\cos\theta_{\mathrm{lab}})^2} \tag{3.4}$$

[104]. Both relations depend only on the relativistic velocity $\beta = v/c$ of the ions. In case of ^{208}Bi with $\beta = 0.72$ this implies that the photon emission in forward direction is enhanced by a factor of 38 compared to the backward direction. In addition to the angular emission characteristic, the wavelength of the fluorescence light gets a Doppler boost. According to Eq. 2.63, photons, which are emitted parallel to the ion motion, appear blue-shifted in the laboratory frame. Both effects are depicted on the right side of Fig. 3.6.
The length of the arrows represent the quantity of emitted photons in the laboratory frame and the searchlight-like structure in direction of ion motion is evident. The color coding indicates the wavelength of the photons observed. In the framework of this experiment, this results in

[3] Operating principle explained in Sec. 3.3.2

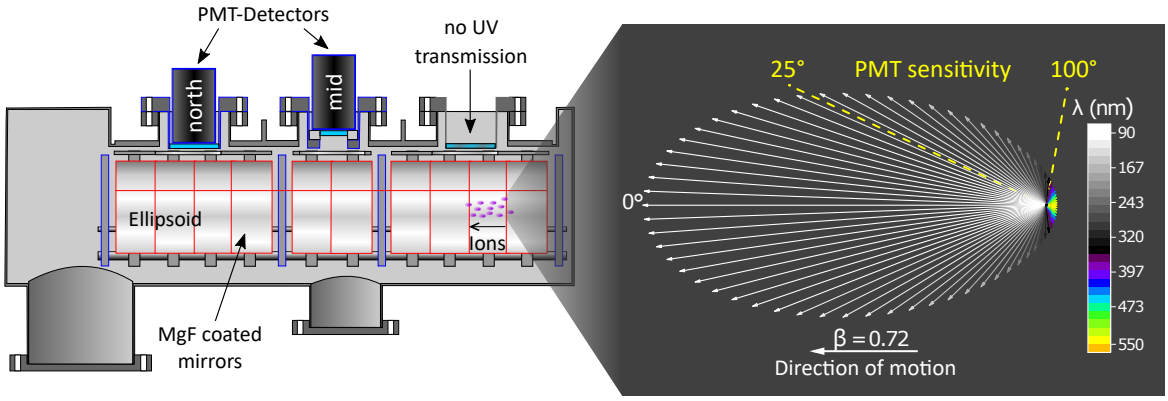

Figure 3.6: Left part: Schematic of the optical detection chamber for visible and UV light that is implemented at the ESR. The mirror system enhances the number of fluorescence photons that can be collected by the two installed Photo-Multiplier Tube (PMT) detectors. Right part: Light emission characteristics of the relativistic ^{208}Bi ions observed in the laboratory frame. The length of the arrows correspond to the intensity and the color indicates the wavelength. Angles for which the PMTs are sensitive are marked in yellow (figure modified from [89]).

fluorescence light with a wavelength range of $89\,\mathrm{nm}$ to $549\,\mathrm{nm}$ with a predominant component in the far ultraviolet.
To account for the emitted short wavelengths, two solar blind PMTs of type 9422B from ET Enterprises [105] are used for photon detection. The quantum efficiency of these detectors is above $1\,\%$ in the range between $110\,\mathrm{nm}$ and $360\,\mathrm{nm}$ with a broad maximum of about $10\,\%$ efficiency. The detection of visible photons, which constitute a large part of the photon background in the storage ring, is strongly suppressed by this choice. The PMTs are installed in air on top of magnesium fluoride viewports mounted on the detection chamber (see Fig. 3.6). The viewports have a diameter of $60\,\mathrm{mm}$ (north) and $38\,\mathrm{mm}$ (mid) and are transparent for wavelengths down to $120\,\mathrm{nm}$. Unfortunately, a third PMT viewport could not be used, because it became leaky during bake out and had to be covered with vacuum seal, making it non-transparent for short wavelengths. The installed XUV detector is also used for the experiment, but due to the high ion background signal, the data cannot be utilized for further analysis.
A mirror system inside the vacuum chamber is used to enhance the photon detection. The system consists of highly reflective metal plates arranged to direct photons with a maximum solid angle to the PMTs. Therefore, the lower part has an elliptical shape to focus the light emitted by the ion beam towards the detectors. Compared to the previous laser spectroscopy experiments on ^{209}Bi [8, 102], the mirror system has been modified. The main intention was to optimize the fluorescence detection for another experiment, aiming at laser excitation of the ^{229}Th-nucleus [106], which was scheduled a few weeks before the ^{208}Bi beamtime.
The thorium experiment was conducted under similar conditions regarding experimental setup and ion velocity, searching for a transition at about $150\,\mathrm{nm}$ [107]. The higher transition energy in the ions rest frame compared to the bismuth case, shifts the wavelength of the fluorescence

photons even further to a minimum wavelength of $60\,\mathrm{nm}$. In this regime, photons emitted at angles below $50\,^\circ$ with respect to the ion direction cannot transmit the viewports and cannot be detected by the PMTs. Therefore the tilt of the lower plates, which optimizes the photon collection for angles of $20\,^\circ$ to $60\,^\circ$, is straightened (compare Fig. 3.6 with Figure 2a in [102]). In addition, the reflective plates were replaced with magnesium fluoride coated *MIRO® 4 UV/C* plates from *Alanod*. This enhances the reflectivity for short wavelengths and the coating protects the surface from oxidation, which deteriorates the reflective properties.
It is difficult to state whether these changes have a positive or negative effect on the detection performance for the laser spectroscopy on bismuth, since other parameters (e.g. PMTs, viewports, data analysis) also differ. Nevertheless, with the results of this work, it can be claimed that the present detection region is well suited to obtain fluorescence data with good signal-to-noise ratio for H-like bismuth at very low ion numbers.

3.2.5 Data Acquisition

The data acquisition (DAQ) system has been continuously developed during the last experiments and is mainly adapted from the two previous laser spectroscopy beamtimes on bismuth. Detailed information and a scheme of it can be found in [108, 109]. Therefore, this section only provides an overview of the system and addresses the most important aspects.
The task of the DAQ is to process and store the incoming data during the experiment. The main hardware part is the so called VUPROM[4] [110] unit, that was developed by GSI. Inside the VUPROM an integrated FPGA[5] in combination with a $300\,\mathrm{MHz}$ clock allows operations with a maximum temporal resolution of $10/3\,\mathrm{ns}$. The VUPROM features two different types of input channels.
Scaler channels count incoming signals, but do not provide accurate timing information. These channels are useful to record slowly changing values such as the electron cooler current. To make such parameters accessible to the system, they are converted to a frequency.
Time-to-Digital-Converter (TDC) channels are the second type of input channel and are used, for example, for PMT signals. If a PMT signal is detected by the TDC channel, a timer is started that counts in steps of $10/3\,\mathrm{ns}$. In addition, a stop signal arrives at fixed intervals and is called common stop. Each PMT signal can thereby be referenced to the common stop and the timer increment represents the exact time difference. The common stop signal is generated by dividing the applied bunching frequency of $2\,\mathrm{MHz}$ by a factor of 90. This enables a phase-stable assignment of the photon detection to the ion position in the storage ring. In order to utilize this method also in coasting-beam mode, the master oscillator of the bunching frequency is not switched off, only the amplification is reduced to vanishing amplitude.
To avoid erroneous counts caused due to poor signal quality, the raw signals are processed in several steps before being fed into the VUPROM system. For example, the raw PMT signals are first amplified in the cave of the storage ring before being sent via long cables to the measurement room where the majority of the DAQ hardware is located. Here, among other

[4] VME Universal PROcessing Module
[5] Field Programmable Gate Array

steps, the signal is being discriminated by a Constant Fraction Discriminator (CFD) and converted to NIM[6] standard signals.
Readout of the VUPROM system is performed by the *MBS*[7] software. This software continuously reads out the accumulated data at a rate of $200\,\mathrm{Hz}$ and stores it as *MBS* events in an lmd[8] file. The usual file size of a measurement is about $300\,\mathrm{MB}$.
Besides the data that is directly fed into the VUPROM, the wavelength and the electron cooler high voltage are recorded separately. The wavelength data, including the set wavelength, measured wavelength and corresponding time stamp, is stored in a *ASCII* text file by *LabView* software at a rate of $4\,\mathrm{Hz}$. Additionally, this data is transferred via a TCP server connection to the MBS software [109] to make it available for the online analysis during the experiment. For the electron cooler high voltage a second *LabView* program is used, which frequently reads out the multimeter measurements via a TCP connection. This data is not available in real time, but is used for analysis after the beamtime.

3.3 HITRAP Facility

The goal of the Highly charged Ion Trap (HITRAP) facility at GSI is to provide heavy HCI, such as Bi^{82+} or U^{91+}, for precision experiments [13, 14]. HITRAP connects the accelerator facility to the experiments and has the task of decelerating, cooling and transporting the beam to the end user. As such, HITRAP is the first facility of its kind in the world and offers unique experimental opportunities.
After the production at relativistic energies in stripper targets (see Sec. 3.1.2), the heavy HCI are stored and cooled in the ESR. At this stage, the ions have an energy of up to $400\,\mathrm{MeV/u}$, which is two orders of magnitude higher than the acceptance energy of $4\,\mathrm{MeV/u}$ for HITRAP. Therefore, the ESR is used as a first deceleration stage. The deceleration process is split into two deceleration ramps, with an intermediate cooling stage at about $30\,\mathrm{MeV/u}$. This increases the efficiency by compensating the loss in beam quality [111].
After a few seconds of electron cooling at $30\,\mathrm{MeV/u}$, the deceleration is continued at a reduced ramp rate to the final energy of $4\,\mathrm{MeV/u}$. At this energy, the beam is cooled again before being ejected to the HITRAP facility (see Fig. 3.3). The process from HCI production to beam transport to HITRAP takes $30\,\mathrm{s}$ to $60\,\mathrm{s}$, depending on the starting energy. The number of ions decreases significantly during this process. Starting with 10^7 ions at injection in the ESR, typically results in a few 10^5 decelerated and cooled ions at ejection. The dominant loss mechanism is the electron capture from the residual gas, which is significantly higher at low beam energies [111].
The HITRAP decelerator consists of a linear decelerator and the Cooling Trap, which are described in more detail in Sec. 3.3.1 and 3.3.2, respectively. Ions, which are successfully

[6] Nuclear Instrumentation Module
[7] Multi Branch System
[8] list mode data

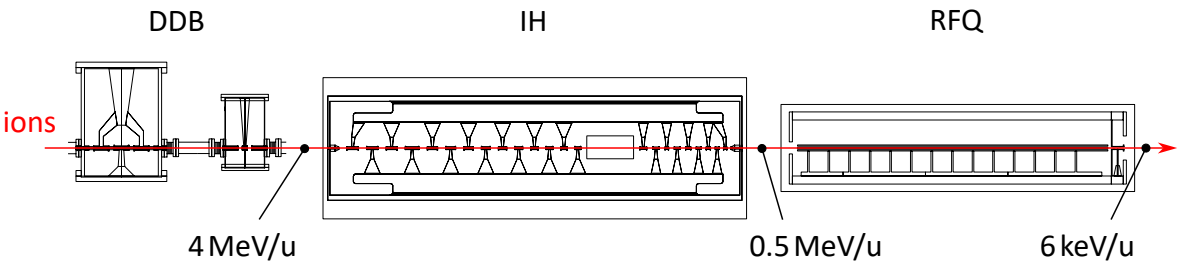

Figure 3.7: Lateral cut of the three main linear decelerator components of HITRAP. The structures are to scale, but beamline components in between, such as steering and focusing elements, are omitted. The Double-Drift Buncher (DDB) bunches the beam for deceleration in the Interdigital H-type (IH) structure. The final deceleration step to $6\,\mathrm{keV/u}$ is realized in the Radio Frequency Quadrupole (RFQ). See text for more information.

decelerated and cooled in the Cooling Trap, are transported with an energy of a few keV/q [9] along a $20\,\mathrm{m}$ long beamline towards the different experiments. The transport energy is chosen as a compromise between transport losses and the requirements of the end users. The residual gas pressure in the beamline is about $10^{-9}\,\mathrm{mbar}$, resulting in charge exchange losses for U^{91+} at $4\,\mathrm{keV}/q$ of $4\,\%$ for a transport over $20\,\mathrm{m}$ [112].
Locally constructed experiments at HITRAP are ARTEMIS [113] and SpecTrap [23]. ARTEMIS aims at the investigation of the electron g-factor in HCI by a double resonance technique with optical light and microwave radiation, while SpecTrap aims at the investigation of the hyperfine splitting of HCI by laser spectroscopy. During the completion of this work, a new experiment on quantum logic spectroscopy [12] is set up at HITRAP by a Helmholtz Young Investigator Group to employ HCI for the development of novel frequency standards. There is also space for mobile setups, for example on surface ionization with slow beams of heavy HCI [114].

3.3.1 Linear Decelerator

The energy limit for ion capture in the Cooling Trap is about $6\,\mathrm{keV/u}$, so the ion energy must be reduced by three orders of magnitude in the linear deceleration part of the HITRAP facility. This system consists of three main components, which are a Double-Drift Buncher (DDB), an Interdigital H-type (IH) structure and an RFQ as shown in Fig. 3.7.
The Double-Drift Buncher is used to bunch the $1\,\mu\mathrm{s}$ long macropulse coming from the ESR, to match the longitudinal acceptance of the subsequent IH. The DDB is composed of two spatially separated bunchers. Each buncher contains an RF cavity and bunches are formed according to the principle of phase focusing introduced in Sec. 2.1.1. The first buncher is driven at a frequency of $108\,\mathrm{MHz}$[10], while the second is operated at the second harmonic of $216\,\mathrm{MHz}$. The

[9] Note that the energy here is given per charge state and not per nucleon. This is more convenient in the case of electrical components such as the beamline or the Cooling Trap. The conversion is easily obtained with the mass-to-charge ratio of the ion.
[10] Same frequency as used in the Alvarez-type cavities of UNILAC.

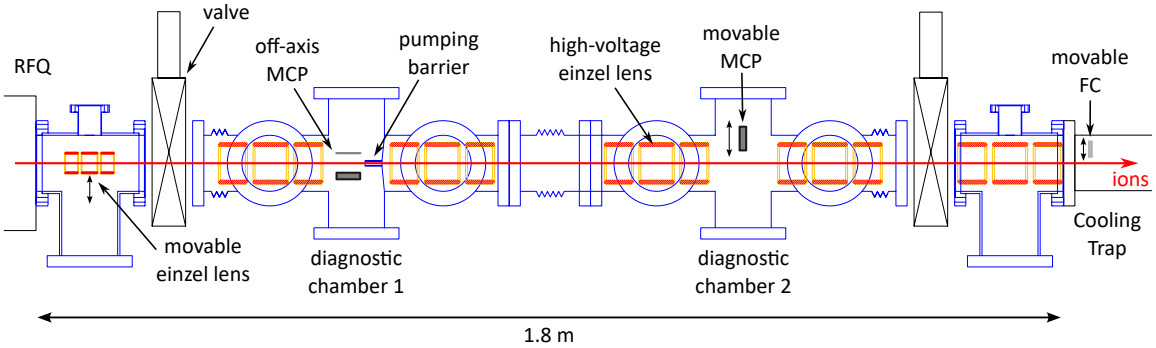

Figure 3.8: Schematic of the low-energy beamline (LEBT) between RFQ and the Cooling Trap. Six high-voltage einzel lenses are needed to focus the strongly divergent beam towards the trap. Different detectors can be installed in the diagnostic chambers. For HCI from the RFQ an off-axis Micro Channel Plate (MCP) with deflection plate is used to distinguish low from high energy ions. For trap commissioning, a movable MCP or Faraday Cup (FC) is suitable to detect ejected particles.

subsequent decelerator systems are also operated at $108\,\mathrm{MHz}$ and must be phase-locked to the buncher system in order to decelerate the ion beam efficiently. The advantage of a double buncher system compared to a single frequency system is the higher bunching efficiency [115]. Following the DDB, a $2.7\,\mathrm{m}$ long IH structure with a peak power of up to $200\,\mathrm{kW}$ is used to decelerate the ion beam from $4\,\mathrm{MeV/u}$ to $0.5\,\mathrm{MeV/u}$. An IH-type LINAC is a special LINAC design in which the magnetic component of the electromagnetic field inside of the cavity is parallel to the beam axis instead of the electric component as in the Alvarez design, which is advantageous for manipulation of low-energy ions ($\beta < 0.5$) [116]. However, the basic principle of accelerating gaps in between drift tubes is the same for both concepts.
Since the IH at HITRAP is used for deceleration, the drift tubes become progressively shorter to account for the change in flight time and the RF phase has to be matched to decrease the beam energy. Inside of the cavity, a quadrupole triplet is integrated to focus the partially decelerated ion beam. With the IH a deceleration efficiency of about $50\,\%$ was achieved, which is close to the theoretical limit of $60\,\%$ [117].
The final linear decelerator element of HITRAP is a $2\,\mathrm{m}$ long RFQ that decelerates ions to about $6\,\mathrm{keV/u}$. A second buncher is installed in front of the RFQ to adjust the phase of the ion beam to increase the efficiency. The RFQ was redesigned in 2012, because the energy acceptance of the first version did not match the output of the IH. The new design corrects this and in 2014 the full deceleration of the HITRAP linear decelerator was achieved for the first time. The RFQ is designed to transmit about $60\,\%$.
As mentioned in Sec. 2.1.1, the deceleration comes with an increase of the geometric emittance and the strongly divergent beam is a big challenge after the linear decelerator of HITRAP. The output of the RFQ shows a large transverse 1σ-emittance of up to $180\,\mathrm{mm\ mrad}$. Transporting this beam to the Cooling Trap over a distance of about $2\,\mathrm{m}$ is challenging. Therefore, a dedicated low-energy beamline (LEBT) with six high-voltage einzel lenses is installed after the RFQ (see

Fig. 3.8). The first einzel lens has a smaller size and is movable to allow for the insertion of an energy-analyzing detector. With typical voltages of $-30\,\mathrm{kV}$[11] it is possible to focus large parts of the ion ensemble towards the trap.
SIMION simulations show a transport efficiency in the LEBT of $60\,\%$, starting from the expected output of the RFQ [118], with respect to ion energy and angle. Assuming a typical ion number of 5×10^5 delivered from the ESR and multiplying the efficiencies of the individual components, results in 1×10^5 decelerated ions at the Cooling Trap. This is an overall efficiency of $20\,\%$.
In addition to transporting the ion beam, the LEBT separates the vacuum systems of the RFQ and the trap. During operation, the residual gas pressure next to the RFQ is in the range of $10^{-7}\,\mathrm{mbar}$, while the pressure next to the trap is about $10^{-9}\,\mathrm{mbar}$. In order to sustain the vacuum of the trap, a small diameter diaphragm is installed to act as a pumping barrier. Therefore, the transport settings must be adjusted accordingly so that the ion beam is focused in the diaphragm to minimize ion loss.
A further challenge is the beam energy composition. A significant part of the incoming ion bunch, which did not fill the phase space bucket of the deceleration system, remains on axis and can pass through the decelerating structures. As a result, in addition to the $6\,\mathrm{keV/u}$ beam, a significant amount of ions with energies close to the injection energy or at intermediate energies are present in the LEBT. To distinguish between the two components, a conventional detector injected into the beam path is not suitable. Therefore, an off-axis MCP in combination with a deflection plate is installed in the diagnostic chamber (see Fig. 3.8). The deflection plate can be biased with a high voltage of up to $10\,\mathrm{kV}$ in order to deflect the low-energy component of the beam onto the detector. The high-energy part is not affected and is not expected to significantly disturb the measurement.
The low-energy ion ensemble has a central energy of $6\,\mathrm{keV/u}$, but a broad energy distribution due to the deceleration. Simulations show a large longitudinal energy spread of about $\pm 1\,\mathrm{keV/u}$ [118]. This complicates the beam transport in addition to the transverse beam quality. Also, capturing the ion beam in the Cooling Trap becomes more challenging.

3.3.2 Cooling Trap

The Cooling Trap of HITRAP is a $40\,\mathrm{cm}$ long Penning-Malmberg trap and consists in total of seven gold-coated trap electrodes (see Fig. 3.9). The outermost electrodes are mainly used to capture extended bunches of HCI, while the adjacent electrodes can be utilized to capture electrons. The central part of the trap consists of two short endcaps and a ring electrode, as common in a basic Penning trap. The ring electrode is split into four segments to be able to address the radial ion motions.
The axial and radial dimensions z_0 and r_0 for the three central electrodes are chosen such that this arrangement facilitates an orthogonalized Penning trap (see also Sec. 2.2.2) and that the voltage of the compensation electrode is the same as that applied to the ring. This means that no separate compensation electrode is required, as it is built into the ring by design [119]. In this part of the trap, charged particles perform in good approximation harmonic oscillations,

[11] Simulations show a higher transport efficiency by using negative einzel lens voltages.

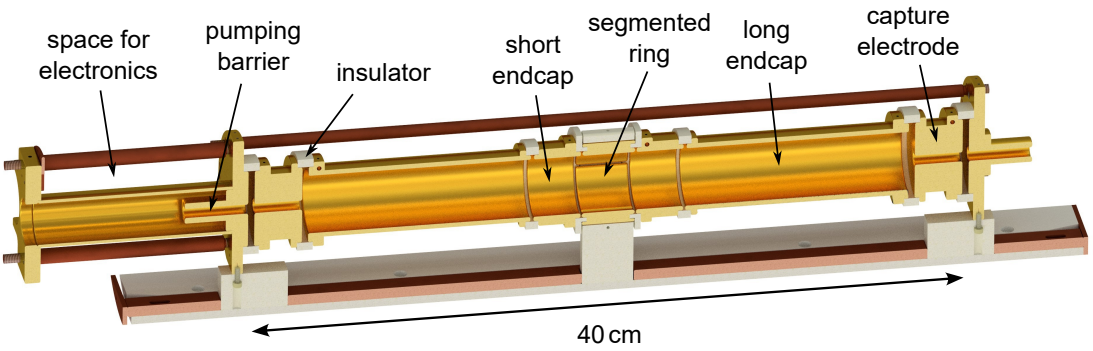

Figure 3.9: Lateral cut of the trap stack of the HITRAP Cooling Trap. The distance between the capture electrodes is $40\,\mathrm{cm}$ to enable trapping of extended bunches of Highly Charged Ions (HCI). The seven electrodes allow the formation of a nested trap potential for electron cooling of the stored ions. The trap is designed by Z. Andelković.

which allows in principle for non-destructive detection methods or resistive cooling.
The design of the Cooling Trap enables the formation of a nested trap potential as shown in Fig. 2.7. This is necessary because electron cooling (see Sec. 2.3.2) is applied to reduce the mean ion energy and, more importantly, to reduce the longitudinal energy spread of the ion ensemble coming from the linear decelerator of HITRAP. In a typical trapping scheme, electrons are captured first between the long endcaps until they have lost a large fraction of their energy by synchrotron radiation. The ions are then captured by the capture electrodes and the cooling process begins by the spatial overlap with the electrons. The next step requires detailed optimization to quickly cool the HCI to the lowest possible energies without losing the high charge state due to recombination processes. Therefore, different trap potentials can be employed and the timing of the ejection must be carefully chosen. The entire process should take less time than the ESR needs to prepare a new ion bunch.
The design of the Cooling Trap was revised and simplified in 2018 [120]. The main problem of the old design [43], which had a total of 21 separate electrodes, was the error-prone cabling system with 52 individual connections to the trap. As a result, broken connections often prevented the operation of the trap and led to long maintenance periods. Therefore, the new design has a minimal number of electrodes with only twelve connections and has demonstrated reliable operation with no major interruptions. Some properties of the Cooling Trap are listed in Tab. 3.4.

The trap is supported by long copper rods and ceramic rings insulate the different electrodes. On one side of the trap stack is some additional space that can be used for electronic components. The trap is mounted on three support structures, which are electrically insulating, but thermally conductive, and is placed in the bore of a superconducting magnet. The magnetic field is arbitrary adjustable up to a field strength of $6\,\mathrm{T}$. The magnet has a cold bore that is

Table 3.4: Properties of the HITRAP Cooling Trap.

Length	$38.7\,\mathrm{cm}$
Trap radius	$20.5\,\mathrm{mm}$
Electrodes	7
Magnetic field	$\leq 6\,\mathrm{T}$
Temperature	$<10\,\mathrm{K}$
Max. platform voltage	$10\,\mathrm{kV}$
Vacuum	$< 10^{-12}\,\mathrm{mbar}$

thermally connected to the trap and thus the trap is at cryogenic temperatures during operation. This is advantageous for the residual gas pressure in the trap, because gas particles are effectively removed by being adsorbed by the cold surface [121]. This effect, combined with the small diameter at the endpoints of the trap and the low pressure in the adjacent beamline sections, results in residual gas pressures below $10^{-12}\,\mathrm{mbar}$ in the trap. Such pressures are mandatory for the storage of HCI to avoid recombination losses and to increase the storage time (see Sec. 4.2.1).

The geometrical-extended trap design allows the storage of HCI bunches with broad energy and thus long spatial distribution. Assuming a maximum energy of $7\,\mathrm{keV/u}$ for Bi^{82+} ions, results in a velocity of about $1.2\,\mathrm{m/\mu s}$ and the ions travel twice the trap length in $700\,\mathrm{ns}$, neglecting radial motions. Therefore, a bunch length of about $700\,\mathrm{ns}$ can be trapped without losing the fastest ions.

One way to capture longer bunches is to reduce the velocity of the ions as they enter the trap region. To do this, the Cooling Trap is connected to a high-voltage platform that can be biased to a voltage of $+10\,\mathrm{kV}$ against ground. For the previous example, the maximum bunch length that can be trapped in this case is increased to $1\,\mu\mathrm{s}$. During storage, the platform voltage can be arbitrary adjusted, which determines the offset energy of ejected ions. A mean energy around $4\,\mathrm{keV}/q$ for the released ions is reasonable, since the subsequent beamline is designed for this energy range.

To capture HCI, the entrance capture electrode must be switched rapidly, after the ion bunch reaches the trap. The second capture electrode is used as an electrostatic mirror at a constant positive potential during the process. Attached to each capture electrode is a HV-switch[12], which can be triggered to switch between two input voltages. A typical capture voltage of $20\,\mathrm{kV}$ is applied with a rise time of less than $100\,\mathrm{ns}$. The precise timing is controlled by an FPGA[13] with a timing resolution of $5\,\mathrm{ns}$. Besides the ion capture, the FPGA controls all time-sensitive events in a temporal sequence, such as ion ejection and detection, adjustment of trap potentials, electron production or beam transport.

[12] HTS 301-10-GSM, BEHLKE
[13] PCI-7811R, NI

Detection of Stored Particles

Currently, the detection of stored particles is only possible by ejecting them on destructive detectors outside of the magnetic field. For this work, a Micro Channel Plate (MCP) is used in the diagnostic chamber of the LEBT close to the trap (see Fig. 3.8). An MCP consists of many small channels with a diameter between $10\,\mu\mathrm{m}$ and $100\,\mu\mathrm{m}$ and a length-to-diameter ratio between 40 and 100 [122]. Both ends of the channels are covered with a metallic coating, in order to apply a high voltage across these channels.
If an ionizing particle impacts a channel on the surface of the MCP, electrons are produced and accelerated. This creates an electron avalanche that can be measured electronically. The signal from the MCP used for the Cooling Trap is measured from the capacitive fluctuation of the supply voltage and is proportional to the number of primary particles. However, this method provides only relative results and is not suitable for measuring an absolute particle number.
A second detector, primarily used during beam adjustment, is a conductive metal plate - commonly called a Faraday Cup (FC) - located close to the trap in the fringe field of the superconducting magnet (see Fig. 3.8 and Fig. 3.10). The FC is electrically connected to an amplifier and impinging charges can be measured directly as a voltage signal. Since the signal is directly proportional to the deposited charge of the particles, this constitutes an absolute measurement.
It must be noted that electrons from the surface can be released by the incident particles, which is measured as an additional positive charge. This effect is typically in the range of $20\,\%$ and can be suppressed in other setups by applying a negative voltage on a cage surrounding the cup. The FC is not suitable for the detection of stored particles, because the electrical noise generated by the rapid switching of the trap electrode voltage exceeds the signal. However, it is used, e.g. for adjusting the electron beam into and through the Cooling Trap as described in Sec. 4.2.2.

Electron Source

The electron source for the Cooling Trap is shown in Fig. 3.10 and was developed and commissioned by C. Krantz. Detailed information can be found in [123]. The source is designed to deliver short ($1\,\mu\mathrm{s}$) bunches with up to 5×10^9 electrons. The bunch structure is important to store a maximum number of electrons in one capture process as described in Sec. 4.2.2. The electron bunch is generated by an ultraviolet-light pulse of a xenon flash lamp[14] that is coupled in the beamline through a small window (see Fig. 3.10). The pulse is focused on the gallium-arsenide (GaAs) photocathode of the electron source and electrons are emitted via photon absorption. By applying a typical negative voltage of $-200\,\mathrm{V}$, the electrons are accelerated away from the cathode.
The electron source is mounted in a diagnostic chamber about $1.5\,\mathrm{m}$ downstream of the Cooling Trap. It is placed off axis to not interfere with the ion flight path. To direct the electrons towards the trap, several pairs of magnetic coils are placed around the beamline. These are ramped synchronously with the light flash to guide the electrons without disturbing the flight

[14] L11316-11, Hamamatsu

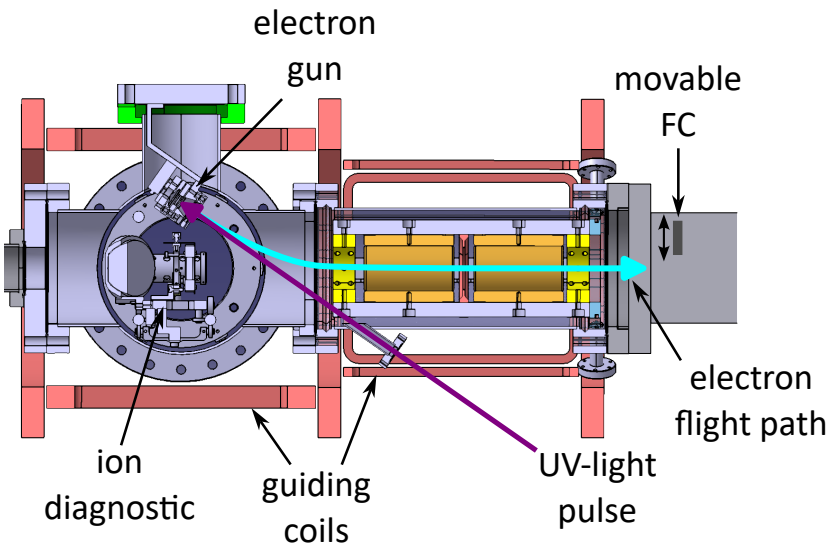

Figure 3.10: Electron source for the HITRAP Cooling Trap. Electrons are generated by an ultraviolet(UV)-light pulse and guided by magnetic coils towards the trap. The electron gun is placed off-axis in order to allow the passage of the ion beam. The electrons can be detected in front of the trap by an FC. The image is modified from [123] and used with the permission of C. Krantz.

path of the ions and to prevent overheating. The electron bunch can be detected directly in front of the trap by an FC, which is already placed in the magnetic field of the trap.

4 Commissioning of the HITRAP Cooling Trap

4.1 Status of the HITRAP Project

The funding for the HITRAP project at GSI began in 2005 and the first components were commissioned during a beamtime in 2007. In the following years, the commissioning of the linear decelerator components progressed steadily in two or three beamtimes per year. After the redesign of the RFQ in 2012, the functionality of the new design was proven in 2014 and HCI bunches were successfully decelerated from $4\,\mathrm{MeV/u}$ to $6\,\mathrm{keV/u}$ [117].
With the start of the CRYRING@ESR project [90] at GSI in 2015, most of the manpower from HITRAP was reassigned to the new experiment. Since then, there has been no further beamtime at HITRAP and only limited efforts have been invested in commissioning the Cooling Trap with offline ions to demonstrate electron cooling, but (so far) without success. During these tests, it has been decided to redesign the trap, in order to achieve a more reliable operation. The new design was implemented in 2018 and first tests were performed [120].
This is the starting point of this work at the HITRAP Cooling Trap setup. The new trap design has to be commissioned with ions from the EBIT and with electrons from the local electron source, which is a major contribution of this work. Some of these results are presented in Sec. 4.2.1 and 4.2.2. Furthermore, during this work, ions and electrons were simultaneously stored in the Cooling Trap for the first time and signs of electron cooling were observed. These experiments are discussed in Sec. 4.3.
In 2022, after a break of eight years, a beamtime with HCI from the ESR took place. During this campaign, the achievements of the previous beamtime were repeated, although the linear decelerator was not operated for a long time. In addition, an updated control system was implemented and successfully tested.
In the next beamtime period in 2024, HITRAP is assigned with two beamtimes to demonstrate the transport of HCI from the RFQ to the Cooling Trap and electron cooling of heavy HCI in the trap. With the recent progress, accelerator produced HCI could soon be transported from HITRAP to the subsequent high-precision experiments.

4.2 Status of the Cooling Trap

4.2.1 Commissioning with HCI

The commissioning of the Cooling Trap includes several stages, such as the implementation and testing of the hardware and software. The results presented here, which are also published in [124], demonstrate the successful storage of HCI from the local source and allow the extraction of the ion lifetime in the trap.
For the offline experiments, the SPARC-EBIT (see Sec. 3.1.1) is used and connected to a reservoir of argon gas to produce highly charged $^{40}Ar^{16+}$, which has a mass-to-charge ratio of 2.5, close to H-like bismuth. Using a breeding time of $1.3\,\mathrm{s}$ and a transport energy of $4\,\mathrm{keV}/q$, results in bunches of a few 10^5 Ar^{16+}-ions at the Cooling Trap. A magnetic bender is installed in the transport beamline between EBIT and trap to allow for charge-state separation.
To capture the ions, coming from the right side of the trap, the left capture electrode is at a blocking potential of $6\,\mathrm{kV}$, while all other trap electrodes are at ground potential. The ion energy is not sufficient to surpass the potential of the left capture electrode and the bunch is reflected. Before the bunch leaves the trap again, the right capture electrode is also switched to $6\,\mathrm{kV}$ and the ions are trapped. After a certain storage time, the left blocking potential is reduced and the ions leave the Cooling Trap towards the LEBT (see Fig. 3.8), where they can be detected by an MCP detector.
The lifetime of the trapped ions can be estimated by varying the storage time and analyzing the ejected ions. The detected signal decreases with increasing storage time as shown in Fig. 4.1 due to two main effects. First, elastic scattering of the trapped ions with residual gas particles or other ions. This results in a momentum change that can lead to scattering into an unstable orbit and ion loss. This mechanism is enhanced for large ion numbers and for high residual gas pressures.
The second effect is charge exchange. Thereby, one or more electrons from the residual gas are captured into a bound state of the ion, reducing the ion charge state. The absolute energy is not changed in the process, but the energy per charge state increases. For charge exchange processes, the ion loss must be specified more precisely. Direct ion loss occurs, if the energy per charge is higher than the axially confining electric potential. However, an ion can remain trapped after charge exchange, if the energy per charge stays low enough to allow for axial confinement. In this case, the number of ions in the initial charge state is reduced while the ion number of the lower charge state is increased, which can be referred to as charge-state loss and growth, respectively.
For the commissioning with a confinement potential of $6\,\mathrm{kV}$ and an ion energy of $4\,\mathrm{keV}/q$, a direct ion loss occurs when the Ar^{16+}-ions undergo six charge exchanges, resulting in Ar^{10+} with $6.4\,\mathrm{keV}/q$. The detector used is in first order insensitive to the charge state of ejected ions. To resolve different charge states, the left capture electrode is not switched to ground potential, but to an intermediate potential. For example, a capture electrode potential of $4.1\,\mathrm{kV}$ keeps Ar^{16+}-ions trapped, while lower charge states leave the trap and are detected.
According to this scheme, the data of Fig. 4.1 is recorded. While the signal for the ejection

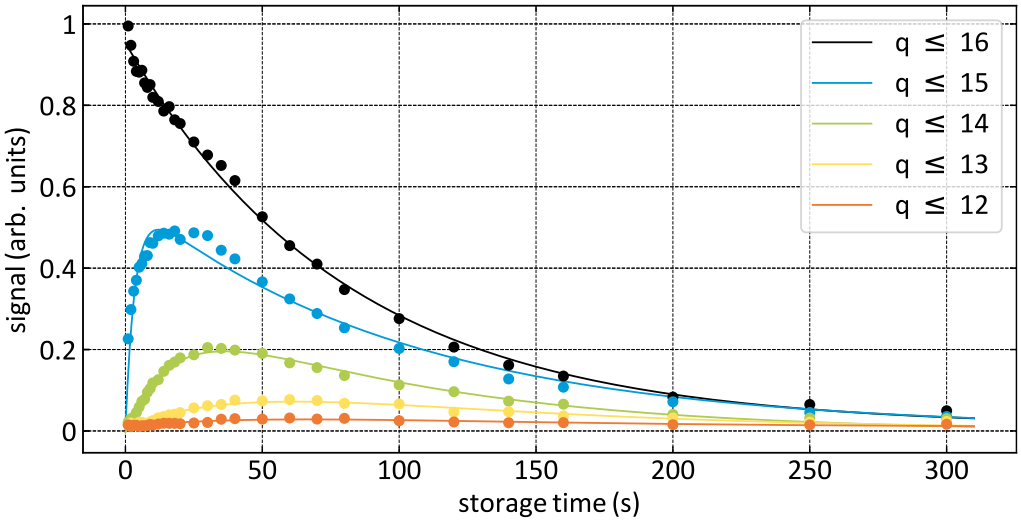

Figure 4.1: Normalized signal of ejected Ar^{q+}-ions measured with a Micro Channel Plate (MCP) after different storage times. The initially pure sample of Ar^{16+}-ions undergoes charge exchange with the residual gas and populates lower charge states. The black data contains all stored charge states, the blue data only charge states with $q \leq 15$ and so on.

of all ions shows an initial maximum followed by an exponential decay, the signal without Ar^{16+} ($q \leq 15$) is negligibly small at first, then grows to a maximum before also decaying exponentially. The shape for lower charge states is similar and the maximum shifts to later times, which is expected, if single charge exchange dominates over double charge exchange. The signal of charge state $12+$ and lower ($q \leq 12$) is already very small and the last one measured.
The total ion loss observed in the measurement period of $300\,\mathrm{s}$ does not seem to be dominated by charge exchange to Ar^{10+}, since there is almost no population left in $q \leq 12$. More likely, elastic scattering with residual gas is the limiting factor for the lifetime. This ion loss mechanism could be enhanced as the charge state decreases, because the axial particle confinement becomes weaker.
For most subsequent experiments at HITRAP, charge-state loss is equivalent to ion loss. To investigate the lifetime of Ar^{16+}-ions, the population of $q \leq 15$ is subtracted from the total signal, which is shown in Fig. 4.2. The total signal is fitted with an exponential decay, while the data for the charge states $q \leq 15$ is fitted by a combination of an exponential increase and decrease to account for the growth due to charge exchange of Ar^{16+}. The division of the two fits yields the green data points. The shape of the curve indicates that two phases must be separated. Within the first ten seconds, the number of Ar^{16+}-ions decreases at a high rate, which is mainly caused by charge exchange, as the population of the lower charge states also increases rapidly. After that, the rate becomes significantly lower, which is not fully understood yet. Perhaps the total number of ions or the number of ions per charge state influence the loss

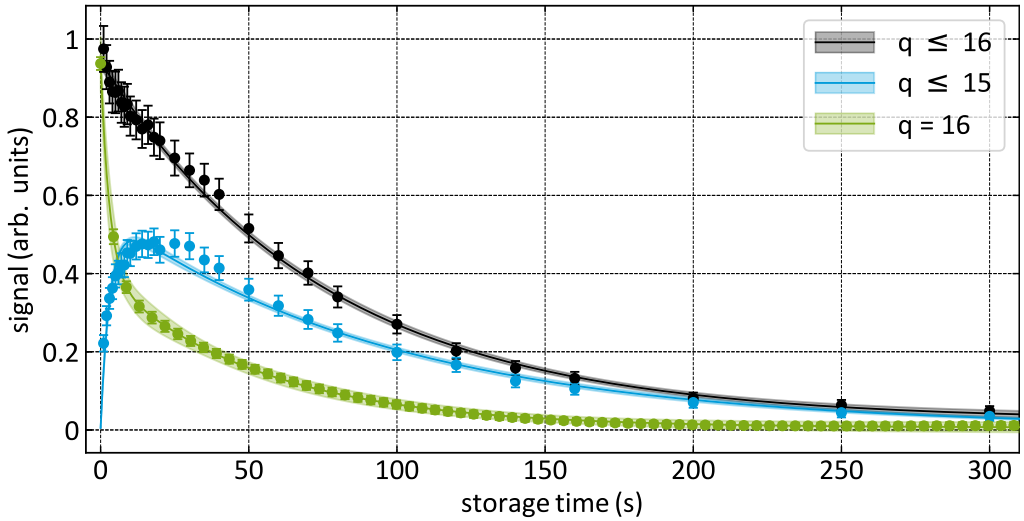

Figure 4.2: Fitted signal of ejected Ar^{q+}-ions for different storage times (see also Fig. 4.1). Subtracting both fits results in the evolution of the charge state population of $q = 16$.

rate. Further measurements are being prepared as this thesis is being written, to employ a magnetic charge selection and an energy-sensitive detector to investigate the process in more detail [125].
Fitting a double exponential decay to the obtained signal of Ar^{16+}, leads to lifetimes of

$$\tau_1 = (3.0 \pm 1.2)\,\mathrm{s} \quad \text{and} \quad \tau_2 = (53.0 \pm 12.9)\,\mathrm{s}. \tag{4.1}$$

Since simulations [37, 43] predict a cooling time of single seconds, electron cooling is possible in both phases, but especially in phase two. Therefore, the successful offline tests with HCI demonstrate sufficient storage times in the trap. The next step is to demonstrate this also with heavy HCI from the accelerator chain.

4.2.2 Commissioning with Electrons

Compared to the initial commissioning in 2009 [123], two hardware changes are implemented to increase the output of the local electron source. The xenon flash lamp is upgraded to a high-intensity model and the UV fiber is replaced with a new one that is half the length. Both changes increase the amount of photons, which are focused on the GaAs photocathode and are available for the photoelectric effect. After optimization of the light pulse and the electron transport settings, the signal shown in Fig. 4.3 is obtained on the FC in front of the trap.
The signal is about $1\,\mu\mathrm{s}$ long and the enclosed area can be converted to the number of electrons using the gain factor of the amplifier. This gives a total of more than 5×10^9 electrons per bunch, which is a factor of two higher than before the improvements.

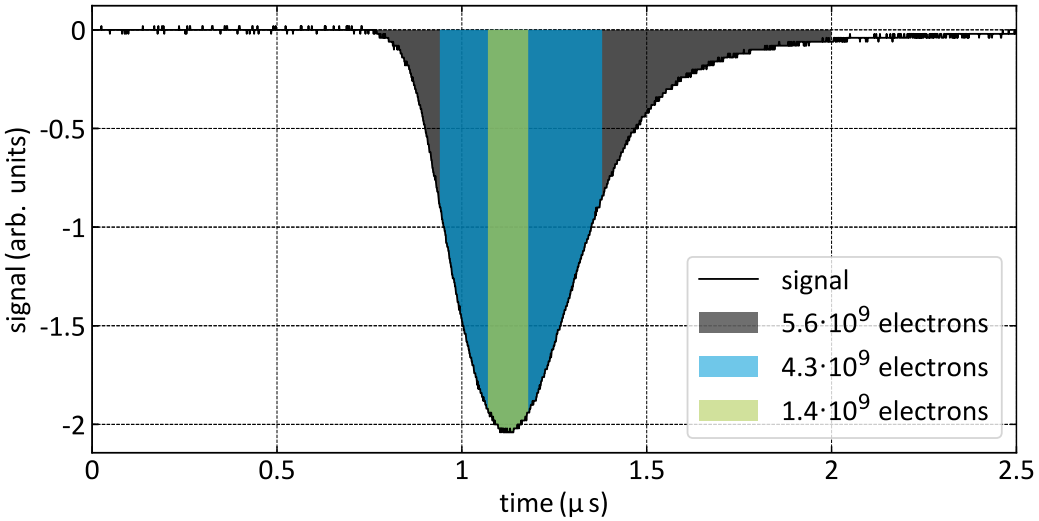

Figure 4.3: Detected electron signal with a Faraday Cup (FC) in front of the Cooling Trap. Due to the geometrical length of the trap, it is not possible to capture the entire $1\,\mu s$ long bunch. The blue and green areas represent electrons that could theoretically be trapped between the capture electrodes and long endcaps, respectively.

Due to the limited geometric length of the Cooling Trap, not all of these electrons can be captured. Estimation of the electron flight time in the strong magnetic field by measuring the electrons with the FC in front and after the trap yields a theoretical maximum of 4.3×10^9 electrons for capture between the capture electrodes and 1.4×10^9 electrons for capture between the long endcaps (compare with Fig. 3.9). The latter case is the most important, since this part is used for the nested trap potential. Unfortunately, the absolute number of electrons stored cannot be measured directly, because the electron ejection out of the magnetic field leads to a significant loss and the absolute measurement with the FC is disturbed by electrical noise caused by the fast switching electrode.
To get an estimate of the number of stored electrons, which is a crucial factor for the electron cooling process, another measurement principle is needed. One option is to determine the space-charge potential, which is proportional to the number of stored electrons. The electrons in the trap can be approximated as a homogeneous cylindrical beam reflected from the endcap electrodes. The resulting space-charge potential can be assumed analogous to the electron beam in an electron cooler.
In the derivation of Eq. 2.29 in [40], the charge density ρ_e for the relativistic electron beam is expressed in terms of current I_e and velocity β_e. For the electrons in a trap, the charge density can be calculated from the total electron number N_e and the cylindrical trapping volume V_t

$$\rho_e = e n_e = \frac{e N_e}{V_t} = \frac{e N_e}{\pi R_e^2 l_e}. \tag{4.2}$$

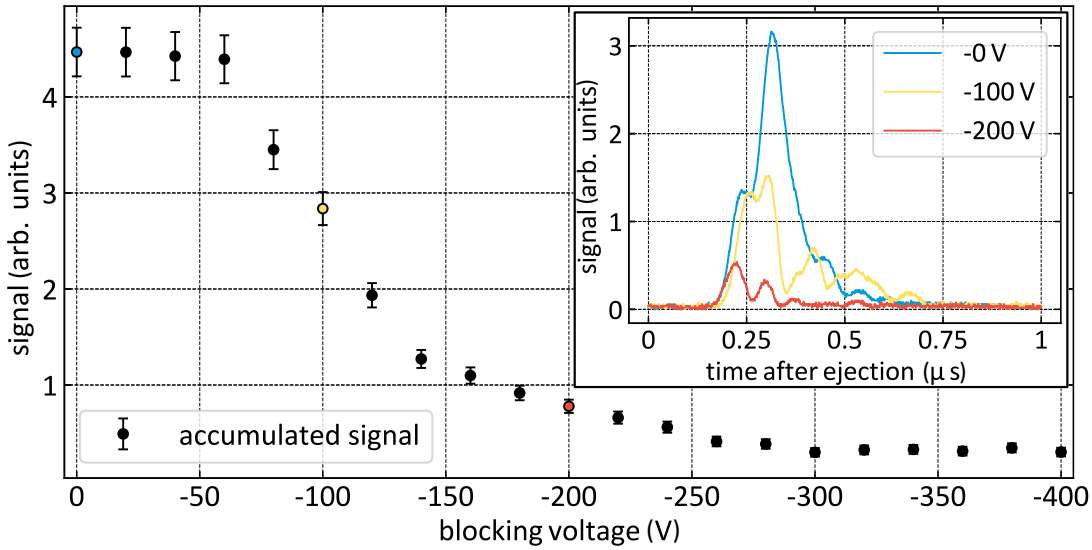

Figure 4.4: Accumulated signal of ejected electrons for different blocking voltages. The highest electron energy is about $200\,\mathrm{eV}$. The inset shows the raw signal for a blocking voltage of $0\,\mathrm{V}$, $-100\,\mathrm{V}$ and $-200\,\mathrm{V}$. The electrons arriving first have the highest energy and are still detectable at a blocking voltage of $-200\,\mathrm{V}$.

Here R_e is the radius of the electron ensemble and l_e is the axial length, which is $0.1\,\mathrm{m}$ between the long endcaps. Substituting the charge density into the space-charge potential yields

$$U_\mathrm{SC}(r) = \frac{N_\mathrm{e} e}{4\pi\epsilon_0 l_\mathrm{e}} \left[1 + 2\ln\frac{R_\mathrm{t}}{R_\mathrm{e}} - \frac{r^2}{R_\mathrm{e}^2}\right] \tag{4.3}$$

with the Cooling Trap radius of $R_\mathrm{t} = 20.5\,\mathrm{mm}$.
The space charge is measured by the retarding field method and the resulting blocking potential curve is shown in Fig. 4.4. The electron bunch is captured and stored for $1\,\mathrm{s}$ between the long endcaps in a $4\,\mathrm{T}$ magnetic field. According to Eq. 2.31, the initial electron energy of $200\,\mathrm{eV}$ is reduced to $0.4\,\mathrm{eV}$ by synchrotron radiation during this time. The kinetic energy of the released electrons can thus be neglected and the measured energy originates only from the space-charge potential.
The ejected electrons are measured on an MCP detector and the signal is accumulated for different blocking voltage potentials. The blocking potential is applied to the left capture electrode. This electrode has no influence on the storage and is located in the homogeneous part of the magnetic field, which guarantees the measurement of the axial energy. The blocking potential curve in Fig. 4.4 shows a plateau for small retarding fields followed by an exponential decrease. At a blocking potential of $-200\,\mathrm{V}$, which corresponds to an electron energy of $200\,\mathrm{eV}$, electrons can still be detected.
The raw signal for a blocking voltage of $0\,\mathrm{V}$, $-100\,\mathrm{V}$ and $-200\,\mathrm{V}$ is shown in the inset of Fig. 4.4. For no retarding field, the signal shows a broad distribution at a flight time of $0.32\,\mu\mathrm{s}$.

As the blocking potential is increased, the signal becomes weaker, but early arriving electrons are blocked last. For $-200\,\mathrm{V}$ the maximum is at $0.22\,\mu\mathrm{s}$. This shows that the ejected electron ensemble consists of different velocity classes and that the fastest electrons arrive at the detector first, as expected for the conversion of potential space charge energy into kinetic energy.
The electron radius R_e in the trap is not known exactly, but is assumed to be between $10\,\mu\mathrm{m}$ and $100\,\mu\mathrm{m}$, which is accounted for in the uncertainty. Using a space charge potential of $U_\mathrm{SC}(0) = 200\,\mathrm{V}$ and Eq. 4.3 results in

$$N_\mathrm{e} = 1.0(2) \times 10^9. \tag{4.4}$$

This is about $70\,\%$ of the geometrical maximum, which is plausible. According to [43], this is a sufficient amount for electron cooling of HCI.

4.3 Simultaneous Storage of Ions and Electrons in the Cooling Trap

After the successful commissioning of the Cooling Trap with HCI and electrons, the next step is to demonstrate electron cooling, which has never been done before for a large cloud of HCI in a trap. To store ions and electrons simultaneously, a nested potential is used as shown in Fig. 2.7. Ions are stored between the capture electrodes and electrons are stored between the long endcaps of the Cooling Trap.
In a first experiment, electrons are stored for $1\,\mathrm{s}$ before the HCI are captured to let them cool in the magnetic field. After this period, a bunch of Ar^{16+}-ions from the SPARC-EBIT with an energy of $4\,\mathrm{keV/u}$ is simultaneously stored in the Cooling Trap. For different storage times the ions are ejected first, before the electrons are ejected with a delay of $0.4\,\mathrm{s}$. Both signals are recorded by an MCP. To analyze the interaction of ions and electrons, the same process is repeated with identical settings, but without the injection of ions. The comparison of the electron signal for different storage times with and without ions is shown in Fig. 4.5.
For a storage time of $1\,\mathrm{s}$ no effect of stored ions on the electron signal is observed. However, as the storage time increases, a significant difference can be detected. The electron signal is higher, if there are also ions trapped, indicating an interaction between the two ensembles. One explanation for this effect is the improved ejection of the electrons due to the positive charge of the ions, which changes the radial position of the electrons in the trap.
The same measurement principle is also repeated with and without electrons while observing the ion signal, but no difference is observed. Although these measurements do not directly lead to an observation of energy loss of the ions, it reveals the necessary ion-electron interaction. A likely reason for the lack of any cooling effect on the ions is an insufficient radial overlap with the electrons. To improve this, a fluorescence detector is designed and implemented to replace the FC in the LEBT close to the trap.
With this detector the Cooling Trap can be aligned with the magnetic field and the electron injection can be optimized. This and further progress with the Cooling Trap will be described in detail in the PhD thesis of S. Rausch [125]. As a result of the optimization process, a similar measurement as described above leads to the signals shown in Fig. 4.6.
The red curve shows the ejected signal of highly charged argon without simultaneously stored

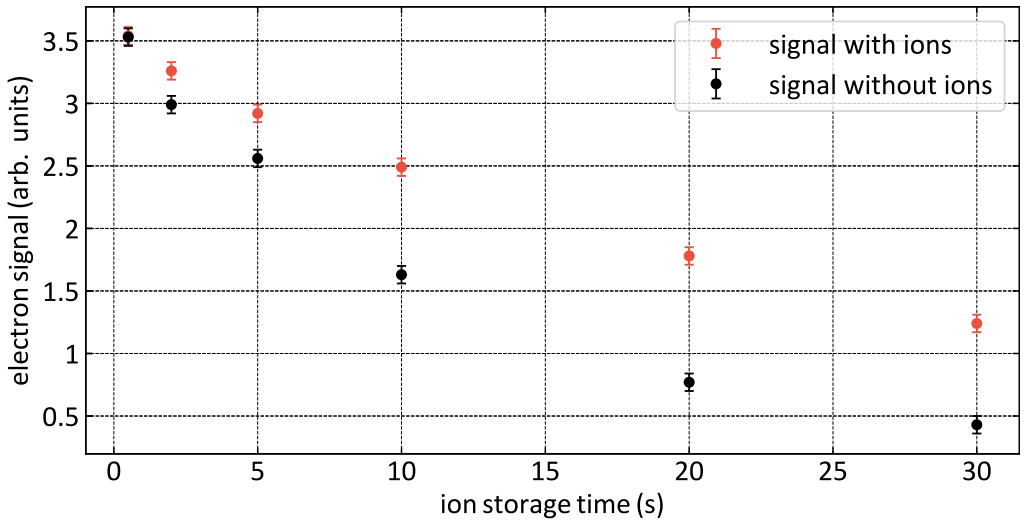

Figure 4.5: Ejected electron signal for different storage times with and without simultaneously stored ions. An increasing effect of the ions on the electrons is observed as the storage time increases. This demonstrates the interaction of ions and electrons in the Cooling Trap.

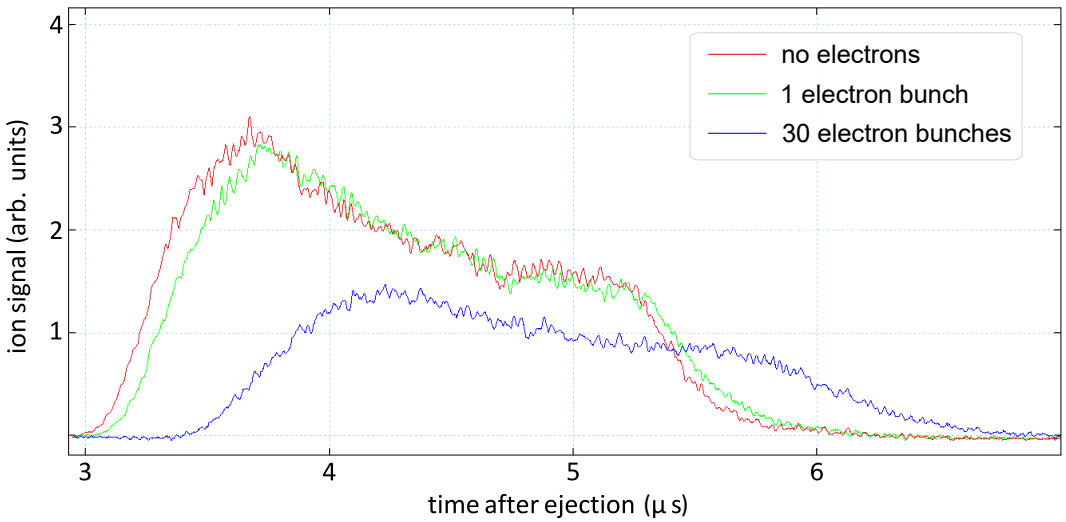

Figure 4.6: Signal of ejected highly charged argon ions after a storage time of $2\,\mathrm{s}$ with different amounts of simultaneously stored electrons. The increase of the ion flight time is a clear indication for a decrease of the mean ion energy, which is an electron cooling effect. The data is provided by S. Rausch.

electrons after a storage time of $2\,\mathrm{s}$. The green and blue curves are observed when electrons are present in the trap during this time. As can be clearly seen, the electrons interact with the ions resulting in later arrival times at the MCP. Longer ion flight times translate to lower ion velocity, which is a clear indication of a reduction of the mean ion energy. The effect is small for the capture of a single electron bunch (green), but increasing the number of electrons by accumulating 30 bunches (blue) leads to a significant effect. As these data are produced in the late stages of this work, further analysis is not performed here and the reader is referred to [125].

In summary, the progress made during this work led to the first demonstration of simultaneous storage of ions and electrons in the redesigned Cooling Trap, which has never been achieved with the initial design. Further optimization resulted in the observation of electron cooling effects in the trap. This is currently under further investigation and shows that the offline commissioning of the Cooling Trap is nearing completion.

5 Laser Spectroscopy of $^{208}Bi^{82+}$ at the ESR

5.1 Introduction

This chapter is about the E128 laser spectroscopy experiment on H-like Bi^{82+}. The main objective of the beamtime was to measure the ground-state hyperfine splitting energy of the $1s$ electron of the radioactive isotope $^{208}Bi^{82+}$, which was fully achieved. This is the first time that an artificially produced radioactive isotope has been successfully targeted by laser spectroscopy in a storage ring. The key to this success is the separation of the fluorescence signal of the few exotic ions from the background by using advanced detection and evaluation techniques.
The experiment was performed at the storage ring ESR at the GSI Helmholtzzentrum für Schwerionenforschung in Darmstadt and took place from 09.05. - 17.05.2022 and from 29.05. - 01.06.2022. Due to severe technical problems at the ESR, a large fraction of the first beamtime period had to be canceled. This has been compensated on short notice in the three-day long extension.
Based on the progress made in the first period, the extra three days allowed the measurements of the hyperfine splitting energy of $^{209}Bi^{82+}$ and $^{208}Bi^{82+}$. All laser spectroscopic data presented in this work are from this period. In total 40 individual measurements of the hyperfine splitting of each isotope are obtained. The first 14 measurements were performed with ^{209}Bi, which were followed by all 40 ^{208}Bi measurements. Measurements #15 to #40 for ^{209}Bi were conducted at the end of the beamtime.
The measurements on $^{209}Bi^{82+}$ are performed to test the functionality of the experimental setup in combination with the data acquisition. In addition, the results of previous beamtimes [8, 126] should be confirmed and the larger number of ions of the stable isotope facilitates the study of systematic effects.
A detailed description of the experimental setup can be found in the previous chapter (Sec. 3.2). This chapter begins with a description of the measurement preparation, including the timing between ion bunch and laser pulse. After this, the main focus is on the data analysis and the emerging results. The last part contains the analysis of systematic effects and the concluding discussion.

5.2 Measurement Preparation

Before the laser scan of a measurement run can be started, some requirements must be met and a number of settings have to be specified. One requirement is the spatial overlap of laser and ion beam. Both beam positions can be measured at the electron cooler with the integrated

T-scrapers (see Sec. 3.2.1). Since the ion beam is set up by the machine experts at the beginning of the beamtime and the trajectory cannot be easily adjusted, the ion position remains fixed and is used as a reference. The laser position and angle, on the other hand, can be easily adjusted remotely with the stabilization system (Sec. 3.2.3). After determining the position of the ion beam by scraping the stored beam until it disappears, the laser position is adjusted accordingly. The scraping effect on the laser beam can be observed on a camera-monitored screen, which is used as a beam dump after the ESR. Once the laser position is optimized, the beam stabilization system is activated. This procedure is repeated several times throughout the experiment to account for drifts in the beam position.
The next step is to specify the measurement conditions. This includes the laser scan settings. The scan range and the step size are chosen such that the resonance is completely captured with a reasonable number of data points. In addition, the dwell time per laser step and the number of laser scans are selected to ensure that a sufficient ion current is still maintained at the end of a measurement run. Furthermore, the ESR conditions are set regarding electron cooler current and beam mode. The cooler current is set rather low between $50\,\mathrm{mA}$ to $200\,\mathrm{mA}$ to ensure sufficient cooling, while limiting ion losses due to recombination effects with the free electrons. Varying the cooler current with otherwise identical settings enables the determination of the electron space charge potential (see Sec. 5.6.3).
Resonances are recorded either in coasting or bunched-beam operation. Both of these settings were used about equally often. Using a bunched beam increases the number of ions interacting with the laser, while in the coasting mode the ion energy is not affected by the bunching force. The consequences are discussed in more detail later in this chapter.
Another important requirement, especially for the bunched mode, is the temporal overlap of ion and laser beam. In this experiment a $10\,\mathrm{ns}$ laser pulse with $30\,\mathrm{Hz}$ repetition rate has to be synchronized with a $50\,\mathrm{ns}$ long ion bunch, circulating at $2\,\mathrm{MHz}$ repetition rate. To accomplish the correct timing, a fast photodiode is placed at the entrance and exit windows of the laser-ion overlap section (see Fig. 3.3). This enables accurate monitoring of the transmission of the laser pulse. Both photodiode signals are fed into the time-sensitive TDC channels of the DAQ in the same way as the PMT signals. Great care has to be taken with the signal paths in order to observe the correct timing, since $10\,\mathrm{m}$ difference in cable length already produces a time difference of $30\,\mathrm{ns}$. Therefore, prior to the beamtime all time-sensitive signal paths were checked and delays were adjusted accordingly.
Similar to the phase stability between signal and ion bunch for the DAQ system (see Sec. 3.2.5), the phase stability of the ion bunch with respect to the laser pulse is ensured by using the bunching frequency. Therefore, a coincidence scheme is established with the Q-switch trigger of the laser. With this setup, the temporal overlap can be adjusted by fine-tuning the Q-switch trigger, while monitoring the signals from the photodiodes and the ion-induced fluorescence of residual gas[1]. This is exemplified in Fig. 5.1 using the data of ^{209}Bi measurement #18.
The TDC data from multiple ion revolutions and laser pulses of PMT mid and the photodiodes at the laser ports of the ESR are summed up and displayed for one revolution cycle. The yellow and blue signals are recorded by the photodiodes and the center marks the time when the laser

[1] It is assumed that the main contribution is due to the Ly-α transition of H ($\lambda = 121.6\,\mathrm{nm}$, $\tau = 2.1\,\mathrm{ns}$ [127])

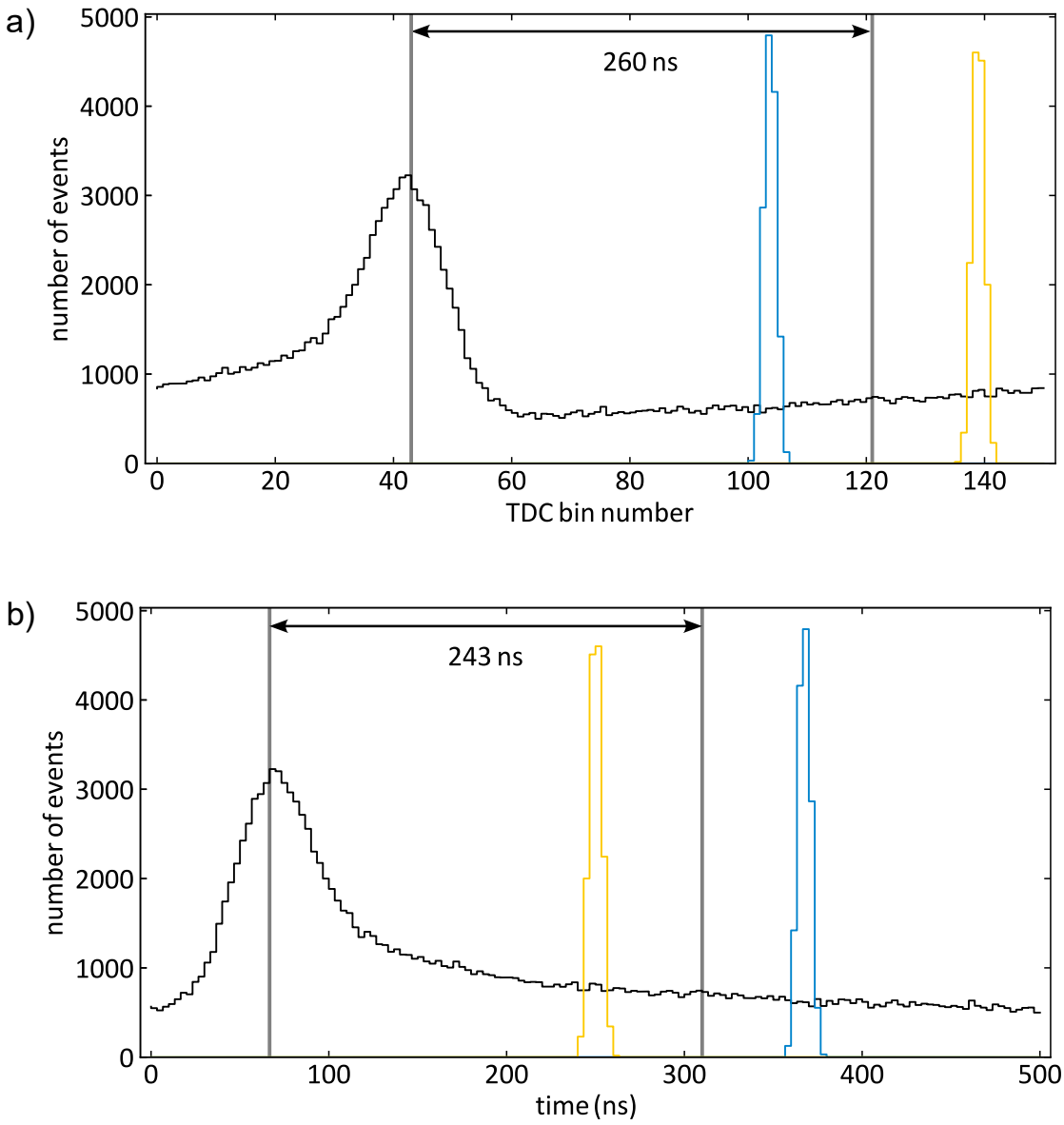

Figure 5.1: Timing scheme of ion bunch and laser pulse for ^{209}Bi measurement #18. The black data is the ion induced fluorescence of the residual gas measured by PMT mid, whereas the yellow and blue data are the signals of the photodiode before and after the ESR electron cooler section. In a) the raw Time-to-Digital-Converter (TDC) data is shown, providing an inverted time axis, while in b) the same data is depicted with transformed x-axis for a more intuitive representation. Due to the spatial separation of fluorescence detection and laser-ion overlap, a time delay of 73 bins or $243\,\mathrm{ns}$ has to be used for the correct timing.

pulse is in the electron cooler. The black signal depicts the ion-induced background detected by the middle PMT. The x-axis is the time required for one revolution, its origin is arbitrary and can be shifted by an additional delay. It should be noted that the TDCs operational principle provides the time to the next common stop. The earlier an event occurs, the larger becomes the timer count. Thus, earlier events are located more to the right and the time axis is actually running from right to left, as can be seen in Fig. 5.1a.
To convert the x-axis from TDC bins to real time, the x-axis has to be inverted and each bin has to be multiplied by $10/3\,\mathrm{ns}$, which yields a time period of $503\,\mathrm{ns}$ corresponding to the revolution frequency of about $2\,\mathrm{MHz}$. In addition, the origin can be shifted, such that the ion signal arrives at the beginning of the time axis, as shown in Fig. 5.1b. This representation method is more intuitive and thus used in the remainder of this work.
The gas-jet target is located exactly opposite to the center of the electron cooler. The optical detection region is about $2\,\mathrm{m}$ downstream of the target (compare Fig. 3.3), which corresponds to about $10\,\mathrm{ns}$ flight time or 3 TDC bins. Therefore, the arrival of the laser pulse is adjusted to be 73 bins ($243\,\mathrm{ns}$) after the ions pass the detection region, which is 3 bins shorter than the time period of a half revolution.
During the beamtime this procedure is applied several times. The position of the ion bunch is always determined by the highest signal of the residual-gas fluorescence. Note that this signal has a slight time delay compared to the ion bunch, due to the lifetime of the excited residual gas states. This is further discussed in Sec. 5.3.1 and has not been considered during the beamtime. This effectively shifts the laser-ion overlap slightly away from the center of the electron cooler to later times. This effect is small and competes with the uncertainties of the measured signal paths. The data analysis also shows, that the signal from PMT north arrives a few bins earlier than the reference signal from PMT mid. This is not a problem as long as a complete overlap of ions and laser pulse is achieved. Therefore, different time delays have been tested while the laser was tuned to be in resonance with the ions to ensure that a maximum number of ions were addressed.
For a coasting ion beam, the time overlap is not critical because the ions are evenly distributed across the ring. For convenience, the laser timing in coasting-beam mode has not been changed to maintain the coincidence scheme for the laser and to record the fluorescence signal at the same time in one ion revolution.

5.3 Data Analysis

In this section the individual analysis steps are discussed, starting from the raw data to the extraction of the hyperfine splitting energy. The raw data in lmd-file format is unpacked and processed using *Go4*[2], a tool based on the analysis software *ROOT*, invented and maintained by GSI [128]. The *Go4* version used is based on code from previous beamtimes [108, 109], which is adapted to the current experimental setup. After the data processing and filtering is done in *Go4*, an *ASCII* text file is extracted for further data processing in *python*. Additional data

[2] GSI Object Oriented On-line Off-line system

like the measured wavelength and the high-voltage measurement, which are stored separately with a time stamp, are combined with the extracted data in *python* to derive the measured resonance positions. Details of these processes are presented in the following sections.

5.3.1 Go4-Analysis

The first step of the data analysis is to unpack the raw data. Each measurement run has a different data file that is analyzed separately. The data is unpacked event by event and an event corresponds to an MBS readout with $5\,\mathrm{ms}$ of data. In such an event, an array is created for each TDC channel, where counts are stored with precise timing information. Counts of scaler channels and other external data are stored without timing information in another array [128].
Once event processing is finished, the generated array of each channel is passed to the analysis step of *Go4*. In this step all events of a measurement are combined and different aspects can be analyzed. Important functionalities are for example the assignment of signal counts to the current laser scan step or the detection time in relation to the ion revolution in the storage ring.
To obtain a good Signal-to-Noise Ratio (SNR), the data is filtered in three steps. These filters are explained in more detail below. At the end of the *Go4* analysis, the final histogram of photon counts versus laser steps is saved in an *ASCII* text file, which can be processed in *python*.

Count Rate Filter

The count rate filter analyzes the sum of counts per event. Only real counts, which are caused by the fluorescence of excited residual gas or laser-induced fluorescence, should be considered for further processing. In particular, false counts generated by electrical noise should be identified and discarded. This can be done by fitting a probability distribution and ignoring events with counts outside of a certain limit.
Due to the independent and small number of photon counts, the probability for $x \in \mathbb{N}$ counts per event follows a Poisson distribution

$$P_\mu(x) = \frac{\mu^x}{x!} e^{-\mu} \tag{5.1}$$

with expectation value μ. To extract the unknown expectation value for a Poisson-distributed data set with n independent data points x_i, the Maximum Likelihood Estimation (MLE) can be used. The basic idea is to maximize the joint probability distribution of all data points by finding the underlying expectation value of the data set.

$$\mu_{\mathrm{MLE}} = \underset{\mu \in \mathbb{R}_{>0}}{\arg\max}\, \mathcal{L}(\mu) = \underset{\mu \in \mathbb{R}_{>0}}{\arg\max} \prod_{i=1}^{n} \frac{\mu^{x_i}}{x_i!} e^{-\mu} \tag{5.2}$$

Applying the natural logarithm simplifies the problem. Since the logarithm is monotonic, the maximum position does not change and it is more convenient to minimize the negative log

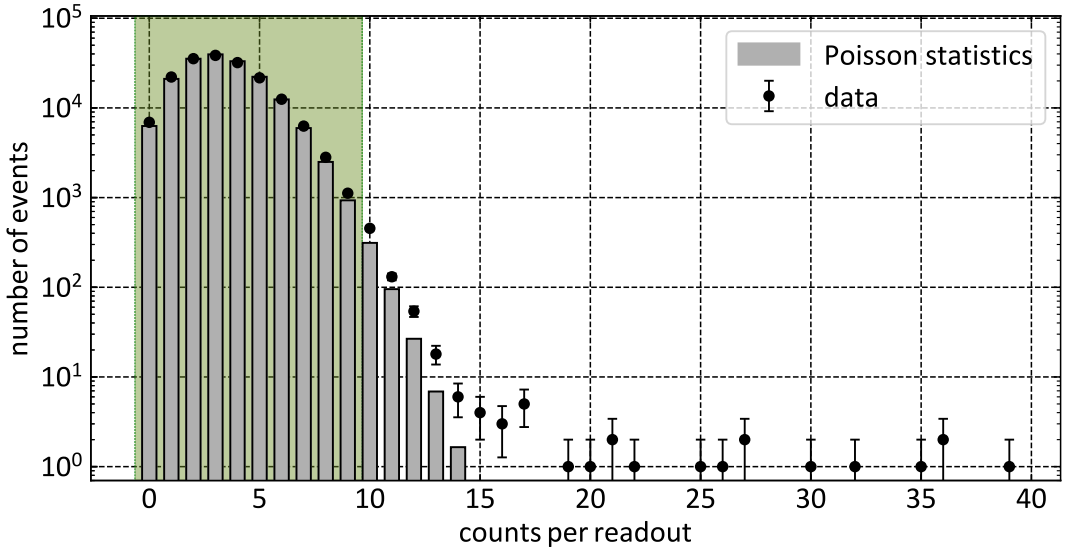

Figure 5.2: Example for a distribution of counts per readout from ^{209}Bi measurement #21. The bars represent the evaluated Poisson statistics with $\mu = 3.35$. Events with count rates higher than nine are outside of the 3σ-range and are discarded by the count rate filter.

likelihood function

$$-\ln \mathcal{L}(\mu) = -\ln\left(\prod_{i=1}^{n} \frac{\mu^{x_i}}{x_i!} e^{-\mu}\right) = \sum_{i=1}^{n} \ln(x_i!) + n\mu - \ln(\mu) \sum_{i=1}^{n} x_i. \tag{5.3}$$

Forming the derivative with respect to μ and setting it to zero yields the expectation value:

$$\mu_{\mathrm{MLE}} = \frac{1}{n} \sum_{i=1}^{n} x_i \tag{5.4}$$

In this case, it turns out that the expectation value is the sample mean of the data set. With this method, any data set can be analyzed and events with unrealistically high count rates can be discarded. Therefore, count rates within a confidence interval of $99.73\,\%$, which corresponds to a 3σ-range, are considered as correct. Fig. 5.2 shows an example of a count rate histogram for a ^{209}Bi measurement on a logarithmic scale.
The data points are measured data and the bar graph represents the evaluated Poisson statistics with $\mu = 3.35$. For this measurement, count rates above nine are discarded. In particular, single outliers with count rates above 15 can be easily identified as false counts. For the fitted statistics, occasional outliers do not significantly change the result because a data set typically consists of more than 10^4 events. To ensure that no signal counts are discarded, a 6σ-range is also tested for certain cases. This caused no change in resonance position or linewidth.

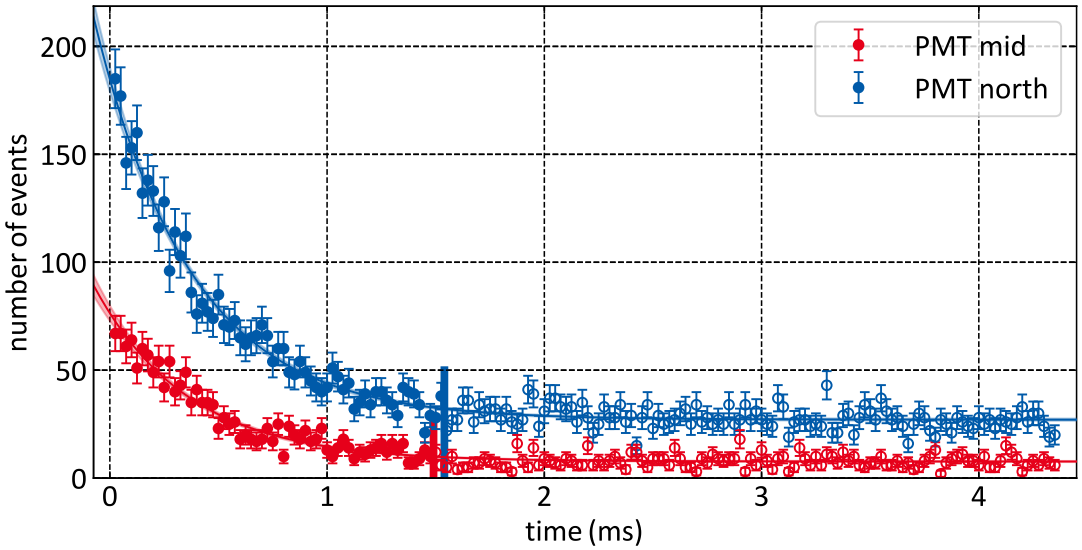

Figure 5.3: Counts of all ^{208}Bi bunched measurements are summed up and sorted into $25\,\mu s$ bins. At the beginning of the time axis, the ions are excited by the laser and the fluorescence signal decays exponentially with time. Fitting and comparing signal to background leads to fluorescence time windows of $1.49\,\mathrm{ms}$ (PMT mid) and $1.54\,\mathrm{ms}$ (PMT north), marked by the closed circles and the red and blue bars.

Fluorescence Time Window

An important method to improve the SNR is the implementation of a fluorescence time window. Due to the extended time of $33.3\,\mathrm{ms}$ between two laser pulses and the comparatively short lifetime of the upper hyperfine state of about $0.4\,\mathrm{ms}$ [52], no fluorescence signal is expected most of the time. The relevant time window starts with the laser pulse and ends when the fluorescence is no longer distinguishable from the background. This time window depends on the amount of ions and the storage ring conditions. Therefore, it has to be chosen individually for the four different cases, namely bunching/coasting measurements of ^{208}Bi/^{209}Bi.
To extract the relevant time window for a case, all data sets of this case are summed up. The counts are sorted into $25\,\mu s$ bins, starting with the laser pulse. The resulting exponential behavior of the detected fluorescence photons in bunched-beam mode of ^{208}Bi is shown in Fig. 5.3. After the laser excitation, a high count rate appears that decreases towards the background within $2\,\mathrm{ms}$. To determine the fluorescence time window an exponential decay with variable background is fitted to the data. Solving for time under the condition that the signal amplitude A decreases to the uncertainty of the background $\sqrt{B}$ leads to the fluorescence time window t_{FW}:

$$A \cdot \exp\left(-\frac{t_{\mathrm{FW}}}{\tau}\right) \stackrel{!}{=} \sqrt{B} \quad \Rightarrow \quad t_{\mathrm{FW}} = \tau \cdot \ln\left(\frac{A}{\sqrt{B}}\right). \tag{5.5}$$

Table 5.1: Fluorescence time window t_{FW} for different experimental conditions.

	$^{208}\mathrm{Bi}^{82+}$		$^{209}\mathrm{Bi}^{82+}$	
	PMT mid	PMT north	PMT mid	PMT north
bunched mode	$1.49\,\mathrm{ms}$	$1.54\,\mathrm{ms}$	$2.22\,\mathrm{ms}$	$2.35\,\mathrm{ms}$
coasting mode	$0.86\,\mathrm{ms}$	$0.99\,\mathrm{ms}$	$1.63\,\mathrm{ms}$	$1.99\,\mathrm{ms}$

In Fig. 5.3 the time t_{FW} is marked by the blue and red bar for PMT north and PMT mid. The result of the evaluation of this time is shown for all four cases in Tab. 5.1. The results are ranging between $0.9\,\mathrm{ms}$ to $2.4\,\mathrm{ms}$. Compared to the time between two laser pulses, this filter excludes more than $90\,\%$ of the measurement time and thus improves the SNR drastically.

Ion Revolution Gate

Another way to reduce the background is to introduce an ion revolution gate. This gate filters the data in the time frame of one ion revolution in the ESR and is applied after the fluorescence time window.
The ion revolution frequency during the ^{208}Bi measurements is close to $2\,\mathrm{MHz}$. This corresponds to a revolution period of $503\,\mathrm{ns}$ or about 151 bins of $10/3\,\mathrm{ns}$. To obtain the signal projected to one revolution in the storage ring, the modulo operation can be used in the analysis. This extracts the relative phase information from the TDC timing information.
In the case of a bunched beam measurement, the ions are forced into a bucket by the RF cavity. The emerging bunch covers only about $10\,\%$ of the ring circumference. A laser-induced photon can only be detected, while the bunch is in the detection region and only background is collected in the remaining time, as shown in Fig. 5.4a. The dominant background effect is the excitation or ionization of residual gas atoms or molecules by the inelastic collisions with the relativistic ion beam [129]. The relaxation back to the ground state can proceed through different states with different lifetimes. This leads to the emission of photons, which explains the slow decay of the background.
The extraction of the ion revolution gate for laser-induced fluorescence requires background subtraction. Therefore, the signal is accumulated for a fluorescence time window immediately after the laser pulse and compared to the signal intensity obtained within the same time window approximately $15\,\mathrm{ms}$ after the laser pulse. The first fluorescence time window contains both, laser-induced and ion-induced fluorescence, the second only ion-induced fluorescence. Due to the long beam lifetime of about $30\,\mathrm{min}$, a constant ion number between two laser pulses is assumed. In Fig. 5.4b the fit of a Gaussian function to the background corrected signal is shown. The flat background confirms the assumption of negligible ion loss between signal and background time window. The position of the ion bunch can be derived from the fit and the 3σ-region around the center is assigned as the ion revolution gate.
The situation is slightly different for a coasting beam measurement. The ions are distributed

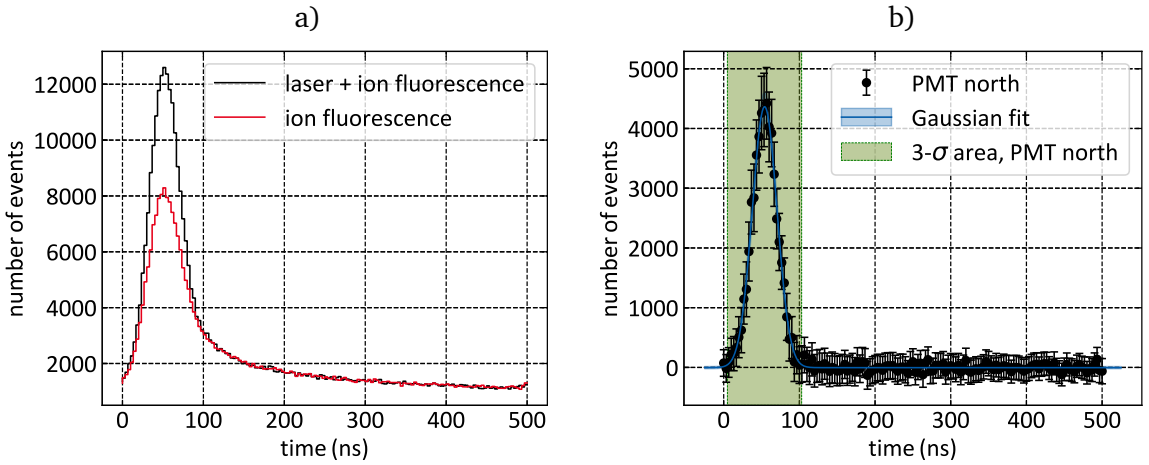

Figure 5.4: Photon counts summed up for all ^{209}Bi bunched measurements of PMT north with respect to one ion revolution of $503\,\mathrm{ns}$ in the ESR. In a) the signal immediately after a laser pulse is compared with the signal about $15\,\mathrm{ms}$ later. The delayed emission of fluorescence photons by the excited or ionized residual gas is clearly visible. b) shows only the laser-induced signal by performing a background correction. A Gaussian fit leads in this case to an ion revolution gate between $5\,\mathrm{ns}$ and $103\,\mathrm{ns}$.

across the whole circumference of the ESR. In this situation, the laser can only interact with a fraction of the stored ions. The resulting fluorescence signal depends on the laser-ion overlap and the number of ions which are excited by the short laser pulse. An estimate of the maximum overlap length is given by the distance between the dipole magnets of $18\,\mathrm{m}$. Taking into account the relativistic flight time t_{ion} of the ions, the laser transmission time t_{l} and the temporal width t_{lw} of the laser, the maximum temporal overlap t_{max} can be estimated:

$$t_{\mathrm{max}} = t_{\mathrm{ion}} + t_{\mathrm{l}} + t_{\mathrm{lw}} = 83\,\mathrm{ns} + 60\,\mathrm{ns} + 8\,\mathrm{ns} = 151\,\mathrm{ns}. \tag{5.6}$$

This is about $29\,\%$ of the ion revolution time of $503\,\mathrm{ns}$ and, thus, the maximum percentage of stored ions that can be addressed by the laser. In Fig. 5.5, the PMT signal accumulated for all runs is shown for coasting beam measurements of ^{209}Bi and ^{208}Bi, respectively. The signal has distinct edges in time and a plateau-like structure in the center. Such a shape is expected for an evenly distributed excitation over the straight section of the ESR. In contrast to the bunched measurement, the background corresponds to a constant value and does not change the signal position. This is caused by the coasting beam, which produces a constant rate of background photons, resulting in an average count rate. The background subtraction for ^{209}Bi is done to create a clear signal separation. This is not effective for ^{208}Bi due to the low count rate.
The ion revolution gate is chosen from the beginning to the end of each signal. For ^{208}Bi, one gate is applied for both detectors. The low count rates make it difficult to define the signal edges, so a larger gate is chosen to not discard any signal. In all cases the ion revolution gate

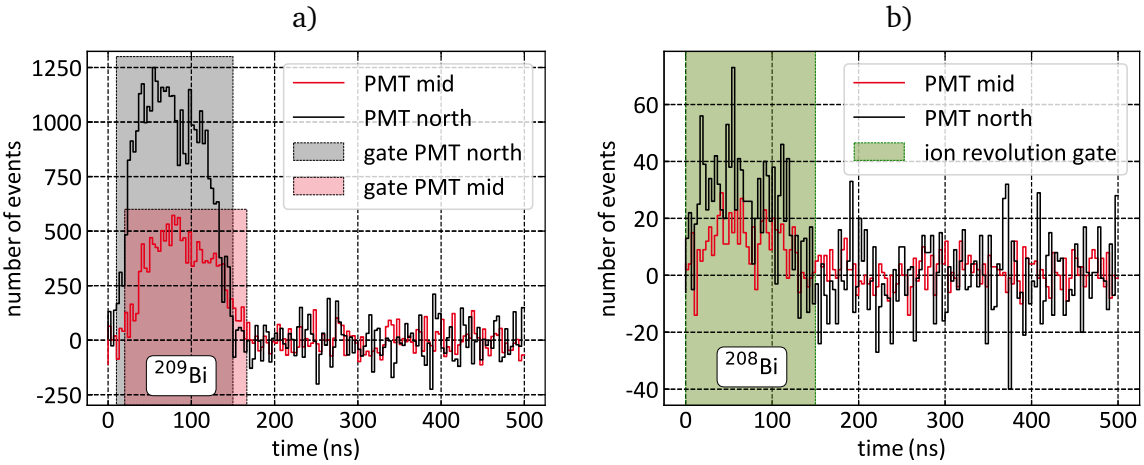

Figure 5.5: Photon counts with respect to one ion revolution of $503\,\mathrm{ns}$ in the ESR in coasting-beam mode. The data is accumulated for all measurement runs of one isotope. a) Shows the signal of ^{209}Bi with background subtraction and b) shows the signal of ^{208}Bi without background subtraction. The signals differ in total count rate, but are similar in arrival time and shape. The ion revolution gate is set at the highlighted areas.

is about $150\,\mathrm{ns}$ long. This agrees well with the previously calculated estimate and the laser-ion overlap can be assumed along the complete straight ESR section.

5.3.2 Python Analysis

After the data is unpacked and filtered by *Go4*, the result is passed to *python* using an *ASCII* text file. Each laser step is associated with a certain number of photon counts. In a measurement run, the laser is typically scanned two to four times in small wavelength steps across the resonance wavelength. In most of the cases the data from both PMTs are used, but in some cases the statistics in one of the two is not sufficient for further analysis.
To extract the resonance position of a particular measurement run, the data from both PMTs are fitted separately with a Gaussian distribution. If only one PMT has significant statistics, the resonance center can be extracted directly from the fit. Otherwise, the resonance position x_{res} is calculated from both fit results using the weighted average

$$x_{\mathrm{res}} = \frac{\sum_{i=1}^{n} \sigma_i^{-2} x_i}{\sum_{i=1}^{n} \sigma_i^{-2}} = \frac{\sigma_1^{-2} x_1 + \sigma_2^{-2} x_2}{\sigma_1^{-2} + \sigma_2^{-2}}. \tag{5.7}$$

Here x_i and σ_i are the resonance position and uncertainty obtained with the data from a single PMT, respectively. The combined uncertainty σ_{res} is given by the standard error of the weighted mean

$$\sigma_{\text{res}} = \sqrt{\frac{1}{\sum_{i=1}^{n} \sigma_i^{-2}}} = \sqrt{\frac{1}{\sigma_1^{-2} + \sigma_2^{-2}}}. \tag{5.8}$$

The application of this calculation is feasible, because there are no systematic differences in the measured resonance positions of the PMTs in all cases for which both signals are observed. The advantage of this method is, that each run contributes one resonance position, regardless of the number of PMTs that can be analyzed. This is important, because in addition to statistical fluctuations, systematic shifts can occur between measurement runs. Therefore, the two data sets from a run recorded by the two detectors cannot be considered as independent measurements. The improved statistics from having significant data in both PMTs is reflected in the reduction of the standard error.

Resonance Fits

As discussed in Sec. 2.5.1, the resonance signal has a Gaussian shape due to the thermal velocity distribution of the stored ions. Therefore, each valid data set is fitted with a Gaussian distribution

$$f(x) = a \cdot \exp\left(-\frac{(x - x_0)^2}{2\sigma^2}\right) + b. \tag{5.9}$$

The four free parameters are amplitude a, center x_0, linewidth σ and background b. In general, the data sets contain low count rates per laser step, due to the optimized background conditions and the applied *Go4* filters. This fact influences the choice of the fit routine and a standard χ^2-minimization is not suitable for evaluating the best model parameters, since the measured count rate per laser step is not normally distributed, but based on a Poisson distribution.
To find the parameters $\mathbf{p}$ of a model m (in this case a Gaussian distribution) that best describe the data points d_i, the MLE method (see also Sec. 5.3.1) is used. This method is implemented in the *python* package *kafe2*, which is used throughout the work. The goal is to find model parameters that maximizes the maximum likelihood function $\mathcal{L}$

$$\arg\max_{\mathbf{p}\in\mathbb{R}} \mathcal{L}(\mathbf{p}) = \arg\max_{\mathbf{p}\in\mathbb{R}} \prod_{i=1}^{n} P(m_i(\mathbf{p}), d_i). \tag{5.10}$$

Here $P(m_i(\mathbf{p}), d_i)$ is the probability to measure a data point d_i based on a model prediction $m_i(\mathbf{p})$. In case of normally distributed uncertainties for each data point, this approach leads to χ^2-minimization. For a Poisson distribution, this results in

$$\arg\max_{\mathbf{p}\in\mathbb{R}} \prod_{i=1}^{n} P(m_i, \mathbf{p}, d_i) = \arg\max_{\mathbf{p}\in\mathbb{R}} \prod_{i=1}^{n} \frac{m_i(\mathbf{p})^{d_i} e^{-m_i(\mathbf{p})}}{d_i!}. \tag{5.11}$$

Analogous steps to those used in Eq. 5.3 lead to the expression for the negative logarithmic likelihood function, which has to be minimized

$$-\ln \mathcal{L}(\mu) = \sum_{i=1}^{n} d_i \ln m_i(\mathbf{p}) - m_i(\mathbf{p}) - \ln d_i! \,. \tag{5.12}$$

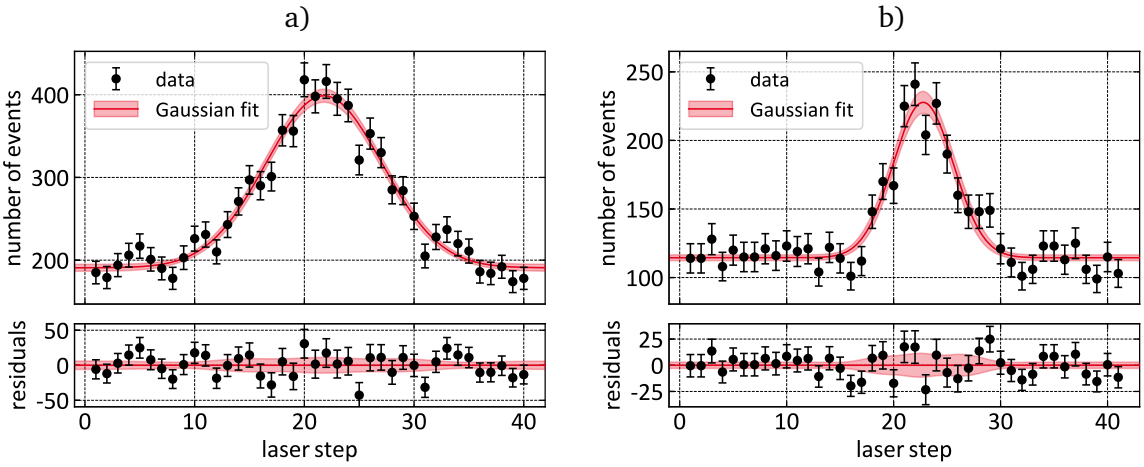

Figure 5.6: Typical resonance fits for a) bunched and b) coasting beam of ^{209}Bi (measurement #7 and #38). The reduced likelihood ratio $\mathcal{P}_{\text{rlr}}$ is 1.09 and 0.95, respectively.

Unlike the χ^2 minimization, the above term does not depend on uncertainties, only on the data and the model prediction. The uncertainty of each data point follows naturally from the choice of the Poisson distribution. Corresponding to the reduced chi-square value, the reduced likelihood ratio $\mathcal{P}_{\text{rlr}}$ is a measure of the quality of the fit

$$\mathcal{P}_{\text{rlr}} = \frac{-2 \ln \mathcal{L}_{\text{r}}}{n - n_p}. \tag{5.13}$$

Where n is the number of data points and n_p the number of model parameters. $\mathcal{L}_{\text{r}}$ is the likelihood ratio of the model function based on the given data points and the model of the underlying relationship. It has been shown for large sample sizes that $\mathcal{P}_{\text{rlr}}$ asymptotically agrees with the chi-square statistic [130]. A value of $\mathcal{P}_{\text{rlr}}$ close to 1 indicates an accurate description of the data by the model. This parameter is used to decide which data set has sufficient statistics for a fit. In case of ^{208}Bi the limit is set to 1.4 while for ^{209}Bi 1.8 is chosen. This corresponds to values, for which a reliable fit of the resonance is possible. In Fig. 5.6 and Fig. 5.7 typical resonance fits for ^{209}Bi and ^{208}Bi are depicted, respectively. The data points show a good agreement with the fitted Gaussian function.
Due to the low count rates - especially for ^{208}Bi - no background correction is performed. Subtracting two small count rates N_{sig} and N_{ref} in the statistical background leads to values close to zero, but the uncertainty grows as the individual uncertainties add up ($\Delta N = \sqrt{N_{\text{sig}} + N_{\text{ref}}}$). Therefore, a constant background is chosen as a model parameter. This approach is valid, because the ion lifetime is long compared to a laser scan and there is no ion loss induced slope in the background. The residuals in Fig. 5.6 and Fig. 5.7 confirm this assumption.
In order to assign the extracted resonance center in laser steps to the corresponding wavelength in the ion rest frame, two additional input parameters are crucial, namely the measured

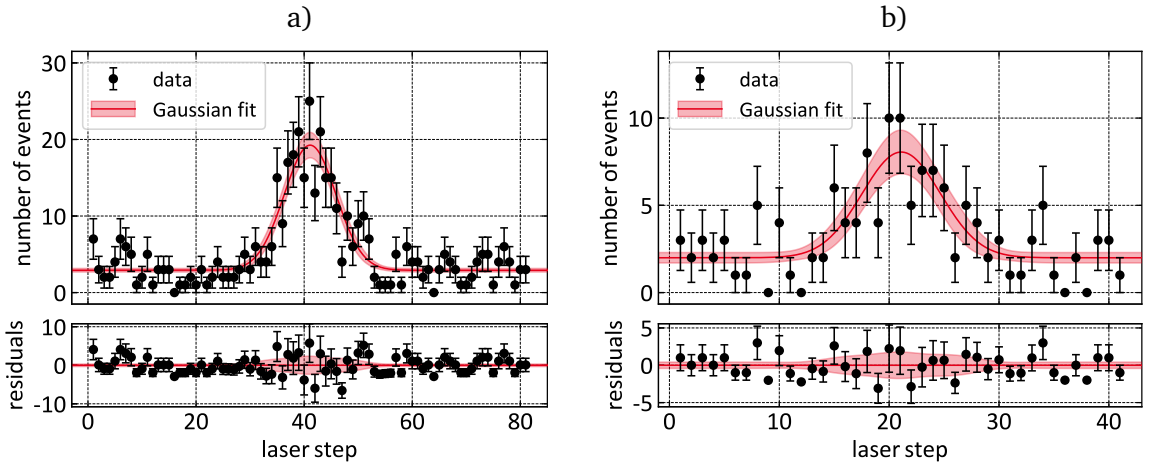

Figure 5.7: Typical resonance fits for a) bunched and b) coasting beam of ^{208}Bi (measurement #6 and #34). The reduced likelihood ratio $\mathcal{P}_{\text{rlr}}$ is 1.21 and 1.11, respectively.

wavelength in the laboratory frame and the high voltage applied at the electron cooler. This is discussed in the next section.

5.4 Extraction of the Measurement Wavelength

This section describes the laser wavelength measurement and how the resonance position in laser steps is converted to a wavelength in the ion rest frame.
The laser wavelength was continuously monitored during the beamtime by a WS/7-60 wavelength meter and the measurement was stored with a rate of $4\,\text{Hz}$. The wavemeter has been calibrated before and after the measurement campaign with a calibrated helium-neon laser with a wavelength of $632.9913(1)\,\text{nm}$.
The version of the wavelength meter used does not have an integrated trigger function to synchronize the wavelength measurement with the repetition frequency of the spectroscopy laser. To avoid overexposure of the photodiodes, the *exposure time* was set to $34\,\text{ms}$ and most of the time only one laser pulse was analyzed. In some cases, however, the measurement integrated over two laser pulses, causing an overexposure and the measurement failed.
Besides the missing trigger function, the laser light had to be coupled via a multimode fiber. This was necessary to achieve a sufficient level of laser power. A single mode fiber did not work, because either the exposure time was too long or the fiber was damaged by the high laser intensity. The beam profile after the multimode fiber, which showed some wavelength dependence, can lead to erroneous measurements. The combination of both effects prevents the use of the raw wavelength data.
Consequently, the wavelength steps are extracted from the dye-laser set value. Prior to a

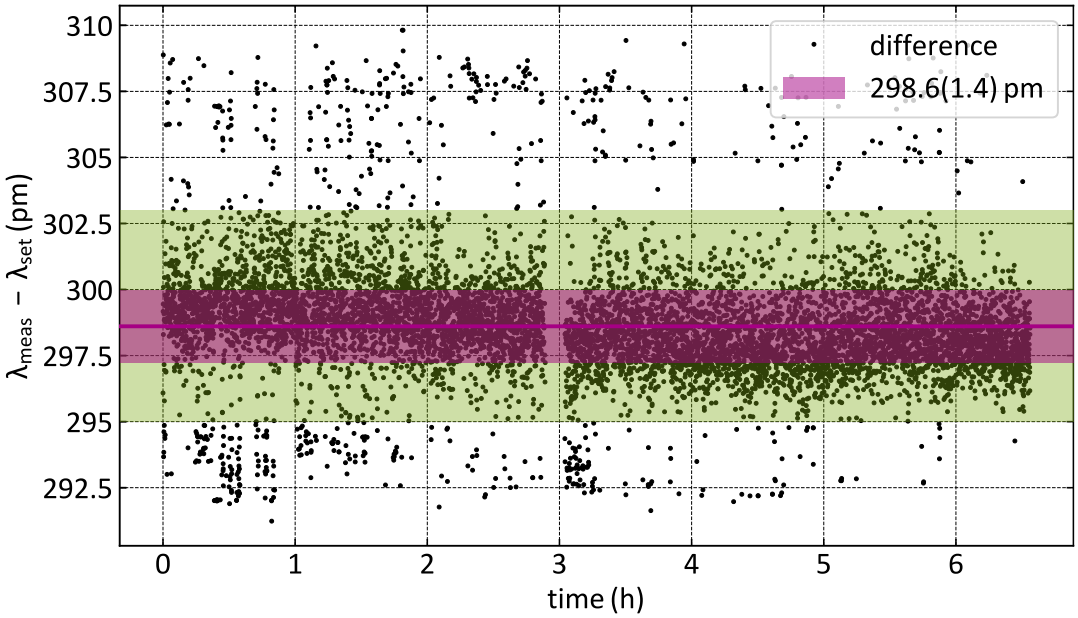

Figure 5.8: Difference of the measured (λ_{meas}) and the set wavelength (λ_{set}) for the measurement period between measurement #26 and #40. Data points in the green range are considered correct measurements and averaging results in an offset of $\Delta\lambda = 298.6\,(1.4)\,\text{pm}$. This offset can be used to reconstruct the true wavelength from the set value.

measurement, the dye-laser scan settings were specified with a start and stop wavelength and the number of laser steps. This results in well-defined wavelength steps, which can be compared to the wavemeter measurement. Therefore, the set value is subtracted from the wavelength meter data. This is shown for the $6.5\,\text{h}$ period between measurement #26 and #40 in Fig. 5.8 (only every tenth data point is plotted).
The subtraction reveals a range that contains the majority of the data points. Assuming that the wavelength meter measurement is correct most of the time, these data points can be considered valid measurements. Outside of this band are isolated or small clusters of data points, where the set value has a comparatively large difference to the wavemeter data. These points can be identified as erroneous measurements.
To assign the true laser wavelength to each laser step with distinct set value, the offset $\Delta\lambda$ is introduced. This offset is extracted by averaging all data points of a period that are considered valid measurements, as depicted by the green range in Fig. 5.8. For this example, the average is $\Delta\lambda = 298.6\,(1.4)\,\text{pm}$, whereby the uncertainty is the standard deviation of the data points. This offset can be added to the set value of a corresponding laser step in order to determine the actual laser wavelength of that step.
In general, subsequent runs with the same scan range are combined into one period. If measurements are stopped for an extended period of time or if there is a significant drift in the

Table 5.2: Calculated offsets between measured wavelength and dye laser set wavelength. Between measurements #14 and #15 of ^{209}Bi the measurements for ^{208}Bi are performed.

$^{209}Bi^{82+}$ ($\lambda = 602\,\mathrm{nm}$)			$^{208}Bi^{82+}$ ($\lambda = 549\,\mathrm{nm}$)		
Meas. #	$\Delta\lambda$ (pm)	Std. Dev. (pm)	Meas. #	$\Delta\lambda$ (pm)	Std. Dev. (pm)
1	326.8	1.0	1 - 5	306.1	2.1
2 - 4	325.6	1.1	6 - 8	303.5	1.8
5 - 9	324.6	0.9	9 - 12	301.8	2.0
10 - 12	324.3	0.9	13 - 25	300.1	1.6
13 - 14	323.2	0.9	26 - 40	298.6	1.4
$^{208}Bi^{82+}$ measurements					
15 - 16	318.9	1.4			
17 - 40	319.5	1.6			

raw data, individual averages are calculated.
In Tab. 5.2 the extracted offset $\Delta\lambda$ is shown for all measurements. The offset is about $0.32\,\mathrm{nm}$ for ^{209}Bi and $0.3\,\mathrm{nm}$ for ^{208}Bi measurements. The origin of the difference between set value and wavemeter measurement can be divided into three parts. About half of the offset is due to the wavelength difference between air and vacuum. While the wavelength meter measures the wavelength in vacuum, the dye laser set value is in air. The corresponding offset can be calculated with the refractive index of air $n_{\mathrm{air}} = 1.00028$ [73] according to

$$\Delta\lambda_n = \lambda_{\mathrm{vac}} - \lambda_{\mathrm{air}} = n_{\mathrm{air}} \cdot \lambda_{\mathrm{air}} - \lambda_{\mathrm{air}}. \tag{5.14}$$

This results in an offset of $\Delta\lambda_{n,208} = 0.15\,\mathrm{nm}$ for ^{208}Bi and $\Delta\lambda_{n,209} = 0.17\,\mathrm{nm}$ for ^{209}Bi. It should be noted that the refractive index depends on the temperature, pressure and humidity. A second part is ascribed to the fact that the dye laser has not been calibrated recently like the wavelength meter, which results in a calibration offset.
Finally, a drift from higher to lower offsets can be observed for both bismuth isotopes over the entire beamtime. Comparing measurement #2 with #40 of ^{209}Bi, which both have the same scan range and are taken $55\,\mathrm{h}$ apart, results in an offset difference of $6.1\,\mathrm{pm}$. Expressed in terms of frequency, this leads to $5\,\mathrm{GHz}$ or $91\,\mathrm{MHz/h}$. Such a drift cannot be explained by a drift of the wavelength meter measurement, which is on the order of $2\,\mathrm{MHz/h}$ [131]. Ultimately, it is unknown why the wavelength drifts at this rate during the beamtime. One possible reason is a temperature or pressure dependent influence on the frequency selective grating of the dye laser. By evaluating the average in regular time steps, this effect has been compensated, as can be seen in the results of Sec. 5.5.1, where no drift to lower wavelengths is observed.
In Fig. 5.9 the wavelength scans of measurement #33 are shown. The measurement run consists of two wavelength scans from set value $548.485\,\mathrm{nm}$ to $548.385\,\mathrm{nm}$. Offsetting the set

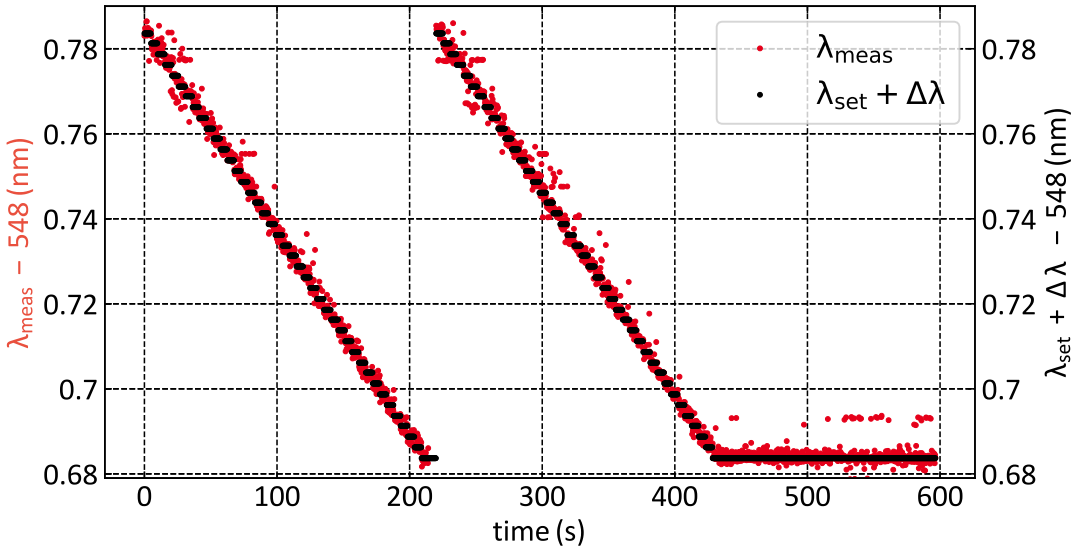

Figure 5.9: Wavelength scans of ^{208}Bi measurement #33. In this measurement run, the laser was scanned two successive times across the set wavelength (λ_{set}) range from $548.485\,\text{nm}$ to $548.385\,\text{nm}$. By adding the extracted offset of $\Delta\lambda = 298.6\,\text{pm}$ to the set values results in the black data points, which show a good agreement with the red data points of the wavelength meter measurement (λ_{meas}).

values by $\Delta\lambda$ =298.6 pm, as extracted from Fig. 5.8, results in the black data points. This agrees well with the wavemeter measurement (red) between wavelength $548.7837\,\text{nm}$ and $548.6837\,\text{nm}$. While the predominant agreement between shifted set values and measured values is evident, some measurements deviate significantly from adjacent ones. These can be explained by the non-ideal wavelength-meter setup and are considered as failed measurements.

With the method described above, the true start and stop wavelengths in the laboratory frame can be extracted for each measurement run. To transform the fitted center of resonance from laser steps (see e.g. Fig. 5.7) to a wavelength in the ion rest-frame, the laser wavelength has to be transformed to the moving ion frame due to the Doppler effect according to Eq. 2.63.
The ion velocity β_{ion} is in equilibrium with the electron velocity β_{e} and can thus be calculated from the high voltage measurement of the electron cooler voltage (Eq. 3.1). For each measurement run the average cooler voltage is taken and used for the entire dataset. The voltage can be considered stable during a run, with a typical standard deviation below $0.2\,\text{V}$. The calculation of β_{ion} includes the corrections due to the electron space charge and the contact potential, which will be discussed in 5.6.3.
To extract the resonance position of the hyperfine transition in the ion rest frame, the wavelength distance corresponding to the number of fitted laser steps is subtracted from the transformed laser start wavelength. The results of all measurements in ^{208}Bi and ^{209}Bi are presented in Sec. 5.5.

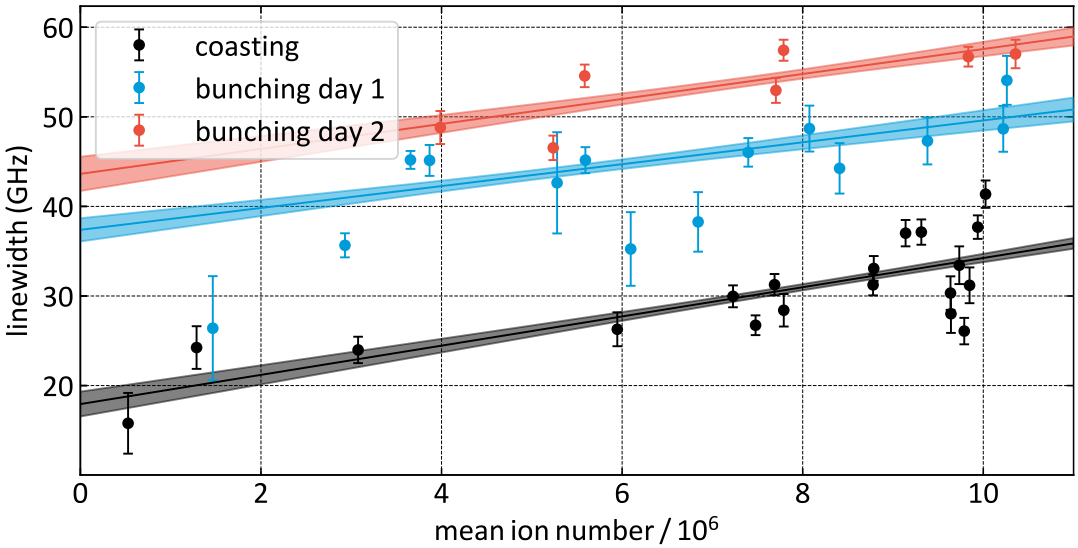

Figure 5.10: Resonance linewidth of all ^{209}Bi measurements versus the mean ion number. The linear fits show a proportionality between linewidth and ion number, which is expected, because heating intrabeam scattering effects are enhanced for larger ion numbers. In coasting-beam mode, the linewidth is significantly smaller than in the bunched-beam mode. Comparing the bunched measurements on different days shows a larger linewidth for the second day, indicating worse bunching settings.

5.4.1 Extraction of the Resonance Linewidth

Like the extraction of the resonance center, the linewidth σ of the fitted resonance in laser steps can be converted to wavelength or frequency in the ion rest frame. The resulting linewidth for all ^{209}Bi measurements with respect to the number of stored ions (the extraction of the ion number is explained in Sec. 5.6.4) is shown in Fig. 5.10.
The linear fits for different measurement settings show similar slopes with respect to the ion number of the measurement run. This is due to higher ion temperatures, since intrabeam scattering effects are enhanced for large numbers of ions. The resonance linewidth, on the other hand, is related to the temperature of the ion ensemble, as discussed in Sec. 2.5.1.
Another significant influence on the linewidth has the beam mode during the measurement. Comparing the data of the coasting with the bunched-beam measurement in Fig. 5.10, reveals an increase by a factor of about two for a bunched beam. This is caused by the force of the RF system, which compresses the ion beam into a bucket and causes synchrotron oscillations. This results in a heating effect on the ions. The comparison of the bunched measurements before (day 1) and after (day 2) the ^{208}Bi measurements shows also a difference. For day 2, the linewidth is broader, indicating that the bunching settings are worse than on day 1.
The resulting linewidth is not only a combination of several broadening mechanisms, but also

depends on the laser linewidth. Transforming the $9.7\,\mathrm{pm}$ of the FWHM laser linewidth in the laboratory frame to the σ linewidth in the ion frame, results in $\sigma_{\text{laser, ion}} = 10.1\,\mathrm{GHz}$. This is the main distribution for small ion numbers in coasting-beam mode, since extrapolating the linewidth of the coasting beam data to very small ion numbers yields a linewidth of $17.9(14)\,\mathrm{GHz}$. The remaining part may be due to other beam heating effects, such as scattering with residual gas, or the temperature of the electron beam in the electron cooler.
For the ^{208}Bi measurements, the ion numbers are low and quite constant at about 5×10^5 (see Sec. 5.6.4). Therefore, no linear dependence with respect to the ion number is observed and the extraction of the linewidth by a weighted average is justified, which yields

$$\sigma_{208,\text{bunch}} = 28(4)\,\mathrm{GHz} \quad \text{and} \quad \sigma_{208,\text{cw}} = 17(5)\,\mathrm{GHz}. \tag{5.15}$$

The uncertainty is extracted from the standard deviation of the data set. Again, the linewidth for the bunched-beam mode is broader than for the coasting mode. The linewidth of coasting measurements is the same as the lower limit for ^{209}Bi coasting measurements and is dominated by the laser linewidth.

5.5 Extraction of the Hyperfine Splitting Energy

This section presents the results for the hyperfine splitting energy for $^{209}\mathrm{Bi}^{82+}$ and $^{208}\mathrm{Bi}^{82+}$ in the ion rest frame. The resonance position of a single measurement is obtained using the method described in 5.4. To extract the combined transition wavelength of all measurement runs, the weighted average (Eq. 5.7) is used. This takes into account the uncertainties of individual runs. To assign an uncertainty to this mean value, the standard error of the weighted mean (Eq. 5.8) and the standard error of the arithmetic mean

$$\sigma_{\text{am}} = \frac{\sigma}{\sqrt{n}}, \tag{5.16}$$

with the standard deviation σ of a data set with n values, are compared. Since σ_{am} results in larger uncertainties, it is chosen as the total uncertainty. Due to the large number of independent measurements, a statistical error is obtained that is small compared to the evaluation of a single data set. It has to be emphasized that the result of this section is assumed to cover only statistical uncertainties. In addition, systematic effects may affect the results of individual runs in different ways, thus increasing the statistical uncertainty in this consideration. Systematic effects are discussed in detail in section 5.6.

5.5.1 Hyperfine Splitting of $^{208}\mathrm{Bi}^{82+}$

In Fig. 5.11 the extracted resonance position of all 40 independent measurement runs of $^{208}\mathrm{Bi}^{82+}$ are presented. The calculation of the combined ion rest frame wavelength in vacuum yields

$$^{208}\lambda_{\text{res}} = 221.440\,88(12)\,\mathrm{nm}. \tag{5.17}$$

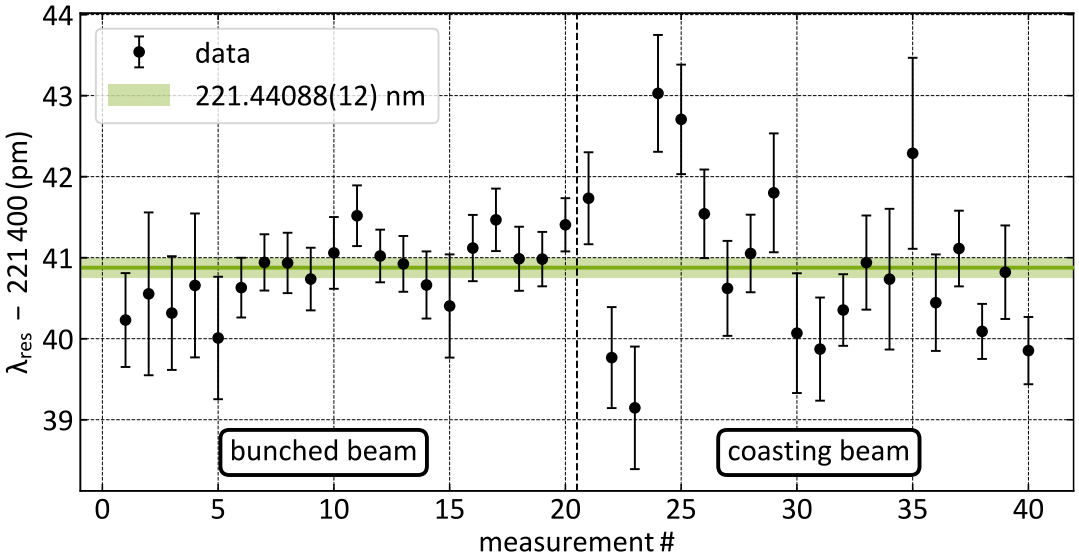

Figure 5.11: Measurement results of the $1s$ hyperfine transition wavelength in $^{208}Bi^{82+}$. The weighted mean corresponds to $^{208}\lambda_{res} = 221.440\,88(12)\,\mathrm{nm}$ where only statistical uncertainties are considered.

The data points are symmetrically distributed around the calculated mean value and agree within their 3σ-uncertainty range. Individual outliers could be suspect to systematic influences. Until measurement #20 a bunched ion beam is used and afterwards a coasting beam. There is no evidence of a systematic influence of the beam mode.

5.5.2 Hyperfine Splitting of $^{209}Bi^{82+}$

In Fig. 5.12 the individual measurements of the hyperfine splitting in $^{209}Bi^{82+}$ are shown. It is apparent, that in this case a systematic effect shifts several data points to higher or lower resonance wavelength. Measurements #1 to #21 are conducted in bunched-beam mode and measurements #22 to #40 in coasting-beam mode. Furthermore, the settings may have changed between measurements #14 and #15, since the measurement runs of the second isotope, $^{208}Bi^{82+}$, are performed there for about $30\,\mathrm{h}$. Thus, all parameters of the storage ring operation have been changed and readjusted between these measurements.
For measurements #15 to #21, a post-beamtime comparison of the Schottky data shows a shift of the central revolution frequency of the ions to higher values after switching on the bunching amplitude at the beginning of the measurement phase. As an example, the cutout of the Schottky signal from measurement #21 is depicted in Fig. 5.13a and compared to a well-matched bunching frequency for ^{208}Bi measurement #20 (Fig. 5.13b). A shift occurs when the bunching frequency is not perfectly matched to the high voltage of the electron cooler. Usually this is carefully tuned when the beam is set up, but it is not possible to reconstruct in retrospective why a mismatch occurs for individual data points.

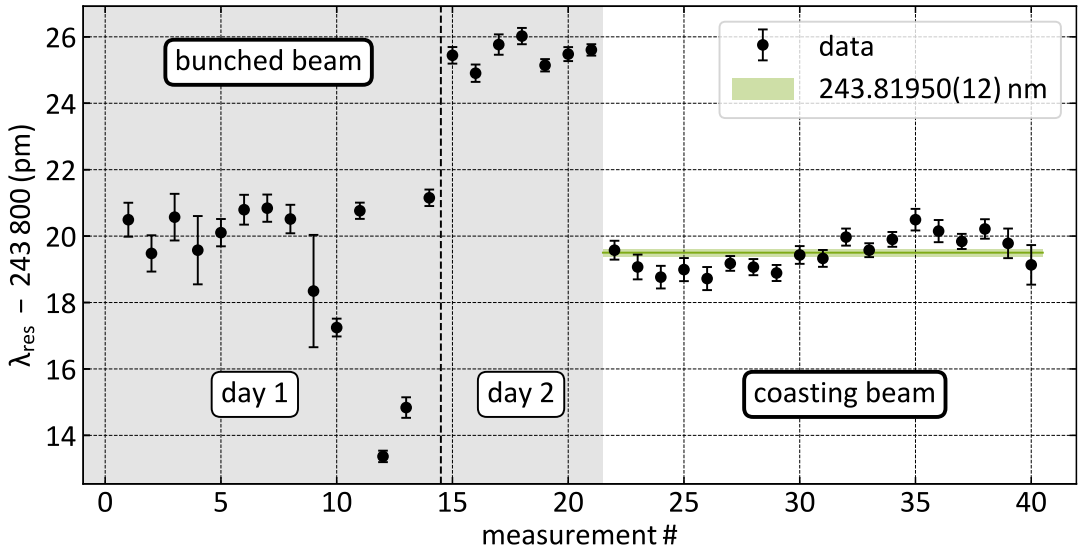

Figure 5.12: Measurement results of the $1s$ hyperfine transition wavelength in $^{209}Bi^{82+}$. The weighted mean of the runs in coasting-beam mode is $^{209}\lambda_{res} = 243.819\,50(12)\,\mathrm{nm}$ where only statistical uncertainties are considered. The discrepancy to the bunched-beam mode is discussed in the text.

It should be noted that the bunching force is stronger than the cooling force of the electron cooler. Thus, the beam energy is dominated by the bunching frequency. This also introduces additional heating effects and the ion temperature will be higher than in the case of a well matched bunching frequency. Such an effect can be seen in the extracted linewidths in Fig. 5.10 by comparing the measurements until #14 (day 1) with measurements #15 to #21 (day 2), which show a broader linewidth.
The increase of the central revolution frequency due to the bunching process indicates higher ion energies and will therefore result in a larger Doppler shift. The higher velocity causes the resonance to appear at lower laser frequencies and thus at higher wavelengths in the ion rest frame. The extracted wavelengths for measurement #1 to #14 in bunched-beam mode appear to be in better agreement with the coasting-beam data, except for a few outliers. Unfortunately, the Schottky data for this period is corrupted and cannot be used to reconstruct the match of the bunching frequency.
Under these circumstances, the hyperfine splitting of $^{209}Bi^{82+}$ is extracted solely from the 19 coasting-beam measurements. These data points line up along a constant value of

$$^{209}\lambda_{res} = 243.819\,50(12)\,\mathrm{nm}. \tag{5.18}$$

This also supports the assumption that the systematic effect is indeed caused by the bunching cavity, since there is no outlier in coasting-beam mode.

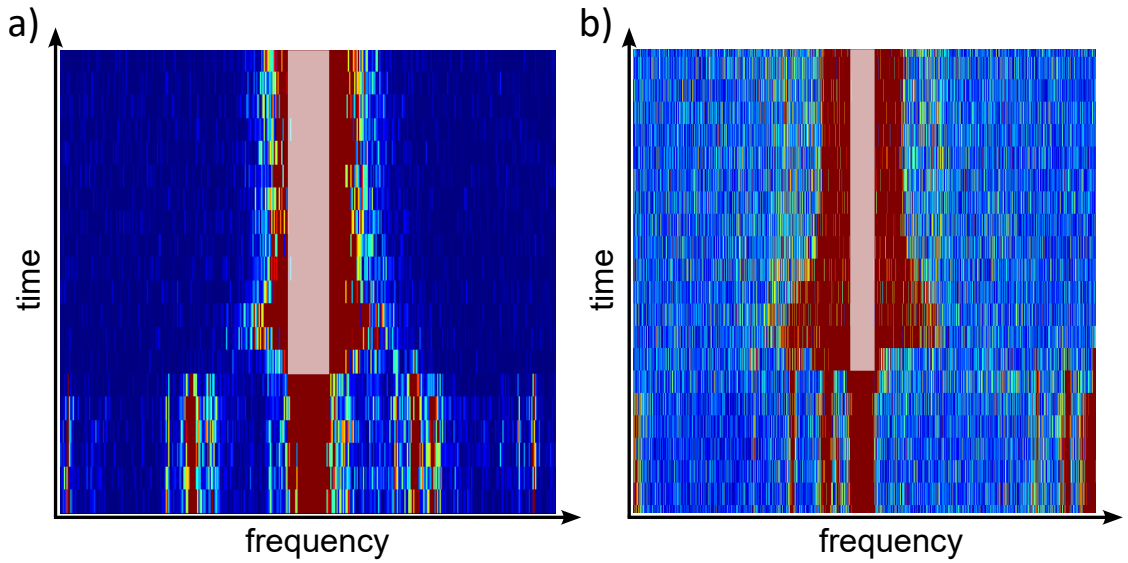

Figure 5.13: Cutout of the Schottky signal (123rd harmonic) at the beginning of the bunching process for ^{209}Bi measurement #21 (a) and for ^{208}Bi measurement #20 (b). The white area represents the ion revolution frequency of the coasting beam before bunching. In both cases the frequency distribution becomes larger due to the heating effect of the bunching process. In a) an additional shift of the central revolution frequency to a higher frequency corresponding to a higher ion energy is observed. In b) the bunching does not affect the central ion energy. Data extracted and provided by S. Sanjari [100].

5.6 Evaluation of Systematic Effects

Despite the fact that measurements are repeated several times during the experiment with the same settings, the results can vary in a non-statistical way. This is caused, for example, by a temporal drift of the laser frequency due to a change in temperature or pressure. Another factor is the significant influence of the electron velocity in the electron cooler on the measured resonance. The velocity is affected by space charge effects and by the applied acceleration voltage, which cannot be exactly quantified by measurements. Their influence is not expected to scatter statistically, but rather to affect all measurements systematically.
In order to derive the correct value from the measurement data and to assign a realistic uncertainty, it is essential to analyze and understand systematic effects. In some cases it is possible to correct for shifts, in others an uncertainty has to be assigned to the results. In the following part, several systematic effects are discussed, which can ultimately be combined to form the overall measurement uncertainty.

5.6.1 Wavelength Measurement

The procedure for extracting the laser wavelength from the wavelength-meter measurement and assigning it to a laser step is discussed in Sec. 5.4. The systematic uncertainty introduced by calculating the set-wavelength offset by averaging, can be estimated by the standard deviation of this offset. In case of $^{209}Bi^{82+}$ the highest uncertainty listed in Tab. 5.2 for one period is $1.6\,\mathrm{pm}$ and for $^{208}Bi^{82+}$ this uncertainty is $2.1\,\mathrm{pm}$ in the laboratory frame. These values are used for all measurement of the respective isotope.
Besides the extraction of the wavelength, systematic uncertainties of the wavelength-meter model as specified by the manufacturer must be taken into account. The absolute frequency accuracy is provided as $60\,\mathrm{MHz}$ or $0.1\,\mathrm{pm}$ at the wavelengths of interest. Another $0.3\,\mathrm{pm}$ has to be considered for the calibration with the He-Ne laser. The wavelength meter measurement is also suspect to statistical drifts. Based on a long-term He-Ne laser measurement, this statistical uncertainty is pessimistically assumed to be $0.3\,\mathrm{pm}$. Thus, the intrinsic statistical and systematic uncertainties of the wavelength meter are small compared to the offset extraction.

5.6.2 Spectral Distribution of Laser Light

Pulsed laser light consists of a broad wavelength spectrum. The possible wavelengths are determined by the gain medium and the allowed longitudinal resonator modes. In case of the used Cobra Stretch laser the dye has a broad gain spectrum ($541\,\mathrm{nm}$ to $571\,\mathrm{nm}$ [132]) and the wavelength selection is realized with a grating in combination with a mirror, which can be tilted in small increments.
During the beamtime the double bandwidth mode is used. In this configuration, the prism expander illuminates parts of the grating to produce a linewidth with FWHM of $9.7\,\mathrm{pm}$. The pulse energy is distributed over this wavelength range, but a symmetric distribution around the center wavelength is not guaranteed. An asymmetric line shape would result in a shift of the resonance, which is directly related to the center offset.
The uncertainty is conservatively estimated, as in [108], to be a quarter of the FWHM

$$\Delta\lambda_{\mathrm{asy}} = \frac{\mathrm{FWHM}}{4} = \frac{9.7\,\mathrm{pm}}{4} = 2.4\,\mathrm{pm}. \tag{5.19}$$

5.6.3 Electron Cooler

The velocity of a stored electron-cooled coasting ion beam is determined by Eq. 3.1 through the energy of the electrons in the electron cooler. This energy is mainly determined by the applied acceleration voltage, but is also influenced by space charge and contact potentials. Since the transformation of the laboratory wavelength into the rest frame of the ions depends directly on their velocity (see Eq. 2.63), it is inevitable to measure the electron acceleration voltage accurately and to consider systematic effects on it.

High Voltage Measurement

As explained in 3.2.1 the acceleration voltage in the electron cooler is measured by a combination of a high voltage divider and a digital multimeter. The installed divider has a divider ratio of $248\,517$ with a 1σ-uncertainty of $20\,\mathrm{ppm}$ [93]. The voltage across the final, high accuracy resistor is below $1\,\mathrm{V}$ and is measured by a Keysight 34465A multimeter with 6.5 digits resolution. The manual of the device [133] states a 1σ-uncertainty of $13.5\,\mathrm{ppm}$ for the applied settings. Combining both values to a total uncertainty for the high voltage measurement via Gaussian error propagation yields $24.2\,\mathrm{ppm}$ or $5.5\,\mathrm{V}$ at the applied voltage of about $225\,\mathrm{kV}$. Using Eq. 2.63 in case of $^{208}\mathrm{Bi}^{82+}$, this translates into a wavelength uncertainty in the ions rest frame of $2.3\,\mathrm{pm}$. With a relative uncertainty of $10.3\,\mathrm{ppm}$, this represents the leading uncertainty of the experiment.

Space Charge Correction

Besides the high voltage at the electron gun U_{EG}, the space-charge potential from the dense electron beam modifies the electric potential experienced by the inner electrons as well as the ions (see Sec. 2.3.1). Using Eq. 2.29 for the ESR electron cooler with $R_{\mathrm{D}} = 100\,\mathrm{mm}$ and $R_{\mathrm{e}} = 25.4\,\mathrm{mm}$, $\beta = 0.72$ and $r = 0$ yields

$$U_{\mathrm{SC}}(0) = -0.156\,\frac{\mathrm{V}}{\mathrm{mA}} \cdot I_{\mathrm{e}}[\mathrm{mA}]. \tag{5.20}$$

A typical cooler current of $200\,\mathrm{mA}$ leads to an effective reduction of the electron acceleration potential of $31\,\mathrm{V}$ in the beam center. This effect decreases radially towards the edge of the beam. During the measurement run, the ion beam radius is only of the order of a few mm. Thus, the position of the ion beam inside the electron cooler has a significant influence on the ion velocity.

To investigate the effects of space-charge potentials, the electron-cooler current in coasting-beam mode was systematically varied during the beamtime between $50\,\mathrm{mA}$ and $200\,\mathrm{mA}$. Two separate $^{209}\mathrm{Bi}^{82+}$-resonances are recorded for each electron current. The black data points in Fig. 5.14a display the resonance positions using the measured electron cooler voltage for the rest frame transformation without any space charge correction in the data analysis. It is important to note that a change of the electron current in the control system provokes an automatic change of the acceleration voltage of the electrons in order to compensate for the change of the space charge, which is shown in Fig. 5.14b.

This compensation can be extracted by analyzing the measured voltage for different current settings. Fitting a straight line results in a slope of $0.168\,\mathrm{V/mA}$, close to the theoretical calculation of Eq. 5.20. Applying this correction factor to the measured voltage for the rest frame transformation yields the orange data points in Fig. 5.14a. The linear correlation between electron current and resonance position is still evident. This indicates that the space-charge correction-model used in the control system is not accurate but overcompensates the effect slightly.

The measured resonance positions can actually be used to get a more accurate space-charge

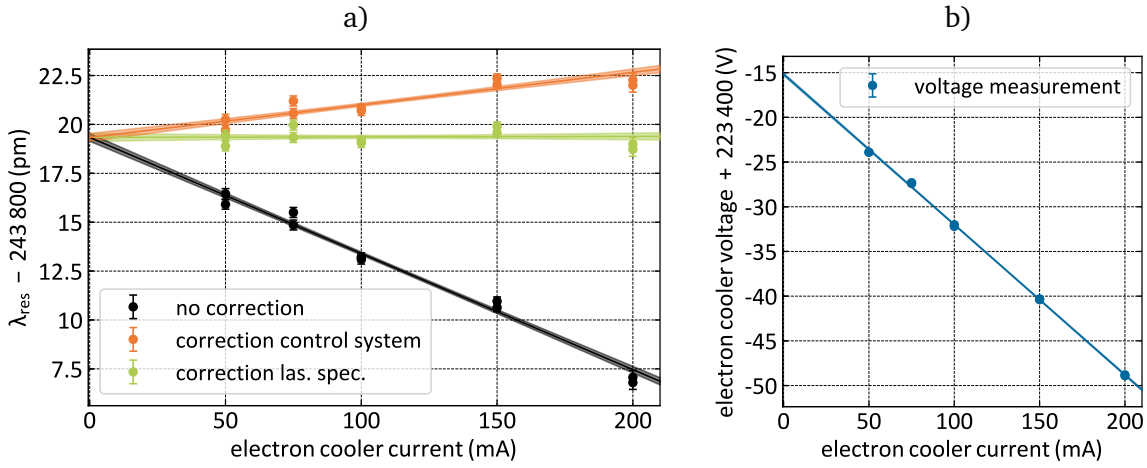

Figure 5.14: a) Resonance wavelength in the ion rest frame as a function of the electron cooler current for different space charge corrections. The green data points represent the experimentally extracted space charge correction with a slope of $-0.129\,\mathrm{V/mA}$. b) Automatic adjustment of the electron cooler voltage by the control system to compensate for the change of the space charge.

correction factor, since the resonance wavelength must not depend on the electron current. Instead, the data points should scatter around a constant value, if the ion velocity, i.e. the space charge correction, is chosen correctly. By varying the correction factor while analyzing the transformed resonance positions, the correlation between the electron current and the rest frame transition wavelength is vanishing for a correction factor of $-0.129\,\mathrm{V/mA}$, as shown by the green data points in Fig. 5.14a. This correction will be used in the remainder of this work. The experimentally determined space-charge potential is smaller than the theoretical minimum for $r = 0$. Since R_D and R_e are storage ring constants, the discrepancy can be attributed to the ion beam position within the electron cooler. An ion beam offset of $20.4\,\mathrm{mm}$ explains the extracted result. This value is consistent with scraper measurements of the ion beam during the beamtime, indicating a displacement from the central orbit. This shows that laser spectroscopy is a precise tool for investigating storage ring parameters that are challenging or impossible to access by conventional methods, as also discussed in [75].
The statistical uncertainty of this method can be extracted from the linear fit of the green data points with vanishing slope, which amounts to an offset uncertainty of $0.2\,\mathrm{pm}$. Due to the small number of data points and the lack of an additional independent data set, it is difficult to assign a systematic uncertainty. Therefore, a $2\,\mathrm{mm}$ displacement of the ion beam with respect to the extracted spatial position in the electron beam is assumed. A correction factor of $-0.135\,\mathrm{V/mA}$ is obtained from Eq. 2.29 for a shift towards the electron beam center and of $-0.123\,\mathrm{V/mA}$ for a shift away from the electron beam center. Multiplying the symmetrical difference of $0.006\,\mathrm{V/mA}$ by the highest electron current of $200\,\mathrm{mA}$ used for spectroscopy

results in a systematic uncertainty of $1.2\,\mathrm{V}$.

Contact Potential

A contact potential builds up between two materials with different work functions $W_{\mathrm{A},1}$ and $W_{\mathrm{A},2}$. The electrons from the material with higher work function (1) enter the material with the lower work function (2) until an equilibrium is reached. In this case, material 1 becomes positively and 2 negatively charged and the contact potential U_{cp} amounts to

$$U_{\mathrm{cp}} = \frac{W_{\mathrm{A},1} - W_{\mathrm{A},2}}{e} \tag{5.21}$$

[134]. For the ESR electron cooler, the drift tube is made of stainless steel, while the electron cathode is made of tungsten and coated with barium to optimize its efficiency. The work function of stainless steel is $W_{\mathrm{A,steel}} = 5.0\,\mathrm{eV}$ [135] and for a tungsten-barium compound $W_{\mathrm{A,W\text{-}Ba}} = 1.7\,\mathrm{eV}$ [48]. These values are measured under ideal conditions and may deviate in different experimental environments. Effects that can have an influence on the work function are, e.g., impurities, inhomogeneities or surface roughness and therefore a conservative uncertainty of $1\,\mathrm{eV}$ is considered for both materials [136].
According to [137], the contact potential present in the ESR electron cooler can be derived from the potential difference $\Delta\phi$ between cathode ϕ_{cat} and drift tube ϕ_{drift} potential

$$\begin{aligned}\Delta\phi = \Delta\phi_{\mathrm{cat}} - \Delta\phi_{\mathrm{drift}} &= \left(U_{\mathrm{cat}} - \frac{W_{\mathrm{A,W\text{-}Ba}}}{e}\right) - \left(U_{\mathrm{drift}} - \frac{W_{\mathrm{A,steel}}}{e}\right) \\ &= (U_{\mathrm{cat}} - U_{\mathrm{drift}}) - \left(\frac{W_{\mathrm{A,W\text{-}Ba}}}{e} - \frac{W_{\mathrm{A,steel}}}{e}\right) = U_{\mathrm{HV}} + U_{\mathrm{cp}} = U_{\mathrm{HV}} + 3.3(1.5)\,\mathrm{V}.\end{aligned} \tag{5.22}$$

Here U_{HV} is the negative high-voltage generated by the power supply of the electron cooler. The contact potential effectively reduces the electron acceleration voltage by a considerable amount of $U_{\mathrm{cp}} = 3.3(1.5)\,\mathrm{V}$.

5.6.4 Ion Current

In order to draw conclusions about the influence of the ion current, it has to be extracted from the raw data first. During an ESR experiment, the ion current is continuously and non-destructively measured by DC-Trafo GE02DT-ML [95], as explained in subsection 3.2.2. The data is stored with a time stamp in a separate database and can be combined with the start and stop times of the laser scans to extract the ion number for a measurement run.
The ion current in the storage ring decays exponentially with time during a measurement. This is mainly due to interactions with residual gas ions or electrons in the electron cooler. Such interactions can lead to energy loss or charge exchange of the particles. While the former can be partially compensated by the electron cooler, the latter always leads to a change of orbit and thus to ion losses. Another factor affecting the amount of ions available for the experiment, is the number of ions provided by the GSI accelerator chain and the efficiency of injection and

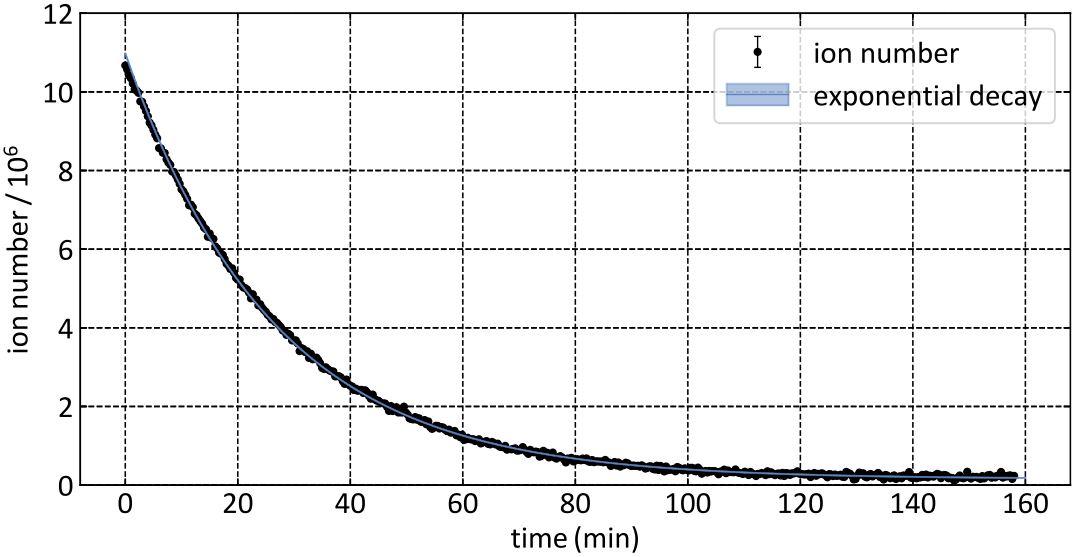

Figure 5.15: Ion number versus time for the last filling of the ESR. The ion lifetime is τ = $27\,\mathrm{min}$ and the offset is N_{offset} = 1.5×10^5. ^{209}Bi measurements #37 to #40 were performed in the first $90\,\mathrm{min}$ of the time period shown.

cooling in the ESR.
Usually each measurement run starts with a new ion injection. In some cases several measurement runs are performed for one injection. This is the case for four consecutive measurements of $^{209}Bi^{82+}$. They were performed with the last filling of the ESR at the end of the beamtime, which is shown in Fig. 5.15. After $90\,\mathrm{min}$, the number of ions was insufficient to extract the hyperfine transition by laser spectroscopy. However, the remaining ions were stored for another hour until the ion signal on the Schottky detector disappeared. Fitting an exponential decay with the initial ion number N_{i}

$$N(t) = N_{\mathrm{i}} e^{-\frac{t}{\tau_{\mathrm{i}}}} + N_{\mathrm{offset}} \tag{5.23}$$

provides the lifetime τ_{i} and the measurement offset N_{offset}. A lifetime of $\tau_{\mathrm{i}} = 27\,\mathrm{min}$ is a typical value for stored heavy and highly charged relativistic ion beams in the ESR and is possible due to the ultra-high vacuum conditions below $10^{-10}\,\mathrm{mbar}$. The extracted offset of

$$N_{\mathrm{offset}} = 1.5 \times 10^{-5} \mathrel{\widehat{=}} 4\,\mu\mathrm{A} \tag{5.24}$$

originates from the DC-Trafo measurement principle and has to be subtracted in order to get the correct number of ions. This offset is influenced, for example, by stray magnetic fields from the nearby quadrupole magnet, depending on the storage ring settings. Offsets up to $10\,\mu\mathrm{A}$ are expectable according to the manual [95]. Since the ring settings are similar for both isotopes, the extracted offset is also assumed for ^{208}Bi measurements.
During the beamtime campaign, the range of the DC-Trafo was set to $300\,\mu\mathrm{A}$. In this mode up to 1.1×10^7 Bi^{82+}-ions can be measured. At the other end of the scale, if a minimum resolution

Table 5.3: Number of $^{209}Bi^{82+}$ ions in successive measurements within one ion injection.

Meas. #	$N_{\text{ion, start}}$	$N_{\text{ion, stop}}$	Duration (min)
37	1.1×10^7	4.6×10^6	23
38	4.6×10^6	1.9×10^6	22
39	1.9×10^6	8.0×10^5	22
40	8.0×10^5	3.4×10^5	22

of $1\,\%$ (i.e. $3\,\mu A$) is assumed, a minimum ion number of 1.1×10^5 ions is still detectable.
The $^{209}Bi^{82+}$ ion numbers per measurement run can be approximated by averaging over the measurement period and range between 10^6 to 10^7 ($26\,\mu A$ to $260\,\mu A$). For $^{208}Bi^{82+}$ the ion numbers are between 3×10^5 to 5.5×10^5($8\,\mu A$ to $14\,\mu A$) and thus significantly lower due to the additional neutron-removal reaction that has to happen during the stripping process.
The large range of different ion numbers stored in the ring, and particularly the large disparity for $^{208}Bi^{82+}$ and $^{209}Bi^{82+}$, requires a discussion of possible systematic influences. Analogous to the considerations in Sec. 5.6.3, a high ion current can cause a positive space-charge potential, which accelerates electrons in the electron cooler. This in turn increases the ion velocity and affects the Doppler effect. In bunched-beam mode this space-charge effect would be enhanced, but is compensated by the applied bunching force, which is stronger than the electron cooler force [109].
Therefore, the effect of different ion currents on the resonance position is especially important in coasting-beam mode. Since the ion number for a $^{209}Bi^{82+}$ measurement varies between 10^6 and 10^7, while it is almost constant and significantly lower for $^{208}Bi^{82+}$, it is more probable that it can be observed for ^{209}Bi.
To avoid the influence of other systematics, the resonance positions of the four consecutive measurements of Fig. 5.15 are analyzed. These measurements are performed in sequence without a new ion injection and differ only in the number of stored ions. In Tab. 5.3 the ion numbers for start and stop ($N_{\text{ion, start}}$, $N_{\text{ion, stop}}$) of the laser scans are listed. Extracting the resonance position for measurements #37 to #40 yields the graph shown in Fig. 5.16a. The result is consistent with a constant value and no significant influence of the ion current can be observed.
To further investigate the effect of the ion current on the resonance center, the extracted resonance wavelengths of all $^{209}Bi^{82+}$ coasting-beam measurements are plotted versus the mean ion number in Fig. 5.16b. The measurements are taken over a period of eight hours and other systematics besides the ion current could be present. However, even in this case no effect that shows the expected functional behaviour can be observed.
Based on these observations, a systematic effect due to different ion currents must be negligibly small in this experiment. As an upper limit for a possible systematic effect the standard error (Eq. 5.16) of measurement #37 to #40, $0.19\,\text{pm}$, is chosen.

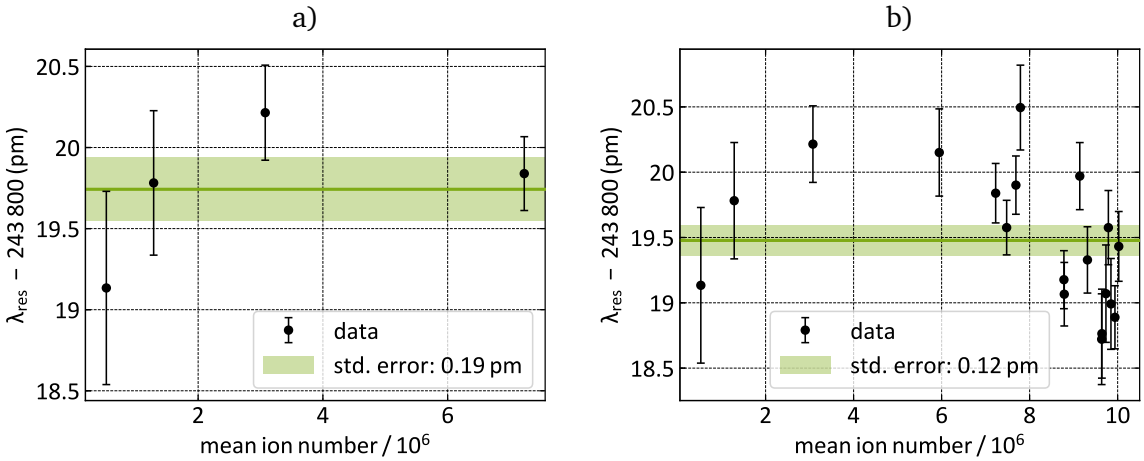

Figure 5.16: Resonance wavelength plotted as a function of the mean ion number for ^{209}Bi coasting-beam measurements. a) Results of subsequent measurements #37 to #40 with the same ion injection. b) Results for all coasting-beam measurements. In both cases no influence with the expected functional behaviour for the ion current can be observed.

5.6.5 Ion Bunching

As discussed in Sec. 5.5, a mismatch between bunching frequency and electron-cooler voltage can have a significant impact on the ion velocity and the extracted wavelength. This is the reason why the bunched $^{209}Bi^{82+}$ measurements have been discarded. For the ^{208}Bi measurements there is no obvious difference between coasting- and bunched-beam mode observable, as shown in Fig. 5.17. To estimate an upper limit on the effect of a bunching frequency mismatch for this isotope, the bunched and coasting measurements are considered separately. The calculated weighted means are

$$\begin{aligned} {}^{208}\lambda_{\text{res, bun}} &= 221.440\,96(9)\,\text{nm} \\ {}^{208}\lambda_{\text{res, coas}} &= 221.440\,72(23)\,\text{nm} \end{aligned} \tag{5.25}$$

and are within their combined 1σ-range. The maximum difference within their respective 1σ-ranges is

$$\Delta^{208}\lambda_{\text{dif}} = ({}^{208}\lambda_{\text{res, bun}} + \Delta^{208}\lambda_{\text{res, bun}}) - ({}^{208}\lambda_{\text{res, coas}} - \Delta^{208}\lambda_{\text{res, coas}}) = 0.6\,\text{pm}. \tag{5.26}$$

Based on this difference, a systematic uncertainty of $2.8\,\text{ppm}$ is estimated for a potential bunching-frequency mismatch.

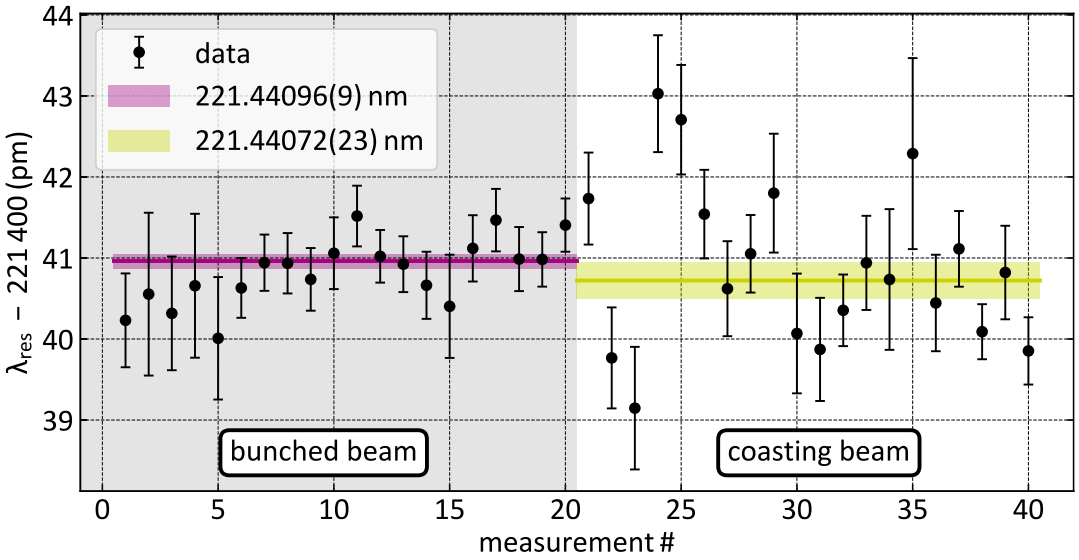

Figure 5.17: Resonance wavelength of $^{208}Bi^{82+}$ measurements with bunched and coasting beam. The maximum difference within the respective 1σ-ranges is $0.6\,\mathrm{pm}$.

5.6.6 Angular Alignment of Laser and Ion Beam

The alignment of laser and ion beam affects the extracted resonance wavelength via the angular dependence of the Doppler effect (Eq. 2.63). The maximum shift to a minimum wavelength occurs for a perfect anti-collinear alignment with $\theta = 180°$. A deviation from this angle leads to a symmetrically smaller wavelength shift in both directions due to the cosine function in the relation.

The laser and ion beams are superimposed with the T-scraper system inside the electron cooler. This allows the measurement of the horizontal and vertical position of both beams at two points $3.6\,\mathrm{m}$ apart (see Fig. 5.18). Assuming a misalignment of $1\,\mathrm{mm}$ in each direction, leads in the worst case to an alignment uncertainty of $0.8\,\mathrm{mrad}$, which corresponds to a wavelength shift of $0.03\,\mathrm{pm}$ for ^{208}Bi at the respective beam energy.

In addition, the ion beam follows a complex trajectory in the horizontal plane of the ESR, which is shown in Fig. 5.18 for the straight section along the electron cooler. The shape of the trajectory is mainly determined by the focusing and steering elements and has a parallel overlap with the electron beam within the electron cooler (indicated by the green band). The horizontal displacement in mm of the trajectory and the 1σ beam envelope (blue band) is caused by dispersive effects and the betatron motion. It was calculated by S. Litvinov with the betatron and dispersion functions (see Sec. 2.1.2) of the ESR.

The ion beam must be injected with an energy slightly higher than the reference energy of the synchronous particle, which corresponds to an outer orbit with a horizontal offset between $20\,\mathrm{mm}$ to $40\,\mathrm{mm}$ in the electron cooler section. Since the ion beam was cooled by the electron cooler and the laser could be superimposed with the ions at this orbit, the orbit offset was not corrected for the experiment.

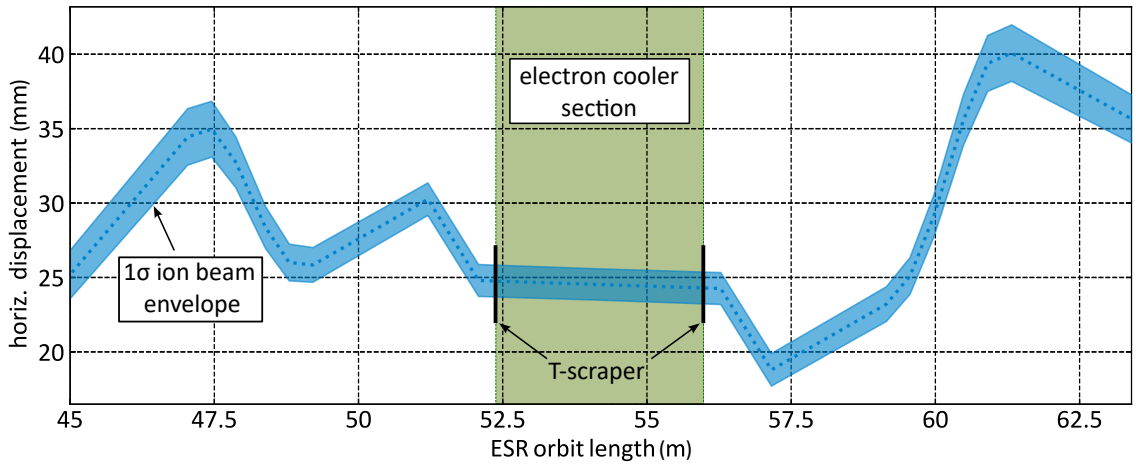

Figure 5.18: Simulation by S. Litvinov of the horizontal ion beam displacement and the 1σ ion beam envelope in the ESR. The straight section for laser and ion beam overlap is in the ESR reference frame from $45\,\mathrm{m}$ to $63\,\mathrm{m}$. The area of the electron cooler section is marked in green and the integrated T-scrapers are used for alignment.

Since the laser beam has a diameter of about $2\,\mathrm{cm}$ and according to the evaluation of the ion revolution gate (see subsection 5.3.1), the overlap of both beams is not limited to the cooler section, but takes place over the entire straight section. This means that an angular misalignment is inevitable and present in large sections of the trajectory inside the laser beam. To account for the ion beam misalignment, the ion angles are calculated with respect to the laser beam. Since this is a symmetric shift and the direction is not important, the absolute values of the angles can be considered. With Gaussian error propagation, the additional laser misalignment of $0.8\,\mathrm{mrad}$ is added to these angles. With this total alignment uncertainty for the different segments in the straight section, the wavelength transformation is performed. A weighted average is calculated from the result, to account for the length of each segment. This gives a total asymmetric alignment uncertainty of $4.4\,\mathrm{ppm}$.

5.6.7 Combined Systematic Uncertainties

A summary of the systematic uncertainties discussed in the previous sections is provided in Tab. 5.4. All uncertainties - statistical as well as systematical errors - are transformed to the ions rest frame and listed in ppm. The accumulated uncertainties result from Gaussian error propagation of the individual contributions.
The dominant uncertainty of $10.3\,\mathrm{ppm}$ is due to the high voltage measurement. Compared to the last laser spectroscopy experiment on H-like bismuth in 2014 [109], this uncertainty is about twice as high. The first reason for this is the use of a different high voltage divider. In 2014, the mobile HVDC2.1 divider from the Physikalisch-Technische Bundesanstalt (PTB) in Braunschweig with a specified uncertainty of only $13\,\mathrm{ppm}$ [138] was used. In addition, a Fluke 8508A multimeter significantly improved the measurement of the divided voltage.

Table 5.4: Uncertainty estimates for the hyperfine splitting of Bi^{82+}. All values in ppm.

	$^{209}Bi^{82+}$		$^{208}Bi^{82+}$	
	stat. Unc.	syst. Unc.	stat. Unc.	syst. Unc.
Fitting procedure	0.5		0.6	
Wavelength extraction		2.7		3.9
Laser linewidth		4.0		4.4
WM calibration	0.5	0.7	0.6	0.8
Ion bunching				2.8
Ion current		1.7		1.7
Space charge	0.9	2.3	0.9	2.3
HV measurement	0.4	10.3	0.5	10.3
Contact potential		2.9		2.9
Angular alignment		4.4		4.4
Overall uncertainty	1.3	12.9	1.4	13.7
Wavelength rest frame	243.8195(3)(32)nm		221.4409(3)(31)nm	
Energy rest frame	5085.08(1)(7)meV		5598.97(1)(8)meV	

Despite the increased uncertainty of the high voltage measurement, the overall systematic uncertainty is smaller than in the previous experiment ($17.7\,\mathrm{ppm}$ in [8]). The main factors are a better understanding of the effects caused by the ion current and the bunching amplitude. In this work compared to the previous, the ion current is about five times smaller for the stable isotope and two orders of magnitude smaller for the radioactive isotope. Thus, the corresponding effects of space charge potentials are strongly suppressed.
Effects of a mismatched bunching frequency become apparent in the case of $^{209}Bi^{82+}$. Due to the lack of information, it is not possible to extract accurate resonance data for the bunched mode measurements and only coasting beam results are reliable. For $^{208}Bi^{82+}$ no significant effect of a mismatch can be observed in the Schottky data or in the extracted hyperfine transition wavelengths. Therefore, the comparison with the coasting data results in a comparatively small uncertainty.

5.7 Results and Discussion

In this work, the hyperfine splitting energy of the H-like isotopes ^{209}Bi and ^{208}Bi is experimentally determined to be

$$\begin{aligned} {}^{209}\Delta E^{(1s)} &= 5085.08(1)(7)\,\mathrm{meV} \quad \text{and} \\ {}^{208}\Delta E^{(1s)} &= 5598.97(1)(8)\,\mathrm{meV} \end{aligned} \tag{5.27}$$

Table 5.5: Comparison of the measured hyperfine splitting $^{209}\Delta E^{(1s)}$ with previous experiments and theory. Except for Karpeshin et al., the theory values are scaled by $\mu_{\text{new}}/\mu_{\text{old}}$ to account for the corrected nuclear magnetic moment [10].

Experiment		Theory	
Reference	$^{209}\Delta E^{(1s)}$ (meV)	Reference	$^{209}\Delta E^{(1s)}$ (meV)
This work	$5085.08(8)$	Karpeshin et al. [140]	5085.84
Ullmann et. al [8]	$5085.03(10)$	Sen'kov et al. [59]	$5088(-3,+20)$
Lochmann et. al [126]	$5086.3(1.2)$	Boucard et al. [55]	5030.8
Klaft et. al [5]	$5084.03(84)$	Shabaev et. al [139]	$5077(26)$
		Tomaselli et al. [58]	$5035(12)$

with statistical and systematic errors, respectively. The energy difference in ^{209}Bi has been measured experimentally several times [5, 8, 126] and predicted theoretically, e.g., in [55, 58, 59, 139, 140]. In Fig. 5.19a, Fig. 5.19b and Tab. 5.5 the value obtained in this work is compared with the previous experimental results and theoretical predictions, respectively. The agreement with the recent experiment by Ullmann et al. is excellent and previous measurements have estimated their uncertainties reliable. The uncertainty of the hyperfine transition in ^{209}Bi^{82+} is slightly reduced by this work.

For the comparison with theory, predictions prior to 2018 are scaled by $\mu_{\text{new}}/\mu_{\text{old}}$ to account for the corrected nuclear magnetic moment [10]. The accuracy of the theoretical predictions are limited by the calculation of the Bohr-Weisskopf effect, which depends on the nuclear model and results in large uncertainties (see Sec. 2.4.3). However, the comparison shows a good agreement with [59, 139, 140], while the predictions of [55, 58] seem to underestimate the energy of the hyperfine splitting.

The agreement with the previous result shows the functionality and accuracy of the experimental setup. Clean conditions can therefore be assumed for the measurements on ^{208}Bi.

In contrast to the stable isotope, there has been no experimental data for the hyperfine splitting energy of ^{208}Bi^{82+} prior to this work. The extracted value is compared with the theoretical and semiempirical predictions performed by Schmidt et al. [11] in Fig. 5.19c. The theoretical prediction is based on full calculations of the individual contributions to the hyperfine splitting. It uses a new value for the magnetic moment that was obtained by assuming correct QED calculations and scaling the tabulated magnetic moment to obtain agreement for ^{209}Bi. The main uncertainty of $30\,\text{meV}$ is due to the magnetization distribution.

The second, semiempirical approach combines experimental results with theoretical calculations. It includes the measured hyperfine splitting constant of the $^4P_{1/2}$ state of neutral ^{208}Bi and ^{209}Bi and the hyperfine splitting of ^{209}Bi^{82+} obtained in [8]. Combined with the calculation of the hyperfine structure anomaly ratio, which appears to be stable for different nuclear models, a reduced uncertainty of $4\,\text{meV}$ was obtained.

The extracted result of this work is in excellent agreement with both predictions but has a

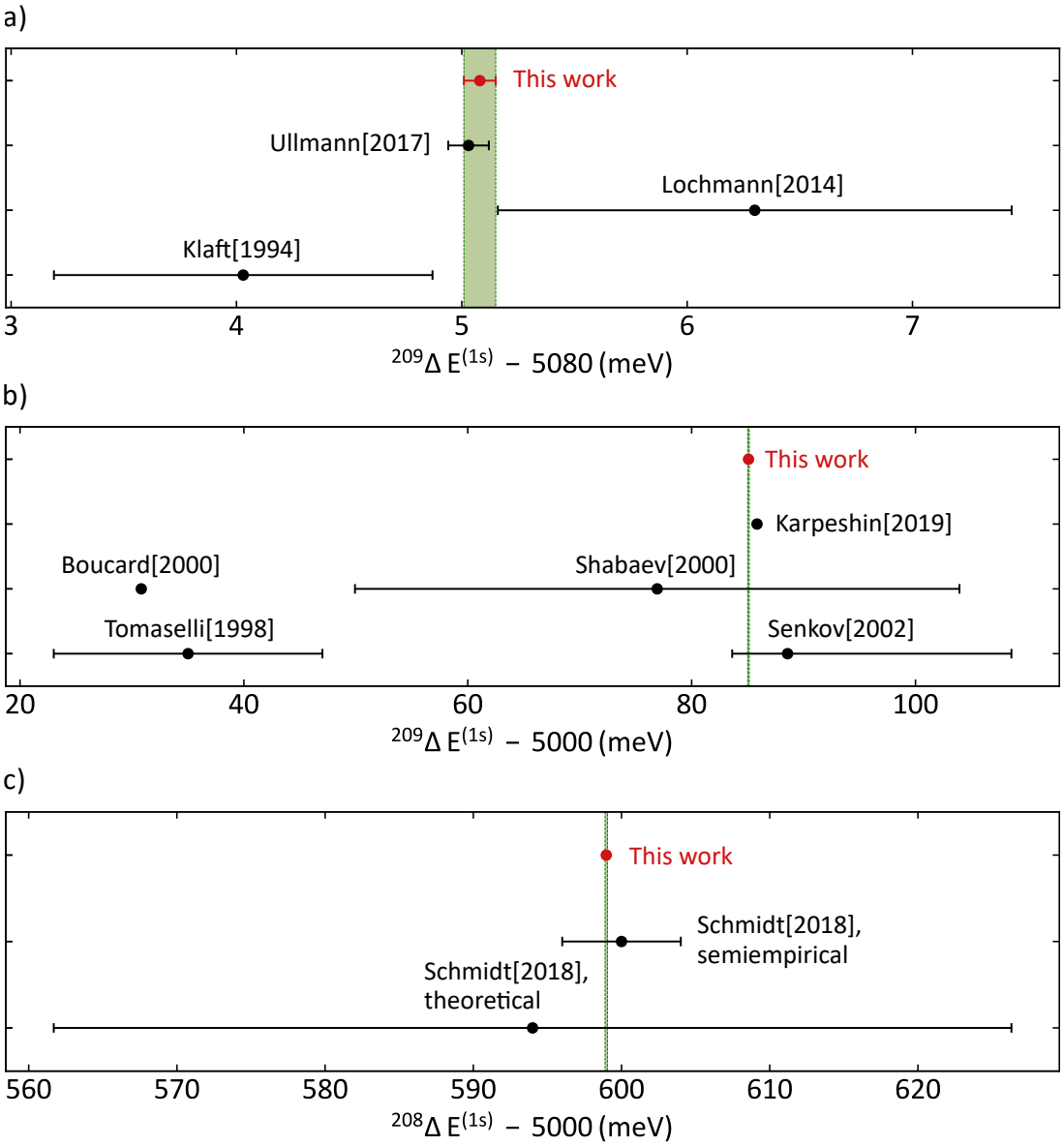

Figure 5.19: Comparison of the measured hyperfine splitting in $^{209}Bi^{82+}$ with a) previous experimental results [5, 8, 126] and b) theoretical predictions [55, 58, 59, 139, 140] (scaled by μ_{new}/μ_{old}). The result of this work is in excellent agreement with the latest experimental results and has a reduced uncertainty. Due to large uncertainties in the calculation of the Bohr-Weisskopf effect, the accuracy of the experiment is much higher than the theoretical predictions shown in b).
c) Comparison of the measured hyperfine splitting in $^{208}Bi^{82+}$ with a theoretical and semiempirical prediction [11]. The splitting obtained in this work is in excellent agreement with theory but has a much smaller uncertainty.

40-times smaller uncertainty than the semiempirical approach.
This is strong evidence for the proposed elimination [7] of nuclear structure contributions in the specific difference.
As pointed out in [11], the agreement between experiment and theory also validates a technique for the accurate extraction of nuclear magnetic moments from the measurement of hyperfine splitting energies, independent of hyperfine structure anomalies and shielding corrections. Additionally, the measured hyperfine splitting energy can be added to the ongoing discussion about the model dependence of the specific difference method and may lead to a better understanding of the Bohr-Weisskopf effect [140, 141].
The hyperfine splitting energy $^{208}\Delta E^{(1s)}$ in combination with the theoretical calculation of the specific difference $^{208}\Delta' E$ (see Tab. 2.2) provides the most accurate prediction for the hyperfine splitting in lithium-like ^{208}Bi^{80+}

$$\begin{aligned} {}^{208}\Delta E^{(2s)}_{\text{pred}} &= {}^{208}\Delta' E + \xi\, {}^{208}\Delta E^{(1s)} \\ &= -67.491(148)\,\text{meV} + 0.168\,86 \cdot 5598.97(9)\,\text{meV} \\ &= 877.95(15)\,\text{meV} = 1412.20(22)\,\text{nm}. \end{aligned} \tag{5.28}$$

This prediction is consistent with the calculated semiempirical and theoretical approach and has a three times smaller uncertainty than the former. The main uncertainty is due to the remaining contribution of the nuclear magnetic moment in the theoretical calculation of $^{208}\Delta' E$.
This result is important to reduce the search scan range in the upcoming laser spectroscopy beamtime at the ESR with lithium-like ^{208}Bi, which has been approved by the GSI Project Advisory Committee (GPAC) for the upcoming experiment period [142]. If the measurement is successful, a second independent pair of hyperfine splittings will be determined experimentally and the specific difference can be extracted. This can resolve some remaining theoretical problems, for example in the calculation of the magnetic shielding constant [143].
The combined results for the specific difference in ^{209}Bi and ^{208}Bi will constitute the most stringent bound state QED test in strong magnetic fields.
Besides the big importance of this experiment for QED tests, it also marks a major milestone for laser spectroscopy in storage rings. Laser spectroscopy with such a small number of ions (see 5.6.4) stored in a storage ring at relativistic velocities has never been achieved before. Measurements in the previous beamtime in 2014 [109] were performed with ion currents of $0.2\,\text{mA}$ to $1.7\,\text{mA}$, which is more than an order of magnitude higher. The enhancement in sensitivity is possible, because of the improved experimental setup and the rigorous data analysis. Prior to this work, it was questionable, whether the amount of ions is sufficient for laser spectroscopy. This work demonstrates the feasibility under such conditions and shows the potential for other experiments on rare isotopes with low production yields.

6 Conclusion and Outlook

In this work, the ground-state hyperfine splitting of $^{208}Bi^{82+}$ was measured for the first time in a beamtime at the storage ring ESR at GSI. The ions were produced by a nuclear reaction in the stripper target at relativistic velocity in front of the ESR together with several different isotopes. In the ESR, the isotope of interest was identified and separated from the others, resulting in a few 10^5 ions for the laser spectroscopy experiment. This is the smallest number of ions for which laser spectroscopy could be successfully performed at the ESR and the first time ever that an in-flight produced isotope is targeted by laser spectroscopy in a storage ring. The overlap in anti-collinear geometry between the ion and the laser beam was realized in the electron cooler section and spatially separated from the fluorescence photon detection. Together with the optimized photon detection and the detailed data analysis, which reduces the background by introducing different analysis gates (see Sec. 5.3), the signal-to-noise ratio is improved to enable the extraction of the resonance position. The result is

$$^{208}\Delta E^{(1s)} = 5598.97(1)(8)\,\mathrm{meV}, \tag{6.1}$$

which is in very good agreement with the semiempirical and theoretical prediction of [11], while having a 40 times smaller uncertainty. This result is one part of the specific difference for the radioactive isotope ^{208}Bi. The missing part is the hyperfine transition in Li-like $^{208}Bi^{80+}$. By assuming a correct calculation of the specific difference in [11] and using the above value, the most accurate prediction for the transition in the Li-like ion is obtained

$$^{208}\Delta E^{(2s)}_{\mathrm{pred}} = 877.95(15)\,\mathrm{meV}. \tag{6.2}$$

This result reduces the search scan range in the upcoming beamtime [142]. If the predicted value can be confirmed in the experiment, it will demonstrate the cancelation of the Bohr-Weißkopf effect in the specific difference and will constitute the most stringent bound-state QED test in strong magnetic fields.

In addition to the laser spectroscopy on the radioactive isotope, the hyperfine splitting in $^{209}Bi^{82+}$ was also measured. This was used to test the experimental setup in combination with the data analysis. The result is in excellent agreement with the previous experiment [8] and shows a reliable calculation of the uncertainties.

In the future, laser spectroscopic measurements of heavy HCI are planned in ion traps to achieve ultimate precision. This will be possible at the HITRAP facility, which decelerates and cools relativistic ions from the ESR to make them available for precision experiments. Besides increasing the precision of measurements of hyperfine transitions by laser spectroscopy in the SpecTrap ion trap, the ARTEMIS experiment can be used to precisely measure the

magnetic moment of bismuth. By using a H-like ion for this measurement, electron-screening and diamagnetic-shielding effects, which are the largest uncertainties in the determination of magnetic moments from NMR, are fully under control. The increase in experimental precision would enable a new level of QED testing. The result of this work is important for such experiments as a starting point in order to find the narrow transition.
The HITRAP facility is not yet fully operational. In the last beamtime in 2022, the deceleration of ions to about $6\,\mathrm{keV/u}$ was reestablished. The final step for deceleration and cooling, which takes place in the Cooling Trap, has not yet been commissioned. The offline commissioning of this trap is the second part of this work. After the redesign of the Penning trap stack, it is tested with ions and electrons in offline experiments and first electron-cooling effects are observed in this work.
The storage of HCI from the SPARC-EBIT demonstrates sufficient long storage times for electron cooling. This implies that the residual gas pressure in the Cooling Trap is at a good level and that charge exchange processes do not prevent the cooling process of HCI. These results have to be confirmed with ions from the accelerator chain in the upcoming beamtimes. Furthermore, the output of the electron source is increased by optimized hardware and the amount of stored electrons is measured by the space charge in the trap. These measurements revealed a stored electron number of about 10^9, which is according to simulations [43] a sufficient amount for electron cooling.
In this work, ions and electrons were simultaneously stored in the Cooling Trap for the first time. This revealed in first tests an effect on the electrons, but no cooling effect on the ions could be observed. However, after the implementation of a new fluorescence detector, the Cooling Trap alignment and the electron injection could be optimized. This resulted in the first observation of electron cooling effects on HCI in a Penning trap.
Further optimization and systematic studies of the cooling process are in progress and will be presented in detail in the PhD thesis of S. Rausch [125].
With the results of this work, significant progress in the commissioning of the Cooling Trap is achieved, which will help for the operation with online ions. In the two upcoming beamtimes in 2024, the decelerated ions have to be transported through the LEBT to the Cooling Trap. In the trap, the knowledge gained from the offline commissioning will help to observe the cooling effects on the ions produced in the accelerator chain. After this final step, the HITRAP facility will be operational and able to distribute heavy HCI further to precision setups, where unique precision experiments will be performed.

Bibliography

[1] D. Hanneke, S. Fogwell, and G. Gabrielse, "New Measurement of the Electron Magnetic Moment and the Fine Structure Constant", Phys. Rev. Lett. **100**, 120801 (2008).

[2] T. Beier, "The g_j factor of a bound electron and the hyperfine structure splitting in hydrogenlike ions", Phys. Rep. **339**, 79–213 (2000).

[3] P. J. Mohr, G. Plunien, and G. Soff, "QED corrections in heavy atoms", Phys. Rep. **293**, 227–369 (1998).

[4] B. Franzke, "The heavy ion storage and cooler ring project ESR at GSI", Nucl. Instr. Meth. Phys. Res. B **24-25**, 18–25 (1987).

[5] I. Klaft, S. Borneis, T. Engel, et al., "Precision laser spectroscopy of the ground state hyperfine splitting of hydrogenlike $^{209}Bi^{82+}$", Phys. Rev. Lett. **73**, 2425–2427 (1994).

[6] P. Seelig, S. Borneis, A. Dax, et al., "Ground State Hyperfine Splitting of Hydrogenlike $^{207}Pb^{81+}$ by Laser Excitation of a Bunched Ion Beam in the GSI Experimental Storage Ring", Phys. Rev. Lett. **81**, 4824–4827 (1998).

[7] V. M. Shabaev, A. N. Artemyev, V. A. Yerokhin, O. M. Zherebtsov, and G. Soff, "Towards a Test of QED in Investigations of the Hyperfine Splitting in Heavy Ions", Phys. Rev. Lett. **86**, 3959–3962 (2001).

[8] J. Ullmann, Z. Andelkovic, C. Brandau, et al., "High precision hyperfine measurements in Bismuth challenge bound-state strong-field QED", Nature Communications **8**, 15484 (2017).

[9] A. V. Volotka, D. A. Glazov, O. V. Andreev, et al., "Test of Many-Electron QED Effects in the Hyperfine Splitting of Heavy High-Z Ions", Phys. Rev. Lett. **108**, 073001 (2012).

[10] L. V. Skripnikov, S. Schmidt, J. Ullmann, et al., "New Nuclear Magnetic Moment of ^{209}Bi: Resolving the Bismuth Hyperfine Puzzle", Phys. Rev. Lett. **120**, 093001 (2018).

[11] S. Schmidt, J. Billowes, M. Bissell, et al., "The nuclear magnetic moment of 208 Bi and its relevance for a test of bound-state strong-field QED", Phys. Lett. B **779**, 324–330 (2018).

[12] P. Micke, T. Leopold, S. King, et al., "Coherent laser spectroscopy of highly charged ions using quantum logic", Nature **578**, 1–6 (2020).

[13] F. Herfurth, T. Beier, L. Dahl, et al., "Highly charged ions at rest: The HITRAP project at GSI", AIP Conference Proceedings **793**, 278–292 (2005).

[14] H. Kluge, T. Beier, K. Blaum, et al., “HITRAP: A facility at GSI for highly charged ions”, Advances in Quantum Chemistry **53**, 83–98 (2007).

[15] H. Wiedemann, *Particle Accelerator Physics*, Vol. 4 (Springer, 2015).

[16] F. Hinterberger, *Physik der Teilchenbeschleuniger und Ionenoptik* (Springer Berlin Heidelberg, 2008).

[17] A. Piwinski, “Intra-beam scattering”, in Frontiers of particle beams, edited by M. Month and S. Turner (1988), pp. 297–309.

[18] R. Stokes and T. Wangler, “Radiofrequency Quadrupole Accelerators and Their Applications”, Annual Review of Nuclear and Particle Science **38**, 97–118 (1988).

[19] A. Schempp, “Research application of RFQ linacs”, Nucl. Instr. Meth. Phys. Res. B **99**, 688–693 (1995).

[20] F. Penning, “Die Glimmentladung bei niedrigem Druck zwischen koaxialen Zylindern in einem axialen Magnetfeld”, Physica **3**, 873–894 (1936).

[21] H. G. Dehmelt, “Experiments with an Isolated Subatomic Particle at Rest”, Physica Scripta **1991**, 47 (1991).

[22] K. Blaum, “High-accuracy mass spectrometry with stored ions”, Phys. Rep. **425**, 1–78 (2006).

[23] S. Schmidt, T. Murböck, Z. Andelkovic, et al., “Sympathetic cooling in two-species ion crystals in a Penning trap”, Journal of Modern Optics **65**, 1–11 (2017).

[24] M. Ahmadi, B. Alves, C. Baker, et al., “Observation of the 1S-2S transition in trapped antihydrogen”, Nature **541**, 506–510 (2017).

[25] C. Smorra, S. Sellner, M. Borchert, et al., “A parts-per-billion measurement of the antiproton magnetic moment”, Nature **550**, 371–374 (2017).

[26] D. Lunney (ISOLTRAP), “Extending and refining the nuclear mass surface with ISOLTRAP”, J. Phys. G **44**, 064008 (2017).

[27] G. Werth, V. N. Gheorghe, and F. G. Major, “Charged Particle Traps II: Applications”, in (Springer Berlin Heidelberg, 2009).

[28] G. Gabrielse, L. D. Haarsma, and S. L. Rolston, “Open-endcap Penning traps for high precision experiments”, International Journal of Mass Spectrometry and Ion Processes **88**, 319–332 (1989).

[29] J. Yu, M. Desaintfuscien, and F. Plumelle, “Ion density limitation in a Penning trap due to the combined effect of asymmetry and space charge”, Applied Physics B **48**, 51–54 (1989).

[30] M. Vogel, *Particle Confinement in Penning Traps: An Introduction*, Springer Series on Atomic, Optical, and Plasma Physics (Springer International Publishing, 2018).

[31] G. Gabrielse, S. Rolston, L. Haarsma, and W. Kells, “Antihydrogen production using trapped plasmas”, Phys. Lett. A **129**, 38–42 (1988).

[32] S. van der Meer, *Stochastic damping of betatron oscillations in the ISR*, tech. rep. (CERN, Geneva, 1972).

[33] G. Budker, "An effective method of damping particle oscillations in proton and antiproton storage rings", Soviet Atomic Energy **22**, 438–440 (1967).

[34] U. Schramm, M. Bussmann, D. Habs, et al., "Laser cooling and Spectroscopy of relativistic C^{3+} beams at the ESR", Hyperfine Interactions **162**, 181–188 (2005).

[35] D. Winters, T. Beck, G. Birkl, et al., "Laser cooling of relativistic heavy-ion beams for FAIR", Physica Scripta **2015**, 014048 (2015).

[36] W. M. Itano, J. C. Bergquist, J. J. Bollinger, and D. J. Wineland, "Cooling methods in ion traps", Physica Scripta **1995**, 106 (1995).

[37] S. Rolston and G. Gabrielse, "Cooling antiprotons in an ion trap", Hyperfine Interactions **44**, 233–245 (1989).

[38] H. Poth, "Electron cooling: Theory, experiment, application", Phys. Rep. **196**, 135–297 (1990).

[39] M. Steck and Y. A. Litvinov, "Heavy-ion storage rings and their use in precision experiments with highly charged ions", Progress in Particle and Nuclear Physics **115**, 103811 (2020).

[40] T. Winkler, "Untersuchung zur Elektronenkühlung hochgeladener schwerer Ionen", PhD thesis (Ruprecht - Karls - Universität Heidelberg, 1996).

[41] G. Gabrielse, W. Jhe, D. Phillips, et al., "A single trapped antiproton and antiprotons for antihydrogen production", Hyperfine Interactions **81**, 5–14 (1993).

[42] L. S. Brown and G. Gabrielse, "Geonium theory: Physics of a single electron or ion in a Penning trap", Rev. Mod. Phys. **58**, 233–311 (1986).

[43] G. Maero, "Cooling of highly charged ions in a Penning trap for HITRAP", PhD thesis (Ruperto-Carola Universität Heidelberg, 2008).

[44] E. Rutherford, "The scattering of alpha and beta particles by matter and the structure of the atom", Phil. Mag. Ser. 6 **21**, 669–688 (1911).

[45] N. Bohr, "On the constitution of atoms and molecules", The London, Edinburgh, and Dublin Philosophical Magazine and Journal of Science **26**, 1–25 (1913).

[46] J. Von Neumann, *Mathematische Grundlagen der Quantenmechanik* (Springer, Berlin, 1932).

[47] C. Foot, *Atomic physics* (Oxford University Press, USA, 2005).

[48] W. Demtröder, *Experimentalphysik 3: Atome, Moleküle und Festkörper*, Vol. 5 (Springer Spektrum, 2016).

[49] W. Gerlach and O. Stern, "Der experimentelle Nachweis des magnetischen Moments des Silberatoms", Zeitschrift für Physik **8**, 110–111 (1922).

[50] W. E. Lamb and R. C. Retherford, “Fine Structure of the Hydrogen Atom by a Microwave Method”, Phys. Rev. **72**, 241–243 (1947).

[51] W. Demtröder, *Experimentalphysik 4: Kern-, Teilchen- und Astrophysik*, Vol. 4 (Springer Spektrum, 2014).

[52] V. Hannen, J. Vollbrecht, Z. Andelkovic, et al., “Lifetimes and g-factors of the HFS states in H-like and Li-like bismuth”, J. Phys. B **52**, 085003 (2019).

[53] V. M. Shabaev, “Hyperfine structure of hydrogen-like ions”, J. Phys. B **27**, 5825 (1994).

[54] V. M. Shabaev, M. Tomaselli, T. Kühl, A. N. Artemyev, and V. A. Yerokhin, “Ground-state hyperfine splitting of high-Z hydrogenlike ions”, Phys. Rev. A **56**, 252–255 (1997).

[55] S. Boucard and P. Indelicato, “Relativistic many-body and QED effects on the hyperfine structure of lithium-like ions”, Eur. Phys. J. D **8**, 59–73 (2000).

[56] M. Gustavsson, C. Forssén, and A.-M. Pendrill, “Thallium hyperfine anomaly”, Hyperfine Interactions **127**, 347–352 (2000).

[57] L. N. Labzowsky, W. R. Johnson, G. Soff, and S. M. Schneider, “Dynamic proton model for the hyperfine structure of the hydrogenlike ion $^{209}_{83}\mathrm{Bi}^{82+}$”, Phys. Rev. A **51**, 4597–4602 (1995).

[58] M. Tomaselli, T. Kühl, P. Seelig, C. Holbrow, and E. Kankeleit, “Hyperfine splittings of hydrogenlike ions and the dynamic-correlation model for one-hole nuclei”, Phys. Rev. C **58**, 1524–1534 (1998).

[59] R. Senkov and V. Dmitriev, “Nuclear magnetization distribution and hyperfine splitting in Bi^{82+} ion”, Nucl. Phys. A **706**, 351–364 (2002).

[60] A. Bohr and V. F. Weisskopf, “The Influence of Nuclear Structure on the Hyperfine Structure of Heavy Elements”, Phys. Rev. **77**, 94–98 (1950).

[61] J. R. Crespo López-Urrutia, P. Beiersdorfer, D. W. Savin, and K. Widmann, “Direct Observation of the Spontaneous Emission of the Hyperfine Transition $F = 4$ to $F = 3$ in Ground State Hydrogenlike $^{165}\mathrm{Ho}^{66+}$ in an Electron Beam Ion Trap”, Phys. Rev. Lett. **77**, 826–829 (1996).

[62] J. R. Crespo López-Urrutia, P. Beiersdorfer, K. Widmann, et al., “Nuclear magnetization distribution radii determined by hyperfine transitions in the $1s$ level of H-like ions $^{185}\mathrm{Re}^{74+}$ and $^{187}\mathrm{Re}^{74+}$”, Phys. Rev. A **57**, 879–887 (1998).

[63] P. Beiersdorfer, S. B. Utter, K. L. Wong, et al., “Hyperfine structure of hydrogenlike thallium isotopes”, Phys. Rev. A **64**, 032506 (2001).

[64] A. Volotka, D. Glazov, G. Plunien, and V. Shabaev, “Progress in quantum electrodynamics theory of highly charged ions”, Annalen der Physik **525**, 636–646 (2013).

[65] A. V. Volotka, D. A. Glazov, I. I. Tupitsyn, et al., “Ground-state hyperfine structure of H-, Li-, and B-like ions in the intermediate-Z region”, Phys. Rev. A **78**, 062507 (2008).

[66] G. W. F. Drake, “QED Effects in Helium and Comparisons with High Precision Experiment”, Physica Scripta **2001**, 22 (2001).

[67] D. A. Glazov, A. V. Volotka, V. M. Shabaev, I. I. Tupitsyn, and G. Plunien, "Evaluation of the screened QED corrections to the g factor and the hyperfine splitting of lithiumlike ions", Phys. Rev. A **81**, 062112 (2010).

[68] S. Epp, J. Crespo López-Urrutia, M. Simon, et al., "X-ray laser spectroscopy of highly charged ions at FLASH", J. Phys. B **43**, 183001 (2010).

[69] A. Egl, I. Arapoglou, M. Höcker, et al., "Application of the Continuous Stern-Gerlach Effect for Laser Spectroscopy of the $^{40}Ar^{13+}$ Fine Structure in a Penning Trap", Phys. Rev. Lett. **123**, 123001 (2019).

[70] K. König, J. Krämer, C. Geppert, et al., "A new Collinear Apparatus for Laser Spectroscopy and Applied Science (COALA)", Review of Scientific Instruments **91**, 081301 (2020).

[71] C. G. Parthey, A. Matveev, J. Alnis, et al., "Improved Measurement of the Hydrogen $1S - 2S$ Transition Frequency", Phys. Rev. Lett. **107**, 203001 (2011).

[72] C. Gorges, L. V. Rodríguez, D. L. Balabanski, et al., "Laser Spectroscopy of Neutron-Rich Tin Isotopes: A Discontinuity in Charge Radii across the $N = 82$ Shell Closure", Phys. Rev. Lett. **122**, 192502 (2019).

[73] W. Demtröder, *Laser Spectroscopy: Basic Principles*, Vol. 4 (Springer, Feb. 2008).

[74] W. Demtröder, *Experimentalphysik 1: Mechanik und Wärme*, Vol. 5 (Springer Spektrum, 2008).

[75] K. Mohr, "First laser spectroscopy of Mg^+ at CRYRING@ESR and He-like Boron at HITRAP", PhD thesis (TU Darmstadt, 2022).

[76] C. Novotny, G. Huber, S. Karpuk, et al., "Sub-Doppler laser spectroscopy on relativistic beams and tests of Lorentz invariance", Phys. Rev. A **80**, 022107 (2009).

[77] R. Geller, *Electron cyclotron resonance ion sources and ECR plasmas* (IOP Press, Dec. 1996).

[78] M. A. Levine, R. E. Marrs, J. R. Henderson, D. A. Knapp, and M. B. Schneider, "The Electron Beam Ion Trap: A New Instrument for Atomic Physics Measurements", Physica Scripta **1988**, 157 (1988).

[79] K. Kromer, C. Lyu, M. Door, et al., "High-precision mass measurement of doubly magic ^{208}Pb", The European Physical Journal A **58**, 202 (2022).

[80] J. Morgner, B. Tu, C. M. König, et al., "Stringent test of QED with hydrogenlike tin", Nature **622**, 53–57 (2023).

[81] B. O'Rourke, S. Geyer, A. Silze, et al., "The SPARC EBIT at GSI; commissioning and future plans at the HITRAP beamline", Journal of Physics: Conference Series **163**, 012103 (2009).

[82] K. Mohr, A. Buß, Z. Andelkovic, et al., "Collinear Laser Spectroscopy of Helium-like $^{11}B^{3+}$", Atoms **11**, 11 (2023).

[83] C. F. Barnett, P. M. Stier, and G. E. Evans, “Pig Ion Source”, Review of Scientific Instruments **24**, 394–395 (1953).

[84] Z. Nouri, R. Li, R. Holt, and S. Rosner, “A Penning sputter ion source with very low energy spread”, Nucl. Instr. Meth. Phys. Res. A **614**, 174–178 (2010).

[85] W. Barth, U. Scheeler, H. Vormann, et al., “High brilliance beam investigations at the universal linear accelerator”, Phys. Rev. Accel. Beams **25**, 040101 (2022).

[86] W. Geithner, Private communication, 2023.

[87] D. Ondreka, C. Dimopoulou, H. Hüther, et al., “Recommissioning of SIS18 After FAIR Upgrades”, in Proceedings of 10th International Particle Accelerator Conference (2019).

[88] C. Scheidenberger, T. Stöhlker, W. Meyerhof, et al., “Charge states of relativistic heavy ions in matter”, Nucl. Instr. Meth. Phys. Res. B **142**, 441–462 (1998).

[89] R. Sánchez, Private communication, 2023.

[90] M. Lestinsky, A. Bräuning-Demian, H. Danared, et al., “CRYRING@ESR: present status and future research”, Physica Scripta **2015**, 014075 (2015).

[91] H. F. Beyer, D. Liesen, and O. Guzman, “On the total recombination between cooling electrons and heavy ions”, Part. Accel. **24**, 163–175 (1989).

[92] S. Passon, J. Meisner, A. Heinrich, et al., “Modular Wideband High Voltage Divider for Metrological Purposes”, in Proceedings of 20th International Symposium on High Voltage Engineering (Aug. 2017).

[93] R. Meisner and M. Seckelmann, *Charakteristische Daten des Hochspannunsteilers Ohm Labs HVS 250*, 24030 PTB 18 (Physikalisch-Technische Bundesanstalt Braunschweig, 2018).

[94] P. Fork, *Lecture Notes on Beam Instrumentation and Diagnostics*, Joint University Accelerator School, 2023.

[95] *GE02DT-ML technical information*, Datasheet, GSI, 2023.

[96] B. Franzke, H. Geissel, and G. Münzenberg, “Mass and lifetime measurements of exotic nuclei in storage rings”, Mass Spectrometry Reviews **27**, 428–469 (2008).

[97] M. S. Sanjari, P. Hülsmann, F. Nolden, et al., “A resonant Schottky pickup for the study of highly charged ions in storage rings”, Physica Scripta **2013**, 014088 (2013).

[98] Y. Litvinov, H. Geissel, T. Radon, et al., “Mass measurement of cooled neutron-deficient bismuth projectile fragments with time-resolved Schottky mass spectrometry at the FRS-ESR facility”, Nucl. Phys. A **756**, 3–38 (2005).

[99] F. Ozturk, B. Akkus, D. Atanasov, et al., “New test of modulated electron capture decay of hydrogen-like 142Pm ions: Precision measurement of purely exponential decay”, Phys. Lett. B **797**, 134800 (2019).

[100] S. Sanjari, *iqtools: Collection of code for working with offline complex valued time series data in Python*, version v4.0.6, June 2023.

[101] V. Hannen, D. Anielski, C. Geppert, et al., “Detection system for forward emitted photons at the Experimental Storage Ring at GSI”, Journal of Instrumentation **8**, 9018 (2013).

[102] R. Sánchez, M. Lochmann, R. Jöhren, et al., “Laser spectroscopy measurement of the 2s-hyperfine splitting in lithium-like bismuth”, J. Phys. B **50**, 085004 (2017).

[103] K. Ueberholz, L. Bozyk, M. Bussmann, et al., “XUV Fluorescence Detection of Laser-Cooled Stored Relativistic Ions”, Atoms **11**, 39 (2023).

[104] H. Backe, “Precision Spectroscopy at Heavy Ion Ring Accelerator SIS300”, Hyperfine Interactions **171**, 93–107 (2006).

[105] *9422B series data sheet*, Datasheet, ET Enterprises, Jan. 12, 2012.

[106] C. Brandau, J. Billowes, M. Bissell, et al., *Nuclear Hyperfine Mixing in $^{229}Th^{89+}$ - Storage Ring Studies of an Orders-Of-Magnitude Accelerated Nuclear Decay*, approved experiment proposal E142, GSI G-PAC44, 2020.

[107] B. Seiferle, L. von der Wense, P. V. Bilous, et al., “Energy of the Th-229 nuclear clock transition”, Nature, 243–246 (2019).

[108] M. Lochmann, “Laserspektroskopie der Grundzustands-Hyperfeinstruktur des lithiumähnlichen $^{209}Bi^{80+}$”, PhD thesis (Universität Mainz, 2013).

[109] J. Ullmann, “Laserspektroskopie an hochgeladenen Bismutionen zum Test der Quantenelektrodynamik”, PhD thesis (Friedrich-Schiller-Universität Jena, 2017).

[110] S. Minami, *VUPROM as 192-ch Multi-hit TDC and Scaler*, GSI Helmholtzzentrum für Schwerionenforschung GmbH, July 6, 2010.

[111] M. Steck, K. Beckert, P. Beller, et al., “Improved Performance of the Heavy Ion Storage Ring ESR”, (2004).

[112] Z. Andelkovic, F. Herfurth, N. Kotovskiy, et al., “Beamline for low-energy transport of highly charged ions at HITRAP”, Nucl. Instr. Meth. Phys. Res. A **795**, 109–114 (2015).

[113] M. Vogel, M. S. Ebrahimi, Z. Guo, et al., “Electron magnetic moment in highly charged ions: the artemis experiment”, Annalen der Physik **531**, 1800211 (2019).

[114] E. Bodewits, H. Bekker, A. de Nijs, et al., “Electron emission yields from boron-like Ar ions impinging on Au(100)”, Nucl. Instr. Meth. Phys. Res. B **269**, 1203–1207 (2011).

[115] W. T. Milner, “Double-Drift Beam Bunching Systems”, IEEE Transactions on Nuclear Science **26**, 1445–1449 (1979).

[116] U. Ratzinger, “H-type linac structures”, CERN Accelerator School : Radio Frequency Engineering, 351–380 (2005).

[117] F. Herfurth, Z. Andelkovic, W. Barth, et al., “The HITRAP facility for slow highly charged ions”, Physica Scripta **T166**, 014065 (2015).

[118] S. Yaramyshev, W. Barth, G. Clemente, et al., “A new Design of the RFQ Channel for GSI HITRAP Facility”, in Proceedings of LINAC2012 (Sept. 2012).

[119] G. Gabrielse and F. Mackintosh, “Cylindrical Penning traps with orthogonalized anharmonicity compensation”, International Journal of Mass Spectrometry and Ion Processes **57**, 1–17 (1984).

[120] J. Viering, “Design und Inbetriebnahme der neuen HITRAP Kühlfalle”, Masterthesis (TU Darmstadt, 2018).

[121] F. Chill, “Vermessung der Pumpeigenschafen einer kryogenen Oberfäche”, PhD thesis (Johann Wolfgang Goethe-Universität Jena, 2015).

[122] J. L. Wiza, “Microchannel plate detectors”, Nucl. Instr. Meth. **162**, 587–601 (1979).

[123] C. Krantz, “Intense Electron Beams from GaAs Photocathodes as a Tool for Molecular and Atomic Physics”, PhD thesis (Ruperto-Carola Universität Heidelberg, 2009).

[124] S. Rausch, M. Horst, Z. Andelkovic, et al., “Commissioning of the HITRAP Cooling Trap with Offline Ions”, Atoms **10**, 142 (2022).

[125] S. Rausch, PhD thesis in preparation (TU Darmstadt, 2024).

[126] M. Lochmann, R. Jöhren, C. Geppert, et al., “Observation of the hyperfine transition in lithium-like bismuth $^{209}Bi^{80+}$: Towards a test of QED in strong magnetic fields”, Phys. Rev. A **90**, 030501 (2014).

[127] A. Kramida, Yu. Ralchenko, J. Reader, and NIST ASD Team, NIST Atomic Spectra Database (ver. 5.10), National Institute of Standards and Technology, Gaithersburg, MD., Sept. 27, 2022.

[128] J.Adamczewski-Musch, M.Al-Turany, S.Augustin, et al., *The Go4 Analysis Framework Introduction*, version 6.2. GSI Helmholtzzentrum für Schwerionenforschung GmbH (Apr. 26, 2022).

[129] B. Franzke, “Interaction of stored ion beams with the residual gas”, CAS - CERN Accelerator School : fourth advanced accelerator physics course, 100–119 (1992).

[130] S. S. Wilks, “The Large-Sample Distribution of the Likelihood Ratio for Testing Composite Hypotheses”, The Annals of Mathematical Statistics **9**, 60–62 (1938).

[131] K. König, P. Imgram, J. Krämer, et al., “On the performance of wavelength meters: Part 2—frequency-comb based characterization for more accurate absolute wavelength determinations”, Applied Physics B **126**, 86 (2020).

[132] *FLUORESCEIN 548*, Datasheet, LUXOTTICA group, 2023.

[133] *Digital Multimeters 34460A, 34461A, 34465A (6½ digit), 34470A (7½ digit)*, Keysight Technologies (Dec. 22, 2022).

[134] P. Tipler and G. Mosca, *Physik für Wissenschaftler und Ingenieure*, Vol. 7 (Springer Spektrum, 2015).

[135] L. Guo, G. Hua, B. Yang, et al., “Electron work functions of ferrite and austenite phases in a duplex stainless steel and their adhesive forces with AFM silicon probe”, Scientific Reports **6**, 20660 (2016).

[136] J. D. Behrens, “Design and commissioning of a monoenergetic photoelectron source and active background reduction by magnetic pulse at the KATRIN experiment”, PhD thesis (Westfälische Wilhelms-Universität Münster, 2016).

[137] D. Winzen, V. Hannen, M. Bussmann, et al., “Laser spectroscopy of the $^2S_{1/2}$–$^2P_{1/2}$, $^2P_{3/2}$ transitions in stored and cooled relativistic C^{3+} ions”, Scientific Reports **11**, 9370 (2021).

[138] J. Hällström, A. Bergman, s. Dedeoglu, et al., “Performance of a Wideband 200-kV HVDC Reference Divider Module”, IEEE Transactions on Instrumentation and Measurement **63**, 2264–2270 (2014).

[139] V. M. Shabaev, A. N. Artemyev, O. M. Zherebtsov, et al., “Calculation of the hyperfine structure of heavy H- and Li-like ions”, Hyperfine Interact. **127**, 279–286 (2000).

[140] F. F. Karpeshin and M. B. Trzhaskovskaya, “Examination of the solution to the hyperfine structure “puzzle” in H-like and Li-like ^{209}Bi ions”, Phys. Rev. C **100**, 024326 (2019).

[141] F. F. Karpeshin and M. B. Trzhaskovskaya, “Comparison of Methods for Eliminating the Bohr–Weisskopf Effect in Atomic Spectra of ^{209}Bi Heavy Ions”, Phys. At. Nucl. **84**, 418–424 (2021).

[142] W. Nörtershäuser, J. Billowes, M. Bissell, et al., *Dielectronic Recombination-assisted laser spectroscopy: A new tool to investigate the hyperfine-puzzle in Bi*$^{80+,82+}$, approved experiment proposal E128, GSI G-PAC45, 2022.

[143] D. A. Glazov, A. V. Volotka, O. V. Andreev, et al., “Ground-state hyperfine splitting of B-like ions in the high-Z region”, Phys. Rev. A **99**, 062503 (2019).

Danksagung

An dieser Stelle möchte ich mich bei allen bedanken, die mich während meiner Promotionszeit begleitet und in vielfältiger Weise unterstützt haben.
Zuerst geht mein Dank an Wilfried Nörtershäuser, der mir die Möglichkeit gegeben hat, unter seiner Betreuung meine Arbeit in diesem spannenden Gebiet der Physik durchzuführen. Vielen Dank für die zahlreichen Erfahrungen, die ich bei Experimenten und Konferenzen rund um die Welt sammeln konnte, sowie die vielen aufschlussreichen Diskussionen.
Weiterhin möchte ich mich bei meinen Kollegen bedanken, die mir bei meinen täglichen Aufgaben an der GSI mit Rat und Tat zur Seite gestanden haben. Zoran, Rodolfo und Frank, die mir mit ihrem unerschöpflichen Wissen oftmals weiterhelfen konnten und immer ein offenes Ohr für mich hatten. Danke auch an Simon, der gemeinsam mit mir etliche Stunden im HITRAP-Tunnel mit Fehlersuche und Optimierung verbracht hat. Bei Konstantin möchte ich mich für die vielen anregenden Diskussionen bedanken und dafür, dass meine *python*-Abbildungen durch ihn auf ein neues Level gehoben wurden. Außerdem möchte ich Wolfgang, Nils, Sonja, Gleb, Nikita und Davide erwähnen.
Zudem bedanke ich mich bei der LaserSpHERe-Gruppe, die mich herzlich aufgenommen hat und mit der die Zusammenarbeit immer Spaß gemacht hat. Insbesondere sind hervorzuheben Patrick, Kristian und Laura.
Meinen Dank möchte ich auch an die gesamte LIBELLE/E128-Kollaboration richten. Vielen Dank für die Hilfe bei der Vorbereitung der Strahlzeit, die rund um die Uhr geleisteten Schichten und die Unterstützung, die ihr mir bei der Auswertung und dem Schreiben dieser Arbeit gegeben habt. Ohne Euch wären die Daten nicht zustande gekommen und die Arbeit in dieser Form nicht möglich gewesen. Zusätzlich möchte ich mich bei den Strahlzeitkoordinatoren, sowie für die Flexibilität von betroffenen Experimenten und Personal bedanken, dass die dreitägige Verlängerung der Strahlzeit nach dem vorzeitigen Ende möglich war. Diese Zeit war essentiell für die Ergebnisse dieser Arbeit.
Bedanken möchte ich mich auch bei Thomas Walther, der mich während meiner Bachelor- und Masterarbeit betreut hat und sich bereit erklärt hat, mein Zweitgutachter zu sein. Danke auch an Joachim Enders und Robert Roth für die Teilnahme an meiner Verteidigung.

Zu guter Letzt möchte ich mich bei meinen Eltern, meinem Opa und meiner Freundin bedanken. Ohne Eure bedingungslose Unterstützung, die ihr mir in den letzten vier Jahren gewährt habt, wäre diese Arbeit nicht möglich gewesen.

Vielen Dank!